

**INVESTIGATIONS INTO FLOW CELL ELECTROLYZERS  
FOR CO<sub>2</sub> REDUCTION**

by

Emily Jeng

A thesis submitted to the Faculty of the University of Delaware in partial fulfillment of the requirements for the degree of Master in Chemical Engineering

Winter 2021

© 2021 Jeng  
All Rights Reserved

**INVESTIGATIONS INTO FLOW CELL ELECTROLYZERS  
FOR CO<sub>2</sub> REDUCTION**

by

Emily Jeng

Approved: \_\_\_\_\_  
Name of Feng Jiao, Ph.D.  
Professor in charge of thesis on behalf of the Advisory Committee

Approved: \_\_\_\_\_  
Eric M. Furst, Ph.D.  
Chair of the Department of Chemical and Biomolecular Engineering

Approved: \_\_\_\_\_  
Levi T. Thompson, Ph.D.  
Dean of the College of Engineering

Approved: \_\_\_\_\_  
Louis F. Rossi, Ph.D.  
Vice Provost for Graduate and Professional Education and  
Dean of the Graduate College

## ACKNOWLEDGMENTS

I would like to thank the many people who have helped me throughout my graduate school career, leading to the cumulation of work for this thesis. First, I would like to thank my advisor Dr. Feng Jiao for all of his guidance in research. I appreciate his patience and his insight regarding the details of my research, and his interest in conducting groundbreaking and exciting research is something that I especially admire.

I would like to thank the Jiao group for all of their help and support over the years. I would like to especially thank Dr. Wesley Luc and Dr. Matthew Jouny, the two senior members of our lab group, who have provided me with the assistance and guidance for conducting research experiments and their helpful insights. I would also like to especially acknowledge Byunghee “Brian” Ko for all of his amazing help and conversations; spending so much time collaborating with and sharing the lab with him has been incredibly fun for these past couple years. I would like to thank the past and current members of the Jiao group: Haeun Shin, Sean Overa, Kentaro Hansen, Dr. Jingjing Lv, Rong “Summer” Xia, Dr. Bjorn Hasa, and Dr. Yaran Zhou. Thank you all for being such incredibly collaborative and supportive people during our days of work; I have enjoyed all the times we have spent together and will remember these memories fondly.

I would like to thank my collaborators at Lawrence Livermore National Laboratory, Dr. Zhen Qi and Dr. Juregen Biener, for all of their help in providing me materials for testing and their incredibly insightful and helpful comments in our

discussions regarding our research. In addition, I would like to thank the following people who have gone out of their way to try and help me for research: Dr. Brian Setzler for his help in the carbonate formation calculations for the study in CO<sub>2</sub> conversion, Dr. Jeffrey Horner for introducing me to ANSYS CFD software, Dr. David Phan for 3D printing electrolyzer flow fields for testing, and Dr. Casper Brady for general lab help. I would also like to thank the following professors in my committee for giving me insights about my research, as well as letting me access their lab and using their chemicals and equipment: Dr. Bingjun Xu and Dr. Yushan Yan. I would also like to thank Dr. Raul Lobo for our past discussions regarding some exciting and interesting ideas that my research could involve.

Thank you to all the CBE Staff for helping me throughout these years. I would like to thank Brian Brant and Alfred Lance at the machine shop for being so accommodating to all of my needs and fabricating the materials that I have needed. I would like to thank Neil Garrett and Weihua Deng for all of their general lab help, especially regarding equipment set-up, and I would like to thank Yamy Gonzalez for helping our lab regarding safety. Finally, I would like to thank the CBE administrative staff, past and present: Cinda Yonce, Rechilda “Chi” Alba, Teh Mary Walsh, Kathie Young, and Cheryl Davis-Robinson. Thank you for helping me navigate through the graduate school process, and I have always enjoyed our interactions about the events going on in Colburn.

I would like to thank my funding sources during my time at graduate school: The U.S. Department of Energy, Lawrence Livermore National Laboratory, and the DE Space Grant. Without their help, I would not have the resources to conduct the research that I have presented in this thesis.

During my time in the University of Delaware, I have made many friends, and I cannot thank them enough for making my time here much more enjoyable. I would especially like to thank the following people: Jacob Anibal, Arnav Malkani, Michiel Wessels, Yifan Wang, Muyuan Li, Daniel Yur, and Nathaniel Hamaker. I have had so many fun moments with you guys, whether it was trivia nights at Kate's, game nights, hot pot parties, or the fun Colburn Club events such as the ski trips, beach trips, picnics, and recruitment. I would like to thank the roommates that I have lived with during my time, past and present: Dr. Caitlin Wood, Esther Roh, Colleen Fridley, Michaela Jones, and Dr. Angela Norton. Thank you guys for being extremely open and willing to talk to me about our struggles during grad school; I could not have asked for better companions to have lived with.

In addition, I am so thankful that I could still maintain great contact with all of my old friends while at grad school. I would like to especially thank my best friends in the entire world, whom I met at Cornell: Yi-Chun "Kelly" Huang, Marion Quien, and Saeef Alam. I have always enjoyed our hangouts together, spending time in the silliest of ways, and our constant online conversations about our lives. I could not have asked for better friends. I would also like to thank my oldest and my most precious friend since high school, Gurmannat "Mannat" Kalra. I always enjoyed all of the times we would talk and hang out to catch up on each other's lives; I am thankful that I have a friend that has been at my side for so long.

Lastly, I would like to thank my incredibly supportive family. This includes my Grandma, Auntie Mei, Uncle Min, Auntie Ping, Uncle Ralph, Uncle Min, Aunt Gemma, and Gugu and Uncle Kevin. Thank you for all providing me with encouragement and words of wisdom when I was feeling down, not to mention the

financial gifts. I want to thank my cousins Peter, Steven, Lori, Zoey, and Zachary, who I have enjoyed spending time with during family reunions, especially during the tough times of quarantine due to COVID.

Finally, I want to thank the three most important people in my life: my mom Huaifen Lin Jeng, my dad Chyongshuh Alex Jeng, and my younger brother Dyllon Jeng. You guys have been there supporting all of the decisions that I have made. Thank you all for giving me reassurance and encouragement even during my lowest moments, and your love means the world to me.

## TABLE OF CONTENTS

LIST OF TABLES .....	ix
LIST OF FIGURES .....	x
ABSTRACT .....	xiv
Chapter	
1 INTRODUCTION .....	1
1.1 Motivation for Electrochemical CO <sub>2</sub> Reduction .....	1
1.2 Understanding CO <sub>2</sub> Electrolysis .....	4
1.2.1 CO <sub>2</sub> Electroreduction Basics and Figures of Merit .....	4
1.2.2 Catalysts and Product Selectivity .....	9
1.2.2.1 Silver and the Formation of CO .....	10
1.2.2.2 Copper and the Formation of C <sub>2+</sub> Products .....	11
1.2.3 CO <sub>2</sub> Electrolyzers and Testing .....	13
1.3 Thesis Scope and Structure .....	17
REFERENCES .....	18
2 INVESTIGATION OF CO <sub>2</sub> SINGLE-PASS CONVERSION IN A FLOW ELECTROLYZER .....	23
2.1 Introduction .....	23
2.2 Experimental Methods .....	25
2.2.1 Materials Preparation .....	25
2.2.2 Electrolyzer Set-up .....	26
2.2.3 Electrolyzer Testing .....	26
2.3 Results and Discussion .....	28
2.4 Conclusion .....	36
2.5 Acknowledgements .....	37
REFERENCES .....	38

3	SCALABLE GAS DIFFUSION ELECTRODE FABRICATION FOR ELECTROCHEMICAL CO <sub>2</sub> REDUCTION USING PHYSICAL VAPOR DEPOSITION METHODS .....	41
3.1	Introduction .....	41
3.2	Methods .....	44
3.2.1	Catalyst Coatings .....	44
3.2.2	Materials Characterization .....	45
3.2.3	Electrochemical active surface area analysis (ECSA) .....	46
3.2.4	Electrochemical Testing .....	47
3.3	Results and Discussion .....	47
3.4	Conclusion .....	61
3.5	Acknowledgements .....	62
	REFERENCES .....	63
4	CONCLUSIONS AND RECOMMENDATIONS .....	66
4.1	Conclusion .....	66
4.2	Recommendations .....	67
4.2.1	Carbonate Formation/CO <sub>2</sub> Crossover .....	67
4.2.2	Membranes and Ionomers .....	69
4.2.3	CO <sub>2</sub> Gas Delivery .....	70
	REFERENCES .....	73
Appendix		
A	SUPPLEMENTARY INFORMATION FOR CHAPTER 2- INVESTIGATIONS OF CO <sub>2</sub> SINGLE-PASS CONVERSION IN A FLOW ELECTROLYZER .....	76
	Calculation of theoretical rate of CO <sub>2</sub> conversion to carbonates .....	81
	REFERENCES .....	83
B	SUPPLEMENTARY INFORMATION FOR CHAPTER 3- SCALABLE GAS DIFFUSION ELECTRODE FABRICATION FOR ELECTROCHEMICAL CO <sub>2</sub> REDUCTION USING PHYSICAL VAPOR DEPOSITION METHODS .....	85
C	PERMISSION LETTERS .....	93

## LIST OF TABLES

Table 1.1: Theoretical Half-Cell Potentials for different eCO <sub>2</sub> R products <sup>12</sup> .....	6
Table A.1: Literature comparison of CO <sub>2</sub> single-pass conversion in CO <sub>2</sub> flow electrolyzers.....	76
Table A.2: Constants for the calculations of CO <sub>2</sub> consumption due to carbonate formations.....	78
Table B.1: Measured capacitance values and corresponding roughness factor of each sample obtained by normalization to Cu foil .....	88
Table B.2: Measured capacitance values and corresponding roughness factor of each sample obtained by normalization to Cu foil .....	89
Table B.3: Thermoneutral theoretical potentials for products detected in Fig. 3.4.....	92

## LIST OF FIGURES

Figure 1.1: Electricity Generation from selected Fuels (natural gas, renewables, nuclear, coal) since 2010, including projections up to 2050 <sup>6</sup> .....	2
Figure 1.2: Schematic showing the closed carbon cycle. Renewable electricity is used to power the electrochemical conversion of CO <sub>2</sub> into products that could be used in the industrial and transportation sectors. The emitted CO <sub>2</sub> from these sectors can then be reused, starting the cycle again once more.....	4
Figure 1.3: A hypothetical potential vs current curve for eCO <sub>2</sub> R showing all of the different overpotential controlled regimes: E <sup>n</sup> (theoretical potential), $\eta_{act}$ (activation overpotential), $\eta_{ohm}$ (ohmic overpotential), and $\eta_{mt}$ (mass transport overpotential). Copied with permission from [13]. .....	8
Figure 1.4: Schematics demonstrating CO <sub>2</sub> electrolyzers using a Membrane Electrode Assembly (MEA) configuration: (a) An electrolyzer using a cation exchange membrane, in which the main charge carrier is the proton traveling to the cathode (b) An electrolyzer using an anion exchange membrane, in which the main charge carrier is the hydroxide ion traveling to the anode .....	14
Figure 1.5: Schematic of the three-compartment microfluidic cell, another electrolyzer configuration used for testing CO <sub>2</sub> electrolysis.....	15
Figure 1.6: Schematic showing the three-phase boundary, where the gas, electrolyte, and catalyst meet. ....	17
Figure 2.1: Schematic diagrams of (a) the CO <sub>2</sub> flow electrolyzer configuration and (b) the cathode-membrane interface with multiple competing reactions.....	29
Figure 2.2: Performance of a 25-cm <sup>2</sup> flow electrolyzer operated at different CO <sub>2</sub> feeding rates: (a) CO partial current density profiles at various cell voltages, (b) fraction of CO <sub>2</sub> feed being converted to CO via eCO <sub>2</sub> RR, (c) rates of CO <sub>2</sub> being consumed due to carbonate formation, and (d) fraction of unreacted CO <sub>2</sub> feed at various current densities. The solid curve in (c) is the theoretical rate of CO <sub>2</sub> conversion to carbonates estimated by the Nernst-Planck equation (Appendix A.1).....	30

Figure 2.3: Effects of reaction temperature on the CO <sub>2</sub> single-pass conversion at a fixed CO <sub>2</sub> feeding rate of 80 mL/min: (a) CO partial current densities, (b) fraction of CO <sub>2</sub> feed being converted to CO via eCO <sub>2</sub> RR, (c) fraction of CO <sub>2</sub> feed consumed by the carbonate formations, and (d) fraction of unreacted CO <sub>2</sub> feed in the gas effluent at various cell voltages.....	33
Figure 2.4: Compositions of the gas effluent from the cathode chamber of a CO <sub>2</sub> flow electrolyzer (25-cm <sup>2</sup> active electrode area) at different operating current densities: (a) 80 mA/cm <sup>2</sup> , (b) 160 mA/cm <sup>2</sup> , and (c) 240 mA/cm <sup>2</sup> . (d) is a comparison among the fractions of CO in the gas product streams under different operating conditions. The x-axis of (d) is the CO <sub>2</sub> feeding rate [mL/min] divided by the theoretical rate of eCO <sub>2</sub> RR [mL/min], estimated from the total current. ....	35
Figure 3.1: Characterization of Cu catalyst coatings: Top view SEM micrographs of (a) 400 nm thick EB and (b) MS Cu coatings on GDLs, as well as the corresponding cross-sectional SEM images (c,d); TEM micrographs of 100-nm-thick EB (e) and MS (d) Cu coatings. ....	49
Figure 3.2: RBS spectra from GDLs with nominally 400 nm thick EB-Cu (a) and MS-Cu (b) coatings. The surface peaks of <sup>64</sup> Cu, <sup>19</sup> F (from the PTFE content of the MPC layer), and <sup>12</sup> C are denoted by arrows. Dashed lines are RUMP simulations for 394 (a) and 358 nm (b) fully dense Cu coatings on MPC, and solid lines are the result of RUMP code simulations reflecting the Cu-to-C depth distribution in the MPC layer shown in (c); contact angle measurements on GDLs with nominally 400 nm thick EB (d) and MS-Cu (e) coatings; (f) EB/MS-Cu roughness factor vs. thickness values derived from EASA measurements shown in Fig. B.4 and B.5. ....	51
Figure 3.3: Faradaic efficiencies and current densities vs. potential for eCO <sub>2</sub> RR with 400 nm (a) EB-Cu and (b) MS-Cu catalysts. These tests were conducted in a three-compartment flow cell, with 15 sccm CO <sub>2</sub> and 1 M KOH electrolyte at room temperature. ....	53

Figure 3.4: Comparison of the CO <sub>2</sub> RR performance of EB-Cu samples of different thicknesses (100, 200, 400, and 800 nm) measured in a 3-compartment electrochemical flow cell (Fig. B.1), with 15 sccm CO <sub>2</sub> and 1 M KOH electrolyte. (a) Total current densities vs. potential for all the thicknesses; (b) ECSA-normalized eCO <sub>2</sub> RR current densities for each catalyst; (c) H <sub>2</sub> and CO <sub>2</sub> RR Faradaic efficiencies for all the different thicknesses at different current densities; and (d) FE of eCO <sub>2</sub> RR products (CO, methane, formate, ethylene, ethanol, acetate, propanol) vs. current density. ....	57
Figure 3.5: (a) Energy efficiency (CO <sub>2</sub> RR + HER) vs. current density for 100-800 nm EB Cu and 400 nm MS Cu catalyst coatings, and (b) energy efficiency vs. film thickness at the highest current density measured (300 mA/cm <sup>2</sup> for 100 nm EB-Cu, 400 mA/cm <sup>2</sup> for all other thicknesses). All tests were performed in the three-compartment flow cell (Fig. B.1) using 15 sccm CO <sub>2</sub> and 1 M KOH electrolyte. ....	58
Figure 3.6: Electrode potential vs. RHE and FE(HER) during a long-term stability test of 400 nm EB-Cu in the microfluidic electrochemical flow cell at a constant current density of 100 mA/cm <sup>2</sup> with 15 sccm CO <sub>2</sub> and 1 M KOH electrolyte. ....	60
Figure A.1- Serpentine flow field used for the cathode during testing: (a) picture and (b) drawing with dimensions. ....	79
Figure A.2-SEM image of 100-nm silver nanoparticles deposited on the gas diffusion layer.....	80
Figure B.1: Electrochemical Testing with the Three-Compartment Flow Cell Set-up, with (a) the schematic and (b) the picture during testing .....	85
Figure B.2: SEM images of (a, b) 100 nm, (c, d) 200 nm, and (e, f) 800 nm thickness EB-Cu samples .....	86
Figure B.3: Contact angle measurement on fibrous backing side of the GDL.....	87
Figure B.4: EB-Cu GDL electrochemical surface area (ECSA) measurements: (a) sample CV scans at different scan rates in 0.1 M HClO <sub>4</sub> for the 400 nm EB Cu, (b) plot of current density vs scan rate for capacitance measurements .....	88
Figure B.5: MS-Cu GDL electrochemical surface area (ECSA) measurements: Plot of current density vs scan rate for capacitance measurements 0.1 M HClO <sub>4</sub> .....	89

Figure B.6: Faradaic efficiencies and current densities vs. potential for EB-Cu at (a) 100 nm (b) 200 nm (c) 400 nm and (d) 800 nm thickness. These tests were conducted in the 3-compartment flow cell (Fig. B.1), with 15 sccm CO <sub>2</sub> and 1 M KOH electrolyte. ....	90
Figure B.7: Long-term stability test of 400 nm EB-Cu: (a) XPS Characterization of the EB-Cu sample before and after 6 hours at a constant current of 100 mA/cm <sup>2</sup> reaction; (b) Picture showing the formation of salt on the backside of the GDL during the stability testing; (c) Pre-reaction and (d) post-reaction SEM images of the EB-Cu catalyst coating show no change in morphology due to CO <sub>2</sub> R.....	91
Figure C.1: Permission Letter for Chapter 2 .....	93
Figure C.2: Permission Letter for Figure 1.3 .....	95

## ABSTRACT

The switch to renewable energy from fossil fuels as a source of electricity means that the issue of its intermittency must be addressed. One possible solution is to produce chemicals and fuels through electrochemical CO<sub>2</sub> reduction, as a way of energy storage in the form of chemicals. For CO<sub>2</sub> electroreduction to be feasible and practical in industrial applications, high current densities, or reaction rates, must be obtained. Therefore, developing electrolyzers, or reactors, for CO<sub>2</sub> reduction has been receiving more attention recently, as a way to boost current densities. In this thesis, I will be discussing work involving different types of CO<sub>2</sub> electrolyzers and various aspects that have been studied for further understanding of these electrolyzers.

In the first chapter, I discuss the single-pass conversion for CO<sub>2</sub> electrolyzers, a figure-of-merit that receives little attention in comparison to other figures-of-merits that are normally investigated (Faradaic efficiency, voltage, current densities, etc.). I mainly focus on the single-pass conversion of CO<sub>2</sub> to CO in MEA-type electrolyzers, investigating how different parameters such as gas flow rate and temperature affected the overall single-pass conversion. A lower gas inlet flow rate (15, 30 mL/min) would result in a higher conversion, whereas higher gas inlet flow rates (greater than 80 mL/min) were limited by the gas diffusion through the GDL, which resulted in partial current densities being controlled by mass transport limitations. Increasing the temperature from room temperature up to 60 C improved the gas diffusivity, which resulted in higher partial current densities at lower voltages. However, regardless of gas inlet flow rate or temperature, the highest single-pass conversion to CO obtained

was 43%. This conversion is limited by the CO<sub>2</sub> being consumed by the side product hydroxide to form carbonates, resulting in an overall conversion of 95% for CO<sub>2</sub> and thus less CO<sub>2</sub> available. In addition, I also show that this consumption of CO<sub>2</sub> by hydroxide affects the effluent stream of the electrolyzer, in which a maximum of 80% CO can be obtained at the single-pass conversion limit.

In the next chapter, I switch to focusing on the three-compartment cell configuration, looking into the aspects for fabricating electrodes for that type of electrolyzer. Two different copper catalyst deposition methods onto the Gas Diffusion Layer (GDL) were compared: electron beam (E-beam) deposition and magnetron sputtering. The E-beam deposited copper showed better performance for CO<sub>2</sub> electrolysis, as the copper deposited by magnetron sputtering had penetrated into the PTFE layer of the GDL, resulting in less hydrophobicity and thus more prone to flooding and shifting the selectivity to H<sub>2</sub>. The effect of catalyst loading was also investigated with E-beam deposited copper samples. Lower thicknesses (100 nm and 200 nm) showed worse performance due to less catalytic area available for CO<sub>2</sub> electrolysis. However, too much catalyst loading (800 nm thickness) resulted in the copper catalyst starting to aggregate, with less porosity and catalytic surface area. The 400 nm E-beam deposited copper had shown the best performance of all the copper samples tested.

While the work done in these chapters had provided insights into different aspects of CO<sub>2</sub> electrolyzers, there is still work that needs to be done for further improvement of CO<sub>2</sub> electrolyzers. For instance, for both of these electrolyzers, improved water management is still an issue that needs to be resolved, as flooding the catalyst would result in poor selectivity and stability. Looking into improving GDLs

and flow fields for gas delivery would help in preventing flooding. In addition, CO<sub>2</sub> forming carbonates as a side reaction is another challenging issue, as it limits the overall single-pass conversion for CO<sub>2</sub> to other products, and can also result in poor stability from the salt formation blocking gas delivery. These are some of the issues that should be solved going forward in the development of CO<sub>2</sub> electrolyzers.

## **Chapter 1**

### **INTRODUCTION**

#### **1.1 Motivation for Electrochemical CO<sub>2</sub> Reduction**

As the concentration of carbon dioxide (CO<sub>2</sub>) in the atmosphere continues to increase, surpassing 400 ppm as of 2020, the impact of climate change continues to be a concern. In 2015, the Paris Agreement had declared the need to lower the global temperature change to 1.5 °C<sup>1</sup>, an ambitious goal that would require the implementation of new technologies with net-zero emissions<sup>2</sup>. Global CO<sub>2</sub> emissions in 2050 would need to be reduced by 50-80%<sup>3</sup>, and reducing the concentration of CO<sub>2</sub> will require drastic changes, up to the gigaton scale<sup>4</sup>.

By switching to utilizing renewable energy sources, the electricity sector is expected to be crucial in cutting down greenhouse gas emissions<sup>5</sup>. As shown in Figure 1.1, in 2019, renewable energy electricity generation consisted of 19% of total electricity generation, resulting in a decrease of 25% in the sector's emitted carbon emissions<sup>6</sup>. Renewables are projected to make up to 31% of total electricity generation in 2050<sup>6</sup>, resulting in a lower cost of electricity that would make operating costs competitive with that of conventional chemical processing<sup>7</sup>. With this increase in renewable electricity also comes the issue of variability, in which excess electricity would be produced during peak hours and would require the implementation of energy storage technologies<sup>8</sup>. Thus, the transformation of CO<sub>2</sub> to various fuels and chemicals through electrochemical methods has been receiving attention as a way to store excess electricity, reducing the demand for energy storage systems<sup>9</sup>.

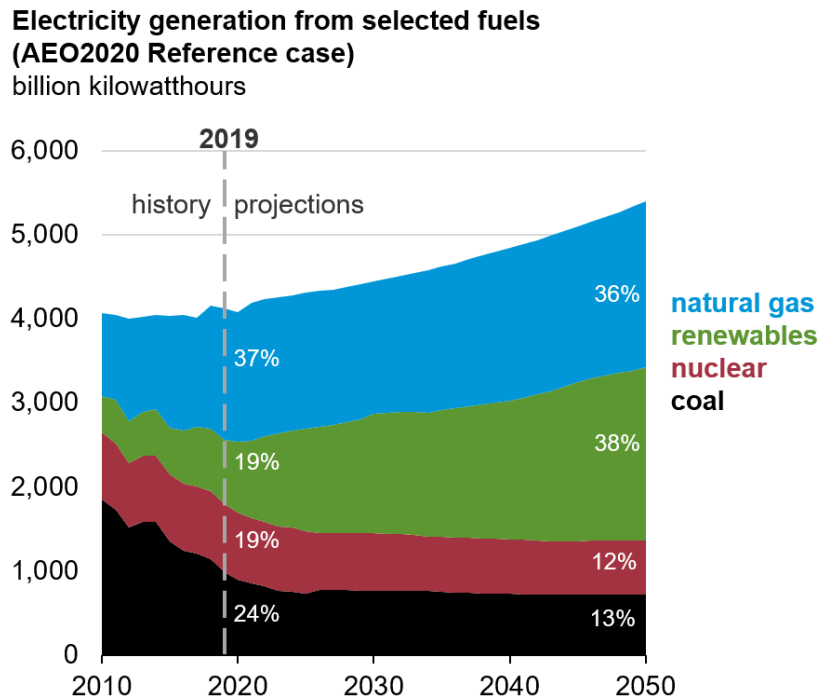


Figure 1.1: Electricity Generation from selected Fuels (natural gas, renewables, nuclear, coal) since 2010, including projections up to 2050<sup>6</sup>

The electrochemical conversion of CO<sub>2</sub> to valuable products can be conducted under relatively mild temperatures and pressures with renewable electricity, instead of through thermochemical processes that require intensive energy for higher temperatures and pressures. In addition, the electrochemical process can be run in modular, decoupled systems. CO<sub>2</sub> can be electrochemically converted into many different products, such as carbon monoxide, formate, ethylene, ethanol, and more. These are all chemicals that can be utilized in the industrial and transportation sectors. Ethylene, for instance, can be used as a precursor for plastics and chemicals like ethylene glycol. Ethanol is valuable as liquid fuel, since despite the push to

electrification, the transportation sectors will still be relying heavily on liquid fuels for the time being.

The production of these chemicals through electrochemical CO<sub>2</sub> reduction (eCO<sub>2</sub>R) allows for the penetration of renewables into the transportation and industry sectors. Currently, the transportation sector relies heavily on carbon-intensive fuels such as petroleum and gasoline, resulting in having the highest CO<sub>2</sub> emissions of the end-use sectors<sup>6</sup>, up to 28.2% of U.S. greenhouse gas emissions in 2018<sup>10</sup>. The industrial sector is also responsible for a significant portion of U.S. greenhouse gas emissions, up to 20% in 2019, with 19% of those emissions coming from the production of bulk chemicals<sup>11</sup>. Instead of relying heavily on carbon-intensive processes, the utilization of electrochemically synthesized chemicals can allow for a carbon-neutral process, as demonstrated in Figure 1.2, in which the converted products can be formed from the emitted CO<sub>2</sub> from the transportation and industrial sectors in a closed carbon cycle.

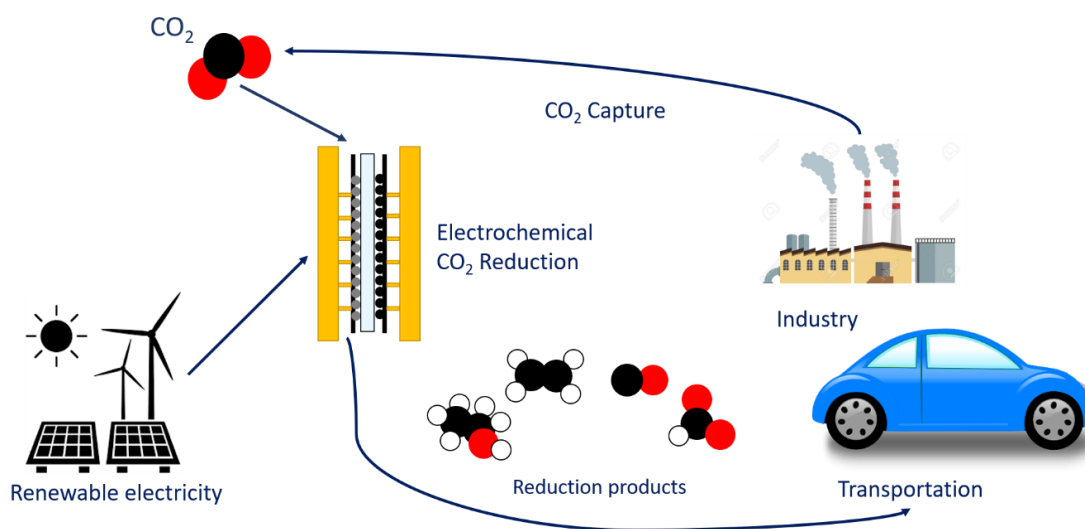


Figure 1.2: Schematic showing the closed carbon cycle. Renewable electricity is used to power the electrochemical conversion of CO<sub>2</sub> into products that could be used in the industrial and transportation sectors. The emitted CO<sub>2</sub> from these sectors can then be reused, starting the cycle again once more.

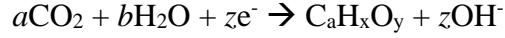
To become commercially applicable technologies to replace conventional chemical production processes, the production rates for eCO<sub>2</sub>R must be improved. Currently, the field of eCO<sub>2</sub>R is pushing towards the study of electrochemical flow cells to improve these reaction rates. While much work has already been done in the development of different electrolyzers for eCO<sub>2</sub>R regarding higher current densities at lower and there are certain aspects of flow cell electrolyzers that still need to be studied.

## 1.2 Understanding CO<sub>2</sub> Electrolysis

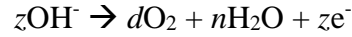
### 1.2.1 CO<sub>2</sub> Electroreduction Basics and Figures of Merit

An electrochemical system consists of two electrodes: a cathode and an anode. The cathode, which the electrons flow to and is negatively charged, is where the

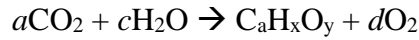
reduction reaction takes place. For eCO<sub>2</sub>R, for an alkaline system a generalized reduction reaction from CO<sub>2</sub> to other carbon products can be formed:



where a, b, z, x, and y are coefficients. The reduction reaction must be paired with an oxidation reaction at the anode, which is positively charged and will provide the electrons necessary for the reduction reaction to occur; for electrochemical CO<sub>2</sub> reduction (eCO<sub>2</sub>R), the oxidation reaction is typically water oxidation, in which water is converted to oxygen:



These two reactions will result in an overall reaction:



To convert a thermodynamically stable molecule such as CO<sub>2</sub> into different products, a driving force must be applied. For electrochemical processes, that driving force is the applied potential, which influences the transfer of charge and thus the rate of the reaction. The theoretical potential to form a product from eCO<sub>2</sub>R can be calculated through the following,

$$E^\circ = -\frac{\Delta G}{zF}$$

where  $E^\circ$  is the theoretical potential,  $\Delta G$  is the free energy of the reaction in J/mol,  $z$  is the mole of electrons needed to convert one mole of product, and  $F$  is Faraday's constant (96485 C/mol  $e^-$ ). Table 1.1 shows the theoretical half-cell potentials for the different products that can form from  $eCO_2R$ .

Table 1.1: Theoretical Half-Cell Potentials for different  $eCO_2R$  products<sup>12</sup>

Product	Number of electrons [z]	Half-cell potential [V]
Carbon monoxide (CO)	2	-0.11
Formate (HCOO <sup>-</sup> )	2	-0.03
Methane (CH <sub>4</sub> )	8	0.17
Acetate (CH <sub>3</sub> COO <sup>-</sup> )	8	-0.26
Ethanol (C <sub>2</sub> H <sub>5</sub> OH)	12	0.09
Ethylene (C <sub>2</sub> H <sub>4</sub> )	12	0.08
Propanol (C <sub>3</sub> H <sub>7</sub> OH)	18	0.21

Meanwhile, the theoretical half-cell potential for water oxidation is 1.23 V. To calculate the total theoretical cell potential for a specific product, the half-cell reduction potential is subtracted from 1.23 V. However, to obtain reasonable reaction rates, a potential higher than the theoretical potential must be applied. The overpotential, or the difference between the actual applied potential and the theoretical potential, is one of the most important figures of merit for  $eCO_2R$ .

Another figure of merit for  $eCO_2R$  is the current density, which is a measure of the rate of formation of the product. As shown in Figure 1.3, the current density is dictated by three different overpotential regions: activation barriers, resistance, and mass transport limitations. At the lower potentials, kinetic activation is the dominant limitation, influenced by the catalyst and the electrolyte used. In this region, the

current density is determined by the Tafel equation, which relates current density to the amount of overpotential applied:

$$j = j_o \exp \left[ \frac{z\alpha_c F \eta}{RT} \right]$$

Where  $j_o$  is the exchange current density,  $\alpha_c$  is the cathodic charge transfer coefficient, and  $\eta$  is the overpotential. With the Tafel equation, one can also extrapolate the Tafel slope, which can be important for determining mechanistic information for electrochemical kinetics.

As the applied potential starts to increase, instead of increasing exponentially as expected from the Tafel equation, the current starts to increase linearly due to the ohmic resistances<sup>13</sup>. For electrolysis, the ohmic overpotential comes from solution resistances:  $\eta_{iR} = iR_s$ , where  $i$  is the current and  $R_s$  the solution resistance. At even higher overpotentials, the current density will eventually reach the mass transport overpotential regime, in which the current density stops increasing. In this regime, the current can then be described by the following equation:

$$j = \frac{nFDc_b}{\delta}$$

Where  $D$  is the diffusion coefficient of  $\text{CO}_2$ ,  $c_b$  is the bulk concentration of the reactant, and  $\delta$  is the diffusion length. The bulk concentration of the reactant becomes the limiting factor for the reaction rate, resulting in the current profile plateauing.

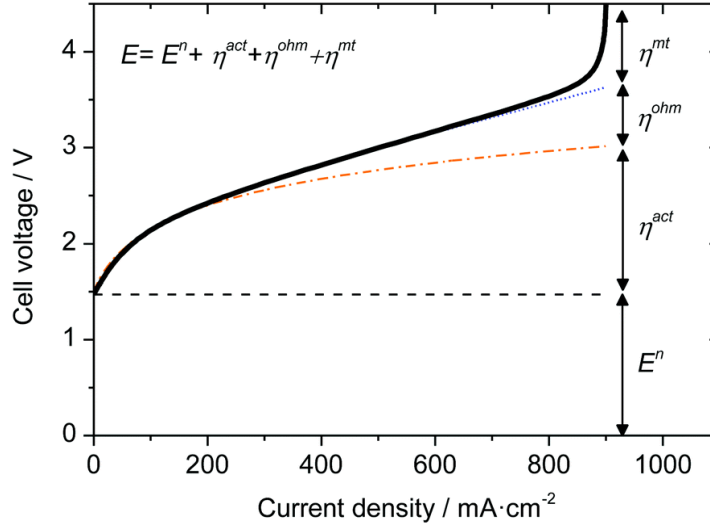


Figure 1.3: A hypothetical potential vs current curve for eCO<sub>2</sub>R showing all of the different overpotential controlled regimes:  $E^n$  (theoretical potential),  $\eta_{act}$  (activation overpotential),  $\eta_{ohm}$  (ohmic overpotential), and  $\eta_{mt}$  (mass transport overpotential). Copied with permission from [13].

For CO<sub>2</sub> electrolysis, another figure of merit often reported is the Faradaic efficiency of a certain product, which indicates how much of the total current is being utilized towards the production of the specified product. The major competing side reaction for eCO<sub>2</sub>R is the Hydrogen Evolution Reaction (HER), as the presence of water can lead to the formation of hydrogen.

To fully understand how much energy the electrolyzer is utilizing for eCO<sub>2</sub>R, the energetic efficiency can be calculated with the Faradaic efficiencies of each product:

$$\varepsilon_{energetic} = \sum_k \frac{\varepsilon_{Faradaic,k} E_k^{\circ}}{E_{applied}}$$

Where  $\varepsilon_{energetic}$  is the energetic efficiency,  $\varepsilon_{Faradaic,k}$  is the Faradaic efficiency of product k,  $E_k^{\circ}$  is the theoretical potential of product k, and  $E_{applied}$  is the

total applied cell potential. The energetic efficiency is usually used as a measure for the entire electrolyzer system. This means that for the improvement of CO<sub>2</sub> electrolyzers, not only should the selectivity and catalyst of the CO<sub>2</sub> reaction be studied, but the oxidation reaction and the electrolyte used must be considered as well, as the energetic efficiency takes those overpotential contributions into account as well.

### 1.2.2 Catalysts and Product Selectivity

For eCO<sub>2</sub>R, the product distribution is dependent on the cathode catalyst. In 1985, Yoshio Hori had screened different metals for testing for eCO<sub>2</sub>R, and the metals were grouped based on the selectivity towards certain products<sup>14</sup>:

1. CO selective: gold, silver, zinc, palladium
2. Formate selective: tin, lead, indium, cadmium, mercury, thallium
3. Hydrocarbons and alcohols: copper
4. H<sub>2</sub> selective: nickel, iron, platinum, and titanium

For formate selective metals, the carbon dioxide molecule binds to the metal through the oxygen atoms, instead of the carbon atom<sup>15</sup>. For the other products, the selectivity was noted to be determined by the metal's binding energy towards CO, one of the key intermediates in eCO<sub>2</sub>R. The metals selective towards CO formation had a weak binding energy towards CO, resulting in CO being desorbed from the catalyst before further reduction. Meanwhile, the H<sub>2</sub> selective metals strongly bind CO, unable to be reduced further to oxygenates or hydrocarbons. DFT calculations have suggested that as the surface coverage of CO of these strongly-binding metals increases, the binding energy of hydrogen on these metals weakens, making it more favorable for HER<sup>16</sup>.

For the purpose of this thesis, I will focus on the formation of CO using silver as the catalyst and the formation of hydrocarbons and oxygenates using copper as the catalyst.

#### **1.2.2.1 Silver and the Formation of CO**

CO is the one of the easiest products to form in eCO<sub>2</sub>R, as it only involves two electrons for the reaction. As a product, CO can either utilized for the synthesis of many chemicals<sup>17</sup>; some examples include CO with hydrogen to make syngas that will undergo the Fischer-Trophs process to create more valuable products<sup>18</sup>, or further electrochemically reduced<sup>19</sup>, which has recently been gaining more attention for higher selectivity towards C<sub>2+</sub> products such as oxygenates and hydrocarbons.

For the formation of CO, silver is one of the catalysts that has high selectivity towards CO in eCO<sub>2</sub>R. Silver catalysts have been utilized because of the lower cost compared to gold and better stability compared to zinc. Economic analysis has shown that for operating costs, silver and zinc have comparable minimum operating current densities<sup>20</sup>.

Different mechanisms for the formation from CO<sub>2</sub> to CO have been hypothesized. Initially, it was suggested that CO<sub>2</sub> first formed a CO<sub>2</sub><sup>-</sup> intermediate as an electron transfer step<sup>14</sup>. Experimental results<sup>21</sup> and predictions from computational work<sup>22</sup> have also claimed that the formation of a CO<sub>2</sub><sup>-</sup> intermediate occurs at higher overpotentials, since the increase in reduction potential could help to overcome the higher energy barrier to reach the CO<sub>2</sub><sup>-</sup> intermediate. The first step is the adsorption of CO<sub>2</sub> onto the catalyst surface. Some have proposed that the first step also involves a Proton Coupled Electron Transfer (PCET) step, from CO<sub>2</sub> to COOH\*. This

intermediate is more energetically favorable at lower potentials than the previously hypothesized  $\text{CO}_2^-$  intermediate, and has also been observed experimentally<sup>21</sup>. When the data was examined in the low overpotential regions, where current is kinetically controlled and not affected by mass transport limitations, a Tafel slope of 59 mV/dec was observed<sup>23</sup>, suggesting that the rate-limiting step involves a proton transfer to the adsorbed  $\text{COOH}^*$  intermediate.

Nanostructured silver catalysts have shown much more  $\text{eCO}_2\text{R}$  activity than polycrystalline silver. DFT calculations have indicated that step sites such as  $\text{Ag}(211)$  and  $\text{Ag}(110)$  have a lower energy barrier for the formation of the  $\text{COOH}$  intermediate<sup>24,25</sup>. For Ag nanoparticles, edge sites have a lower energy barrier for the stabilization of the  $\text{COOH}$  intermediate compared to that of corner sites<sup>25</sup>. Studies have suggested that this is the reason why Ag nanoparticles start showing lower  $\text{CO}_2$  reduction activity when the size becomes too small, as these nanoparticles start showing more corner sites compared to edge sites<sup>26</sup>. In addition to having favorable sites for  $\text{CO}_2$  reduction, nanostructured silver catalysts allow for higher electrochemical surface area, allowing to reach higher current densities<sup>27</sup>.

#### **1.2.2.2 Copper and the Formation of $\text{C}_{2+}$ Products**

Of all the metal catalysts that Hori had screened, copper is the only metal shows the most optimal  $\text{CO}$  binding energy, allowing for the formation of  $\text{C}_{2+}$  products, including ethanol, ethylene, acetate, and propanol.  $\text{CO}$  is widely accepted as an important intermediate for  $\text{CO}_2$  reaction, as the same products are formed when  $\text{CO}$  undergoes the electroreduction process.

However, after the formation of the  $\text{CO}$  intermediate, the mechanism for forming  $\text{C}_{2+}$  products continues to be discussed and debated. Some have proposed that

two adsorbed CO molecules would undergo dimerization to form  $\text{*OCCO}$ . The stabilization of this intermediate requires lower energy barrier for the Cu(100), which explains why the formation of ethylene is especially more favorable on this facet<sup>28,29</sup>. Others have suggested that another possible pathway is that the adsorbed  $\text{*CO}$  forms the  $\text{*CHO}$  intermediate before undergoing C-C coupling with another adsorbed  $\text{*CO}$ <sup>30,31</sup>.

The formation of the  $\text{*OCCHO}$  intermediate then proceeds to form either  $\text{*OCHCHO}$ , the glyoxyl intermediate<sup>32</sup>. This would then lead to the formation of acetaldehyde, which has been shown experimentally to be an intermediate in the formation for ethanol<sup>33</sup>. The formation of propanol does not seem to undergo the pathway of forming acetaldehyde. It was proposed that instead, the CO intermediate would undergo C-C coupling with a formed methylcarbonyl intermediate, followed by subsequent hydrogenation steps, to form propanol<sup>34</sup>.

Through experimental<sup>35,36</sup> and computational studies<sup>37</sup>, it has been observed that pH seems to have an influence on the product distribution for  $\text{CO}_2$ . Goddard et al have stated that at low pH,  $\text{C}_1$  pathways are preferred, forming mainly methane through the formation of a  $\text{*CHOH}$  intermediate. In neutral pH, one of the adsorbed CO molecules would be hydrogenated to form  $\text{*COH}$ <sup>37</sup>. The  $\text{*COH}$  on the surface was thought to be an intermediate for methane and ethylene. This intermediate would then undergo C-C coupling with  $\text{*CO}$  to form  $\text{*CO-COH}$ <sup>37</sup>. For high pH, early CO dimerization occurs, explaining why  $\text{C}_{2+}$  products are more favorable in alkaline conditions<sup>37</sup>.

### 1.2.3 CO<sub>2</sub> Electrolyzers and Testing

Initially, CO<sub>2</sub> electrolysis was conducted in small batch cell reactors, sometimes interchangeably called H-cell reactors. In these reactors, CO<sub>2</sub> is saturated in the electrolyte, usually a bicarbonate solution due to its buffer capacity and near neutral pH, since an acidic environment would promote the Hydrogen Evolution Reaction (HER) instead, while an alkaline environment would consume the fed CO<sub>2</sub>. A three-electrode set-up, which consists of a working, counter, and reference electrode, is often utilized for testing in an H-cell reactor. The potential of the working electrode, which is the sample electrode used for testing eCO<sub>2</sub>R performance, is measured with respect to the reference electrode, which is nonpolarizable. The counter electrode is there to close the current loop passing through the working electrode.

For H-cell reactors, the rate of eCO<sub>2</sub>R is limited by the low solubility of CO<sub>2</sub> in aqueous solution (34 mM CO<sub>2</sub> in standard conditions)<sup>38</sup>, resulting in CO<sub>2</sub> mass transport limitations to the catalyst. For equation 1.3, if we use a bulk concentration of CO<sub>2</sub> in aqueous solution and assume a  $D$  value of  $1 \times 10^{-5} \text{ m}^2 \text{ s}^{-1}$  and a  $\delta$  value of 1  $\mu\text{m}$ , a limiting current density of only 60 mA/cm<sup>2</sup> is obtained<sup>13</sup>. By studying eCO<sub>2</sub>R in continuous flow cell reactors, in which CO<sub>2</sub> is fed as a gas instead of through saturation of the electrolyte, these mass transport limitations can be overcome, increasing the bulk concentration and thus increasing the limiting current density. In addition, unlike H-cell reactors, flow cell electrolyzers can be easily scaled in an electrolyzer stack, to reach the rates needed for commercial scale<sup>39</sup>.

The operation of different types of flow cell electrolyzers has been reported for eCO<sub>2</sub>R. Initial flow cell electrolyzer designs with MEAs for eCO<sub>2</sub>R were investigated by Newman et al, in which four types of cell configurations were discussed<sup>40</sup>. Two of these designs they had investigated included membrane electrode

assembly (MEA) configurations. With an MEA set-up, an ion-conducting membrane acts as a solid polymer electrolyte that is sandwiched in between the cathode and the anode. This configuration is also sometimes called the “zero-gap” electrolyzer, since there is no electrolyte flow separating the electrodes from the membrane. When the cathode is in direct contact with a proton exchange membrane, almost all of the electrochemical activity went towards producing hydrogen, as the membrane provides the supply of protons to the cathode for immediate reduction to hydrogen. On the other hand, using anion exchange membranes avoids this proton transfer, instead transporting the produced hydroxide ions from the cathode to the anode. In addition, the alkaline environment allows for a lower solution resistance<sup>41</sup>, resulting in reaching high CO<sub>2</sub> F.E.’s at lower cell voltages.

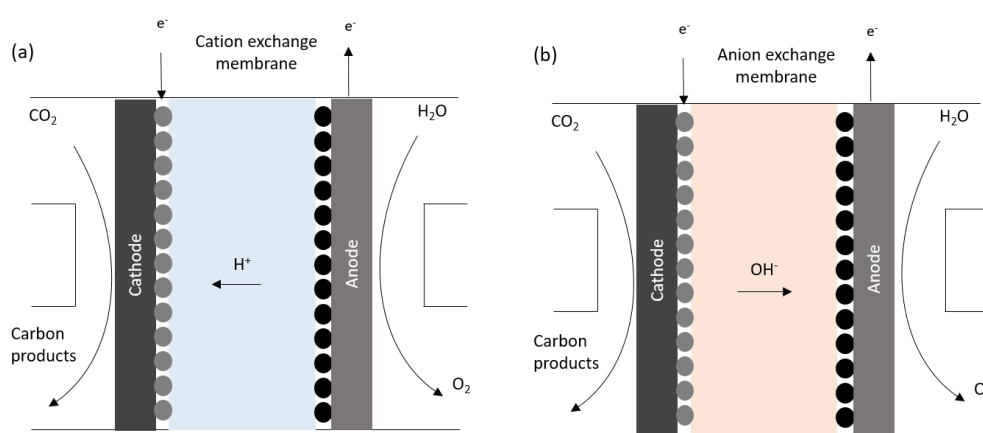


Figure 1.4: Schematics demonstrating CO<sub>2</sub> electrolyzers using a Membrane Electrode Assembly (MEA) configuration: (a) An electrolyzer using a cation exchange membrane, in which the main charge carrier is the proton traveling to the cathode (b) An electrolyzer using an anion exchange membrane, in which the main charge carrier is the hydroxide ion traveling to the anode

Another type of electrolyzer, designed by Kenis et al, includes a three-compartment microfluidic flow cell<sup>42</sup>, as shown in Figure 1.5. In this configuration, there are three flow channels. One of the flow channels is for the anolyte, allowing for water oxidation at the counter. For the cathode, one of the channels allows for the gas flow, which will travel through the fibrous backing of the GDL. Another channel is for the catholyte, which flows between the GDE and the membrane. By controlling the composition of the catholyte, the surface pH can be controlled, which can affect the applied potential and the product distribution. In this set-up, the three-electrode set-up can still be utilized, in which the reference electrode is placed in a separate compartment as part of the catholyte stream, where the flow channel tube between the working and the reference acts as a Luggin capillary. This set-up also allows for measuring the solution resistance, which can then be used for iR correction to obtain the actual half-cell potential applied to the working electrode. However, one of the major issues for eCO<sub>2</sub>R in this electrolyzer is the easy possibility of the electrode flooding<sup>43</sup>. In addition, when taking into account the additional extra electrolyte layer will add additional voltage<sup>44</sup>.

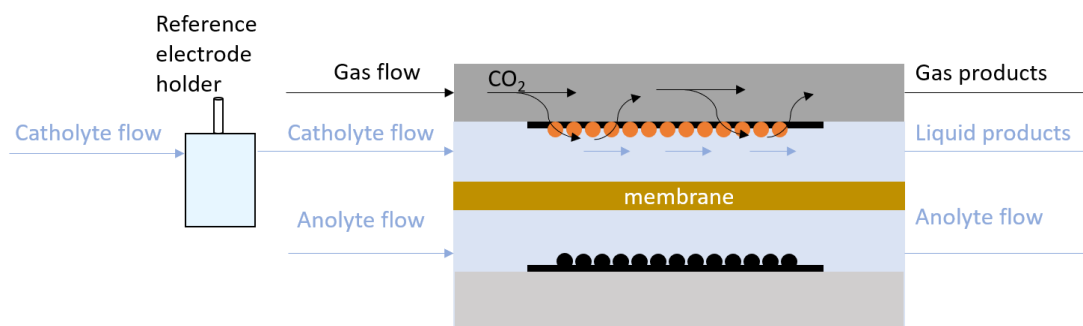


Figure 1.5: Schematic of the three-compartment microfluidic cell, another electrolyzer configuration used for testing CO<sub>2</sub> electrolysis.

For flow cell electrolyzers, the three-phase boundary, as shown in Figure 1.6, is where the gas reactant, liquid electrolyte, and electrons meet, and the optimization of this boundary is crucial to obtain these high reaction rates<sup>13</sup>. When eCO<sub>2</sub>R is conducted with a direct gas feed, the flow cell electrolyzer typically utilizes a Gas Diffusion Electrode (GDE). This electrode is usually fabricated by depositing the catalyst onto carbon paper known as the Gas Diffusion Layer (GDL). The GDL, which is also utilized as electrodes for fuel cells, is comprised of a porous carbon fiber backing and a microporous layer. The gas travels through the carbon fiber substrate, which is typically about 100-400  $\mu\text{m}$  thick with a porosity of about 65-80%<sup>12</sup>. The microporous layer, typically about 10-40  $\mu\text{m}$  thick with 30-50% porosity, consists of polytetrafluoroethylene (PTFE) so that the hydrophobicity can prevent electrolyte flooding, an issue which will prevent the gas reactant from reaching the catalyst layer<sup>12,45</sup>. Designing and optimizing GDL structures for CO<sub>2</sub> is one aspect that requires investigation, as the GDL can influence eCO<sub>2</sub>R performance, including voltage, selectivity, and overall stability.

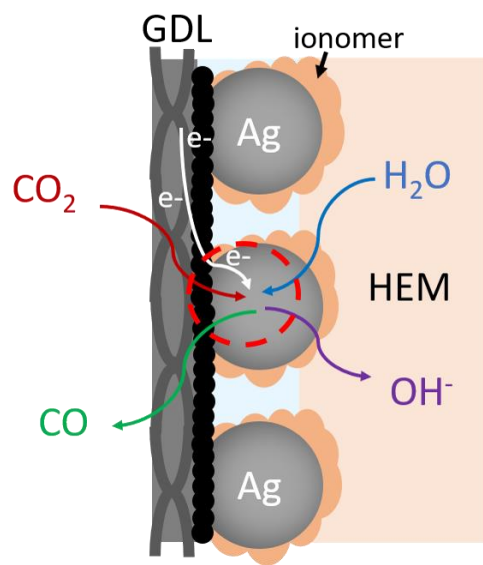


Figure 1.6: Schematic showing the three-phase boundary, where the gas, electrolyte, and catalyst meet.

### 1.3 Thesis Scope and Structure

This thesis will include two chapters discussing work related to  $\text{CO}_2$  electrolyzers. In the first chapter, I will be discussing another important figure-of-merit for  $\text{eCO}_2\text{R}$ , the single pass conversion of  $\text{CO}_2$ , through a systematic study involving an MEA-type electrolyzer for the conversion to  $\text{CO}$ . In the second chapter, I will switch to talking about the three-compartment microfluidic electrolyzer, specifically regarding the importance of electrode fabrication methods for this electrolyzer. Finally, I will conclude this thesis by providing recommendations on what could be done to further improve  $\text{CO}_2$  electrolyzers.

## REFERENCES

1. United Nations. Paris Agreement - UNFCCC. United Nations Climate Change (2015).
2. United Nations Framework Convention on Climate Change. Technological Innovation for the Paris Agreement: Implementing nationally determined contributions, national adaptation plans and mid-century strategies. **9**, 679–691 (2017).
3. Whipple, D. T. & Kenis, P. J. A. Prospects of CO<sub>2</sub> utilization via direct heterogeneous electrochemical reduction. *J. Phys. Chem. Lett.* **1**, 3451–3458 (2010).
4. Majumdar, A. & Deutch, J. Research Opportunities for CO<sub>2</sub> Utilization and Negative Emissions at the Gigatonne Scale. *Joule* **2**, 805–809 (2018).
5. Jenkins, J. D., Luke, M. & Thornstrom, S. Getting to Zero Carbon Emissions in the Electric Power Sector. *Joule* vol. 2 2498–2510 (2018).
6. Energy Information Administration, U. Annual Energy Outlook 2019 with projections to 2050. [www.eia.gov/aeo](http://www.eia.gov/aeo) (2019).
7. Haegel, N. M. et al. Terawatt-scale photovoltaics: Trajectories and challenges. *Science* (80-. ). **356**, 141–143 (2017).
8. Aneke, M. & Wang, M. Energy storage technologies and real life applications – A state of the art review. *Appl. Energy* **179**, 350–377 (2016).
9. Graves, C., Ebbesen, S. D., Mogensen, M. & Lackner, K. S. Sustainable hydrocarbon fuels by recycling CO<sub>2</sub> and H<sub>2</sub>O with renewable or nuclear energy. *Renew. Sustain. Energy Rev.* **15**, 1–23 (2011).
10. US EPA, O. Sources of Greenhouse Gas Emissions.
11. Controlling Industrial Greenhouse Gas Emissions | Center for Climate and Energy Solutions. <https://www.c2es.org/content/regulating-industrial-sector-carbon-emissions/>.

12. Martín, A. J., Larrazábal, G. O. & Pérez-Ramírez, J. Towards sustainable fuels and chemicals through the electrochemical reduction of CO<sub>2</sub>: Lessons from water electrolysis. *Green Chem.* **17**, 5114–5130 (2015).
13. Martín, A. J., Larrazábal, G. O. & Pérez-Ramírez, J. Towards sustainable fuels and chemicals through the electrochemical reduction of CO<sub>2</sub>: Lessons from water electrolysis. *Green Chem.* **17**, 5114–5130 (2015).
14. Hori, Y. Electrochemical CO<sub>2</sub> Reduction on Metal Electrodes. *Mod. Asp. Electrochem.* **42**, 89–189 (2008).
15. Feaster, J. T. et al. Understanding Selectivity for the Electrochemical Reduction of Carbon Dioxide to Formic Acid and Carbon Monoxide on Metal Electrodes. *ACS Catal.* **7**, 4822–4827 (2017).
16. Shi, C., Hansen, H. A., Lausche, A. C. & Nørskov, J. K. Trends in electrochemical CO<sub>2</sub> reduction activity for open and close-packed metal surfaces. *Phys. Chem. Chem. Phys.* **16**, 4720–4727 (2014).
17. Keim, W. *Catalysis in C1 Chemistry*. (Springer Netherlands, 2012).
18. Ciferno, J. P. & Marano, J. J. Benchmarking biomass gasification technologies for fuels, chemicals and hydrogen production. *US Dep. Energy. Natl. Energy* (2002).
19. Jouny, M., Hutchings, G. S. & Jiao, F. Carbon monoxide electroreduction as an emerging platform for carbon utilization. *Nature Catalysis* vol. 2 1062–1070 (2019).
20. Verma, S., Kim, B., Jhong, H. R. M., Ma, S. & Kenis, P. J. A. A gross-margin model for defining techno-economic benchmarks in the electroreduction of CO<sub>2</sub>. *ChemSusChem* (2016).
21. Firet, N. J. & Smith, W. A. Probing the Reaction Mechanism of CO<sub>2</sub> Electroreduction over Ag Films via Operando Infrared Spectroscopy. *ACS Catal.* **7**, 606–612 (2017).
22. Singh, M. R., Goodpaster, J. D., Weber, A. Z., Head-Gordon, M. & Bell, A. T. Mechanistic insights into electrochemical reduction of CO<sub>2</sub> over Ag using density functional theory and transport models. *Proc. Natl. Acad. Sci. U. S. A.* **114**, E8812–E8821 (2017).

23. Dunwell, M., Luc, W., Yan, Y., Jiao, F. & Xu, B. Understanding Surface-Mediated Electrochemical Reactions: CO<sub>2</sub> Reduction and beyond. *ACS Catal.* **8**, 8121–8129 (2018).
24. Rosen, J. et al. Mechanistic Insights into the Electrochemical Reduction of CO<sub>2</sub> to CO on Nanostructured Ag Surfaces. *ACS Catal.* **5**, 4293–4299 (2015).
25. Back, S., Yeom, M. S. & Jung, Y. Active Sites of Au and Ag Nanoparticle Catalysts for CO<sub>2</sub> Electroreduction to CO. *ACS Catal.* **5**, 5089–5096 (2015).
26. Kim, C. et al. Achieving Selective and Efficient Electrocatalytic Activity for CO<sub>2</sub> Reduction Using Immobilized Silver Nanoparticles. *J. Am. Chem. Soc.* **137**, 13844–13850 (2015).
27. Lu, Q. et al. A selective and efficient electrocatalyst for carbon dioxide reduction. *Nat. Commun.* **5**, (2014).
28. Schouten, K. J. P., Qin, Z., Gallent, E. P. & Koper, M. T. M. Two pathways for the formation of ethylene in CO reduction on single-crystal copper electrodes. *J. Am. Chem. Soc.* **134**, 9864–9867 (2012).
29. Jiang, K. et al. Metal ion cycling of Cu foil for selective C-C coupling in electrochemical CO<sub>2</sub> reduction. *Nat. Catal.* **1**, 111–119 (2018).
30. Montoya, J. H., Peterson, A. A. & Nørskov, J. K. Insights into C-C Coupling in CO<sub>2</sub> Electroreduction on Copper Electrodes. *ChemCatChem* **5**, 737–742 (2013).
31. Goodpaster, J. D., Bell, A. T. & Head-Gordon, M. Identification of Possible Pathways for C-C Bond Formation during Electrochemical Reduction of CO<sub>2</sub>: New Theoretical Insights from an Improved Electrochemical Model. *J. Phys. Chem. Lett.* **7**, 1471–1477 (2016).
32. Garza, A. J., Bell, A. T. & Head-Gordon, M. Mechanism of CO<sub>2</sub> Reduction at Copper Surfaces: Pathways to C<sub>2</sub> Products. *ACS Catal.* **8**, 1490–1499 (2018).
33. Bertheussen, E. et al. Acetaldehyde as an Intermediate in the Electroreduction of Carbon Monoxide to Ethanol on Oxide-Derived Copper. *Angew. Chemie - Int. Ed.* **55**, 1450–1454 (2016).

34. Chang, X., Malkani, A., Yang, X. & Xu, B. Mechanistic Insights into Electroreductive C-C Coupling between CO and Acetaldehyde into Multicarbon Products. *J. Am. Chem. Soc.* **142**, 2975–2983 (2020).
35. Ma, S. et al. One-step electrosynthesis of ethylene and ethanol from CO<sub>2</sub> in an alkaline electrolyzer. *J. Power Sources* **301**, 219–228 (2016).
36. Dinh, C. T. et al. CO<sub>2</sub> electroreduction to ethylene via hydroxide-mediated copper catalysis at an abrupt interface. *Science* (80-. ). **360**, 783–787 (2018).
37. Xiao, H., Cheng, T., Goddard, W. A. & Sundararaman, R. Mechanistic Explanation of the pH Dependence and Onset Potentials for Hydrocarbon Products from Electrochemical Reduction of CO on Cu (111). *J. Am. Chem. Soc.* **138**, 483–486 (2016).
38. Weng, L. C., Bell, A. T. & Weber, A. Z. Towards membrane-electrode assembly systems for CO<sub>2</sub> reduction: A modeling study. *Energy Environ. Sci.* **12**, 1950–1968 (2019).
39. Weekes, D. M., Salvatore, D. A., Reyes, A., Huang, A. & Berlinguette, C. P. Electrolytic CO<sub>2</sub> Reduction in a Flow Cell. *Acc. Chem. Res.* **51**, 910–918 (2018).
40. Delacourt, C., Ridgway, P. L., Kerr, J. B. & Newman, J. Design of an electrochemical cell making syngas (CO+ H<sub>2</sub>) from CO<sub>2</sub> and H<sub>2</sub>O reduction at room temperature. *J. Electrochem. Soc.* **155**, 42–49 (2008).
41. Verma, S., Lu, X., Ma, S., Masel, R. I. & Kenis, P. J. A. The effect of electrolyte composition on the electroreduction of CO<sub>2</sub> to CO on Ag based gas diffusion electrodes. *Phys. Chem. Chem. Phys.* **18**, 7075–7084 (2016).
42. Whipple, D. T., Finke, E. C. & Kenis, P. J. A. Microfluidic reactor for the electrochemical reduction of carbon dioxide: The effect of pH. *Electrochem. Solid-State Lett.* **13**, 109–111 (2010).
43. Lv, J. J. et al. A Highly Porous Copper Electrocatalyst for Carbon Dioxide Reduction. *Adv. Mater.* **30**, 1–8 (2018).
44. Salvatore, D. & Berlinguette, C. P. Voltage Matters When Reducing CO<sub>2</sub> in an Electrochemical Flow Cell. *ACS Energy Lett.* **5**, 215–220 (2020).

45. Kim, B., Hillman, F., Ariyoshi, M., Fujikawa, S. & Kenis, P. J. A. Effects of composition of the micro porous layer and the substrate on performance in the electrochemical reduction of CO<sub>2</sub> to CO. *J. Power Sources* **312**, 192–198 (2016).

## Chapter 2

### INVESTIGATION OF CO<sub>2</sub> SINGLE-PASS CONVERSION IN A FLOW ELECTROLYZER

In this chapter, I will be talking about the single-pass conversion for CO<sub>2</sub> electrolyzers, an important figure-of-merit often overlooked for CO<sub>2</sub> electrolyzers. This chapter is taken from the work published in *Reaction Chemistry & Engineering* (*React. Chem. Eng.*, 2020, 5, 1768-1775; DOI: 10.1039/D0RE00261E). Reproduced from Reaction Chemistry & Engineering with permission from the Royal Society of Chemistry (Appendix C).

#### 2.1 Introduction

There has been growing concern about the rapid increase of the atmospheric carbon dioxide (CO<sub>2</sub>) concentration causing global warming and climate change<sup>1</sup>. As a result, renewable energy resources, such as solar and wind, are being utilized more extensively to reduce the energy dependence on fossil sources<sup>2</sup>, which also leads to a significant cost reduction of renewable electricity production<sup>3,4</sup>. The low electricity price opens up potential opportunities for electricity driven chemical and fuel production using CO<sub>2</sub> as the carbon feedstock. For instance, CO<sub>2</sub> can be electrochemically converted into several products, including carbon monoxide (CO), formate, ethylene, and oxygenates, depending on the catalyst<sup>5-7</sup>. In the past few years, significant progress has been made in the development of CO<sub>2</sub> flow electrolyzers<sup>8-12</sup>, which enable high-rate CO<sub>2</sub> electroreduction reaction (eCO<sub>2</sub>RR) by allowing a direct feed of gaseous CO<sub>2</sub> reactant to the electrode-electrolyte interface through a gas-

diffusion layer (GDL). The employment of a GDL largely addresses the CO<sub>2</sub> mass transport limitations that are often seen in batch reactors where the current density is greatly limited by the low solubility of CO<sub>2</sub> in the aqueous electrolyte (~30 mM)<sup>13–15</sup>.

To date, the primary focus of flow cell studies in the literature has been the improvement of the performance of catalysts and gas-diffusion electrodes with higher current densities, better Faradaic efficiencies (FEs), and lower overpotentials of the eCO<sub>2</sub>RR. For example, Jiao et al. showed that a nanoporous copper (Cu) coated GDL was able to deliver a current density of 653 mA/cm<sup>2</sup> with a multi-carbon selectivity of 62% at -0.67 V vs Reversible Hydrogen Electrode (RHE)<sup>16</sup>. In a more recent study, Sargent et al. demonstrated eCO<sub>2</sub>RR at a current density up to 1.2 A/cm<sup>2</sup> together with a total eCO<sub>2</sub>RR FE of ~90% at a cell potential of 4.0 V in a flow electrolyzer, representing the state-of-the-art performance for CO<sub>2</sub> electrolysis in a flow cell<sup>17</sup>. While CO<sub>2</sub> flow electrolyzers show promising performances, much less attention has been devoted to engineering challenges related to CO<sub>2</sub> single-pass conversion in the flow cells, which is also an important aspect of the overall eCO<sub>2</sub>RR process because the CO<sub>2</sub> single-pass conversion is closely associated with the product separation cost. Taking eCO<sub>2</sub>RR to CO as an example, the separation cost of a gas product stream (i.e., a mixture of CO<sub>2</sub> and CO) by pressure swing adsorption is approximately 23% of the total operational costs at a 10% CO<sub>2</sub> single-pass conversion<sup>18</sup>. Theoretically, improving the CO<sub>2</sub> single-pass conversion to 50% will reduce the separation cost by 78% (i.e., 6% of the total cost)<sup>18</sup>. However, the flow cell studies in the literature often use a largely excessive amount of CO<sub>2</sub> in order to achieve high FEs and current densities, where the CO<sub>2</sub> single-pass conversion is typically lower than 10% (ESI Table 1) and usually not reported<sup>9,10,19–23</sup>.

In a flow electrolyzer, the CO<sub>2</sub> single-pass conversion could be influenced by many factors, such as the choice of CO<sub>2</sub> electrocatalyst, the configuration of the flow cell, the type of polymer membrane electrolyte, and the operating conditions (e.g., CO<sub>2</sub> feeding rate, applied potentials and reactor temperatures). Because of the complex nature, a systematic study would be appreciated to elucidate the interplay between CO<sub>2</sub> single-pass conversion with other parameters. In this paper, we chose a silver (Ag) based CO<sub>2</sub> flow electrolyzer as a model system to investigate the CO<sub>2</sub> single-pass conversion to CO. A series of experiments were conducted by varying the operating conditions, such as the CO<sub>2</sub> feeding rate, the applied current density, and the reactor temperature. The experimental results show that the CO<sub>2</sub> single-pass conversion through eCO<sub>2</sub>RR does not exceed 43% at all testing conditions, although a total consumption of CO<sub>2</sub> can be as high as 95%. The high consumption but low single-pass electrochemical conversion of CO<sub>2</sub> is mainly caused by the carbonate formation at the catalyst-electrolyte interface, a side-reaction that consumes up to 55% of the total CO<sub>2</sub> feed even when a neutral potassium bicarbonate electrolyte is used.

## **2.2 Experimental Methods**

### **2.2.1 Materials Preparation**

For both electrodes (cathode and anode), catalyst slurries were prepared by mixing 300 mg of catalyst powder, 1 mL of deionized water, 2 mL of isopropanol, and 100  $\mu$ m of Sustainion™ ionomer (Dioxide Materials). The cathode was prepared by spraying a slurry containing 100-nm Ag nanoparticles (Sigma-Aldrich) onto a 5×5 cm GDL (Sigracet 29BC) using a spray gun, and the catalyst loading was measured by using a balance, until a 1 mg/cm<sup>2</sup> loading of Ag catalyst was achieved. For the anode,

iridium oxide ( $\text{IrO}_2$ ) nanoparticles (Alfa-Aesar, Cat No. 43396) were used as the catalyst material and the rest of procedure is identical to the one for cathode. Anion exchange membranes (Sustainion™ membranes from Dioxide Materials) were used in the flow electrolyzers for all studies. The membranes were activated in 1 M potassium hydroxide (KOH) solution following a reported procedure<sup>24</sup>.

### **2.2.2 Electrolyzer Set-up**

In all experiments, a membrane electrode assembly (MEA) set-up was used, in which a Sustainion™ membrane was placed between the cathode and the anode. The MEA with an active electrode area of  $25 \text{ cm}^2$  was then put inside a flow electrolyzer made of two gold-plated stainless-steel plates ( $9.5 \times 9.5 \times 1 \text{ cm}$ ). The cathode plate has a multiple-channel serpentine flow field, whereas a single-channel serpentine flow field is used for the anode plate. The gold-plating on the stainless-steel plates prevent any potential issues with corrosion and side reactions (Figure A.1). Silicone gaskets with a thickness of 0.05 inch (McMaster Carr) were used for a good sealing. The plates were tightened by using a torque wrench at 20 lb-in torque, to ensure consistent contact distribution between the electrodes and the membrane for each test.

### **2.2.3 Electrolyzer Testing**

The  $\text{CO}_2$  gas feeding rate at the cathode chamber was set by a mass flow controller (MKS). On the anode side, a 0.05 M potassium bicarbonate ( $\text{KHCO}_3$ ) electrolyte was continuously circulated at a flow rate of approximately 70 mL/min using a peristaltic pump (Cole Parmer). The flow electrolyzer was then connected to an external power source (National Instruments), which controls the applied cell potentials or currents. The gas effluent of the flow electrolyzer was analyzed by an

inline gas chromatography (GC) (SRI) to quantify the gas products. The gas flow rate of the effluent was measured using a gas flow meter (Agilent), which is used for product quantifications. All the half-cell potentials reported in this study are adjusted to the RHE scale.

To calculate the CO<sub>2</sub> single-pass conversion to CO, the following equation was used:

$$\gamma_{CO} = \frac{x_{CO}Q_{outlet}}{Q_{inlet}}$$

where  $\gamma_{CO}$  is the fraction of CO<sub>2</sub> feed being converted electrocatalytically to CO,  $x_{CO}$  is the volume fraction of CO in the gas effluent quantified by the GC;  $Q_{outlet}$  is the flow rate of the gas effluent measured by the flow meter, and  $Q_{inlet}$  is the CO<sub>2</sub> feeding rate into the flow electrolyzer. The fraction of unreacted CO<sub>2</sub> was calculated similarly, except the volume fraction of CO<sub>2</sub> ( $x_{CO_2}$ ) instead of the mole fraction of CO was used. The following equation was used to calculate the fraction of CO<sub>2</sub> feed being converted to carbonates ( $\gamma_{carbonates}$ ) through side-reactions with hydroxide:

$$\gamma_{carbonates} = \frac{Q_{inlet} - (x_{CO} + x_{CO_2})Q_{outlet}}{Q_{inlet}}$$

For temperature effect studies, a 0.05 M KHCO<sub>3</sub> aqueous solution was used as the anolyte, which was preheated to the desired temperature (either 45°C or 60°C) using a heating mantle with a temperature controller (OptiChem). At the beginning of each test, both the CO<sub>2</sub> gas feed and the anolyte solution were continuously circulated until the temperature of the whole reactor reached the designated temperature. The rest of experimental procedure is identical to the one for room temperature tests.

### 2.3 Results and Discussion

There are multiple ways to configure the CO<sub>2</sub> flow electrolyzer. In this study, we conducted all experiments using a MEA type flow reactor as a model system, which is the most commonly used flow electrolyzer design for eCO<sub>2</sub>RR. A schematic representation of the flow electrolyzer configuration is shown in Figure 2.1a, where an anion exchange membrane is sandwiched between two electrodes. The cathode consists of a 25-cm<sup>2</sup> GDL coated with 100-nm Ag nanoparticles to facilitate the electroreduction of CO<sub>2</sub> to CO, whereas an IrO<sub>2</sub>-nanoparticle coated GDL is used as the anode for a stable performance in the neutral anolyte (i.e., 0.05 M KHCO<sub>3</sub>). A Sustainion membrane was chosen as the membrane material because it has a relatively high ionic conductivity in bicarbonate electrolytes in compared to other anion exchange membranes<sup>11,24</sup>. Figure 2.1b shows a zoom-in view of the gas-diffusion electrode (GDE) on the cathode side, where Ag nanoparticles are deposited on a hydrophobic GDL (Figure A.2) to facilitate the gas diffusion of reactant (i.e., CO<sub>2</sub>) and products (i.e., CO and H<sub>2</sub>) across the interface. On the surface of Ag catalyst, the CO<sub>2</sub> molecules are electrochemically reduced to CO and the water (H<sub>2</sub>O) molecules donate protons to form hydroxide anions. At the electrode-membrane interface, two side reactions, i.e., hydrogen evolution reaction through water reduction and carbonates formation between CO<sub>2</sub> and hydroxide anions, also occur simultaneously. Both reactions compete with eCO<sub>2</sub>RR and have significant impacts on the CO<sub>2</sub> single-pass conversion, which will be discussed in detail in the following paragraphs.

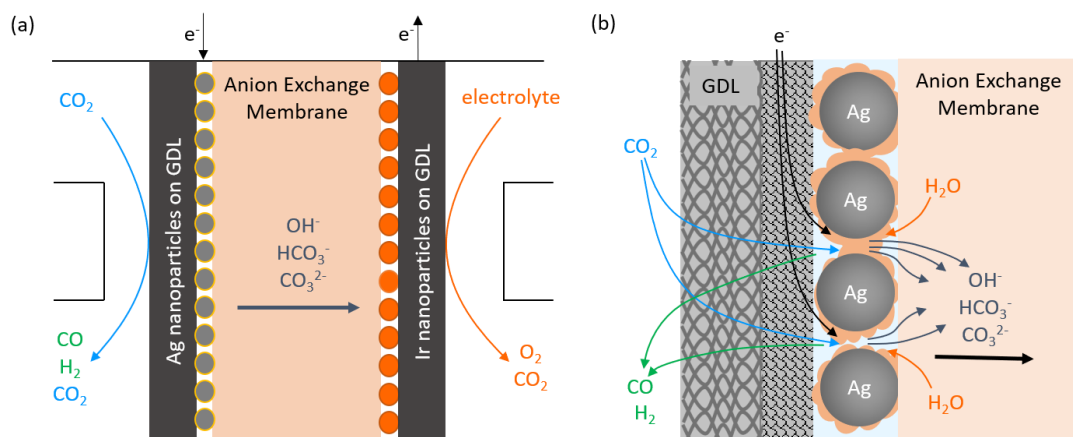


Figure 2.1: Schematic diagrams of (a) the CO<sub>2</sub> flow electrolyzer configuration and (b) the cathode-membrane interface with multiple competing reactions.

We first examined how the single-pass conversion of CO<sub>2</sub> is affected by applied cell potentials and CO<sub>2</sub> feeding rates. The cell potential was varied from 2.2 V to 3.9 V and the CO<sub>2</sub> feeding rate was set at 15-160 mL/min. As seen in Figure 2.2a, at low cell potentials (<2.8 V), the CO partial current densities are similar regardless of the CO<sub>2</sub> feeding rates, because the eCO<sub>2</sub>RR rate is controlled by kinetic activation and ohmic resistances<sup>25</sup>. When the cell voltage goes beyond 2.8 V, the CO partial current densities show a clear dependence on the CO<sub>2</sub> feeding rate, in which a greater CO partial current density was observed at a higher CO<sub>2</sub> feeding rate, suggesting that the system becomes CO<sub>2</sub> mass transport limited. Increasing the applied potential further resulted in a decrease in the CO partial current density, possibly due to more severe competing reactions, such as hydrogen evolution reaction, at high cell potentials.

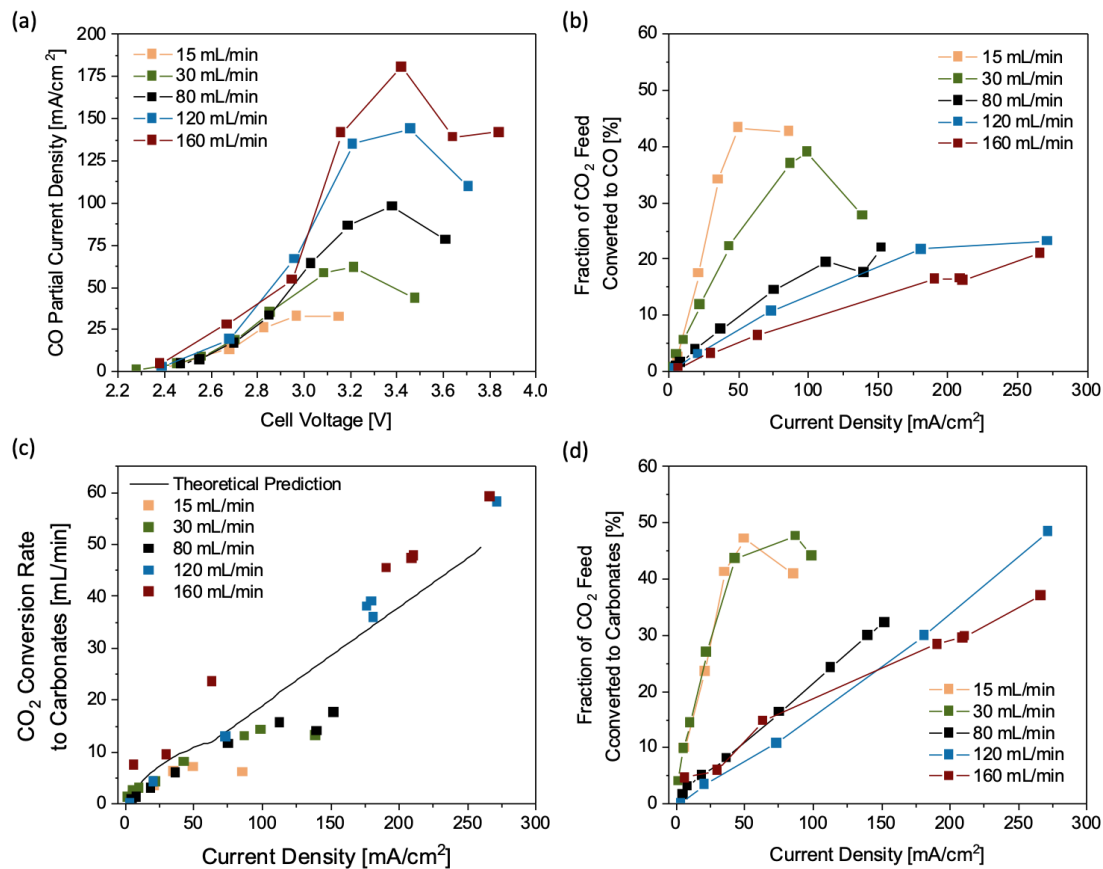


Figure 2.2: Performance of a 25-cm<sup>2</sup> flow electrolyzer operated at different CO<sub>2</sub> feeding rates: (a) CO partial current density profiles at various cell voltages, (b) fraction of CO<sub>2</sub> feed being converted to CO via eCO<sub>2</sub>RR, (c) rates of CO<sub>2</sub> being consumed due to carbonate formation, and (d) fraction of unreacted CO<sub>2</sub> feed at various current densities. The solid curve in (c) is the theoretical rate of CO<sub>2</sub> conversion to carbonates estimated by the Nernst-Planck equation (Appendix A.1).

Based on the CO partial current densities, the fractions of the CO<sub>2</sub> feed being converted electrocatalytically to CO are calculated (Figure 2.2b). At a CO<sub>2</sub> feeding rate of 15-30 mL/min, the maximum of CO<sub>2</sub> conversion to CO is 43% at a current density of 80 mA/cm<sup>2</sup>, corresponding to a current of 2 A. Further tuning the total applied current density and the CO<sub>2</sub> feeding rate did not result in a higher CO<sub>2</sub> single-

pass conversion, which is likely due to the carbonate formation at the electrode-membrane interface. During the eCO<sub>2</sub>RR, hydroxide ions are generated at the interface as a byproduct from the electroreduction process, which increases the local pH and consequently leads to the formation of carbonates, consuming a significant amount of CO<sub>2</sub> feed. At steady state, the reaction rate of carbonate formation with CO<sub>2</sub> and hydroxide should be equal to the rate of carbonate transport across the membrane. Since most of the ion transport across the membrane is dependent on electromigration<sup>26</sup> or the electric potential driving the ion transport, a modified version of the Nernst-Planck equation<sup>27</sup> can be used to estimate the flux of carbonates and bicarbonates expected to travel across the membrane based on the total current (Appendix A.1). This method enables us to calculate the CO<sub>2</sub> consumption due to the carbonate formation at the interface at any given current, which is shown as the theoretical prediction (a solid line) in Figure 2.2c. As the total current increases, the consumption rate of CO<sub>2</sub> to carbonates increases nearly linearly.

The amount of CO<sub>2</sub> that is consumed by the carbonate formation can also be estimated using the experimental data. Based on the product selectivity and the gas flow rates at the gas inlet and outlet of the CO<sub>2</sub> flow electrolyzer, we calculated the CO<sub>2</sub> consumption rates due to the carbonate formation at all flow rates and currents, which match the general trend of the theoretical prediction using the Nernst-Planck equation (Figure 2.2c). Assuming that the byproduct of the side reaction between CO<sub>2</sub> and hydroxide ions is exclusively carbonate (CO<sub>3</sub><sup>2-</sup>), the overall reaction at the cathode can be expressed as  $2\text{CO}_2 + 2\text{e}^- \rightarrow \text{CO} + \text{CO}_3^{2-}$ , suggesting that for every CO<sub>2</sub> molecule being converted to CO via eCO<sub>2</sub>RR there is another CO<sub>2</sub> molecule is consumed by the side reaction of carbonate formation. As a result, the theoretical CO<sub>2</sub>

conversion to CO is limited to approximately 50% regardless of the operating conditions of the flow electrolyzer, such as current densities and CO<sub>2</sub> feeding rates. The 50% conversion limit prediction is well supported by the experimental data shown in Figures 2.2b and 2.2d, indicating that CO<sub>3</sub><sup>2-</sup> is likely the dominant product of the side reaction between CO<sub>2</sub> and hydroxide.

We further examined the temperature effect on the CO<sub>2</sub> conversion to verify if the 50% limit of CO<sub>2</sub> conversion to CO is valid at elevated reaction temperatures. The reaction temperature of the flow electrolyzer was raised from room temperature to 45°C and 60°C, whereas the CO<sub>2</sub> feeding rate was maintained at 80 mL/min across all temperature effect studies. Figure 2.3a shows that a larger CO partial current density was obtained at lower overpotentials when the reaction temperature was increased, as expected based on the Butler-Volmer equation<sup>25</sup>. Additionally, the limiting CO partial current densities are 135 mA/cm<sup>2</sup> and 160 mA/cm<sup>2</sup> at 45°C and 60°C, respectively, a substantial improvement over 88 mA/cm<sup>2</sup> obtained at 25°C. The higher limiting CO partial current densities at elevated temperatures are likely due to the improved gas diffusivity of CO<sub>2</sub> to the catalyst surface<sup>28</sup>. At 60°C, about 40% of the CO<sub>2</sub> feed was converted to CO electrochemically (Figure 2.3b), which is twice as high as the CO<sub>2</sub> conversion obtained at 25°C, showing that the reaction temperature plays an important role in boosting the CO<sub>2</sub> single-pass conversion. On the other hand, the increase in reaction temperature also promoted the carbonate formation, resulting in a higher fraction of the CO<sub>2</sub> feed being converted to carbonates, as shown in Figure 2.3c. For a reaction temperature of 60°C, ~55% of the CO<sub>2</sub> feed formed carbonates, and consequently, less than 5% CO<sub>2</sub> was remained unreacted in the flow cell (Figure 2.3d). The results clearly show that increasing reaction temperature promotes not only the

electrochemical reduction of  $\text{CO}_2$  to  $\text{CO}$ , but also the side reaction of carbonate formation. Since the two reactions compete the  $\text{CO}_2$  feed and the reaction temperature affects both reaction rates in a similar way, it is not possible to improve the overall  $\text{CO}_2$  single-pass conversion to  $\text{CO}$  beyond 50% by simply changing the reaction temperature.

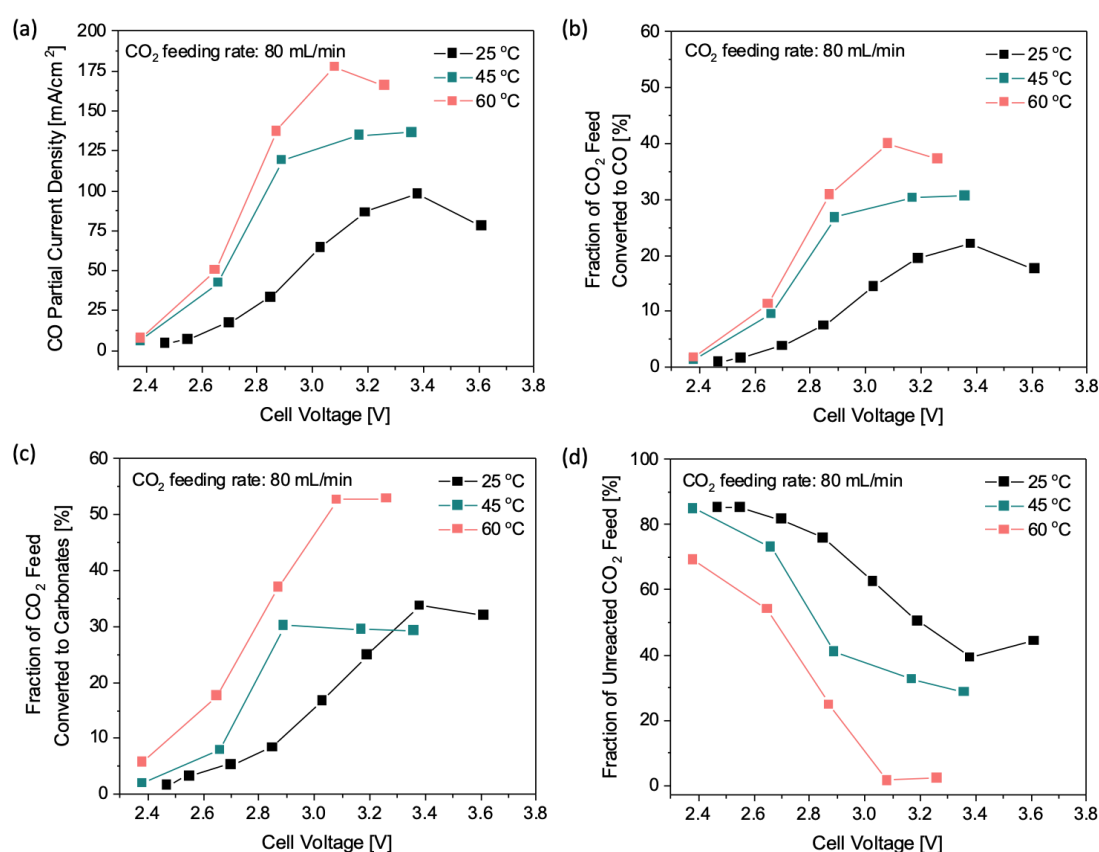


Figure 2.3: Effects of reaction temperature on the  $\text{CO}_2$  single-pass conversion at a fixed  $\text{CO}_2$  feeding rate of 80 mL/min: (a)  $\text{CO}$  partial current densities, (b) fraction of  $\text{CO}_2$  feed being converted to  $\text{CO}$  via  $\text{eCO}_2\text{RR}$ , (c) fraction of  $\text{CO}_2$  feed consumed by the carbonate formations, and (d) fraction of unreacted  $\text{CO}_2$  feed in the gas effluent at various cell voltages.

Although the CO<sub>2</sub> single-pass conversion to CO via eCO<sub>2</sub>RR is limited to less than 50%, the total consumption of the CO<sub>2</sub> feed can be as high as 95% (Figure 2.3d). As a result, the composition of the gas effluent from the cathode chamber is dominated by the gas product of CO at certain operating conditions. Such a phenomenon could be used as a potential strategy to generate a relatively pure gas product stream containing a limited amount of unreacted CO<sub>2</sub> without any gas separation processes. As shown in Figure 2.4, the gas effluent compositions are tunable by adjusting the operating current and CO<sub>2</sub> feeding rate to achieve a wide range of CO-to-H<sub>2</sub> ratios from 1 to 5. The presence of unreacted CO<sub>2</sub> in the gas product stream can be largely suppressed at relatively low CO<sub>2</sub> feeding rates. At optimal conditions, the highest concentration of CO in the gas product stream is ~80% together with ~15% H<sub>2</sub> and 5% unreacted CO<sub>2</sub>. For a fair comparison of the results at different current densities, the CO<sub>2</sub> feeding rates were normalized by the theoretical rate of eCO<sub>2</sub>RR estimated from the total current by assuming 2-electron per product molecule (Figure 2.4d). After normalizing the CO<sub>2</sub> feeding rate, the CO fractions in the gas effluent streams at different current densities all show a maximum value of ~1.75, suggesting that the maximum CO concentration in the gas product stream is mainly controlled by the ratio between the amount of the CO<sub>2</sub> feed and the operating current.

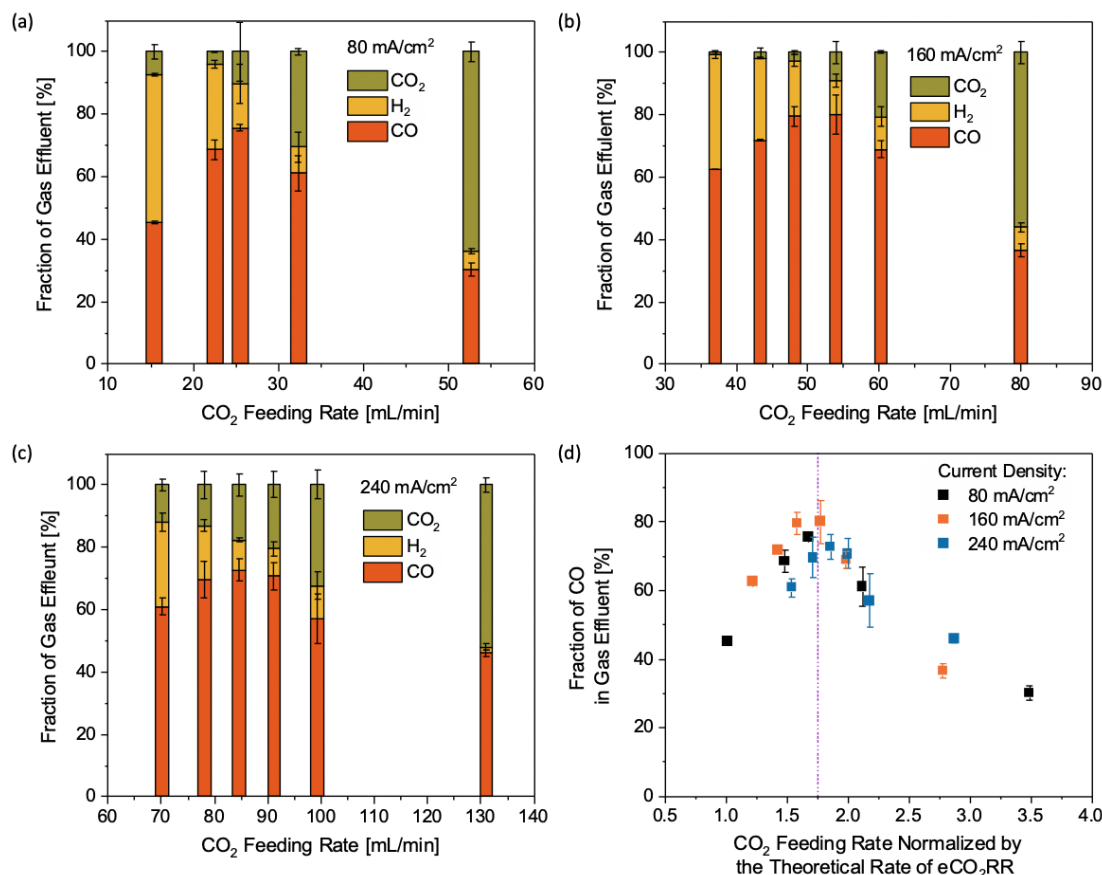


Figure 2.4: Compositions of the gas effluent from the cathode chamber of a CO<sub>2</sub> flow electrolyzer (25-cm<sup>2</sup> active electrode area) at different operating current densities: (a) 80 mA/cm<sup>2</sup>, (b) 160 mA/cm<sup>2</sup>, and (c) 240 mA/cm<sup>2</sup>. (d) is a comparison among the fractions of CO in the gas product streams under different operating conditions. The x-axis of (d) is the CO<sub>2</sub> feeding rate [mL/min] divided by the theoretical rate of eCO<sub>2</sub>RR [mL/min], estimated from the total current.

All the results presented in this work suggest that the 50% limit of CO<sub>2</sub> single-pass conversion is a fundamental challenge in anion-exchange-membrane-based CO<sub>2</sub> flow electrolyzers. The locally generated hydroxide anions from eCO<sub>2</sub>RR inevitably react with CO<sub>2</sub> to form carbonates even when a neutral pH supporting electrolyte is used. Switching the anion exchange membrane to a proton exchange membrane could

avoid the carbonate formation at the interface; however, the strong acidic environment likely promotes hydrogen evolution reaction, an undesired reaction competing with eCO<sub>2</sub>RR at the cathode<sup>29</sup>. Employment of a bipolar membrane combined with a bicarbonate<sup>23</sup> or carbonate<sup>30</sup> supporting electrolyte could be a potential solution. To date, the CO FEs for most bipolar-membrane-based flow electrolyzers are still relatively low at industrially relevant current densities ( $>100 \text{ mA/cm}^2$ ). Another alternative could be a non-aqueous electrolyte system. In that case, a beneficial organic oxidation reaction could be considered as an alternative to the water oxidation reaction for anode and act as the proton source for CO<sub>2</sub> reduction on the cathode. Several technical challenges associated with organic electrolytes include the suppression of hydrogen evolution in an acidic environment, relatively low ionic conductivity of organic electrolytes to support cell operation under high current densities, and decomposition of organic electrolytes on the anode. More research efforts are needed to develop new strategies for a high CO<sub>2</sub> single-pass conversion together with a high CO selectivity at large current densities in CO<sub>2</sub> flow electrolyzers.

## 2.4 Conclusion

In summary, we studied the potential impacts of current densities, CO<sub>2</sub> feeding rates, and reaction temperatures on the single-pass conversion of CO<sub>2</sub> in a typical CO<sub>2</sub> flow electrolyzer. The CO<sub>2</sub> single-pass conversion to CO is limited to ~43% regardless of operating conditions, which is due to the carbonate formation reaction between the CO<sub>2</sub> feed and the locally generated hydroxide ions. The side reaction consumes a substantial fraction of the CO<sub>2</sub> feed and leaves a very small amount of unreacted CO<sub>2</sub> in the system. At certain conditions, nearly 95% of the CO<sub>2</sub> feed are consumed through either eCO<sub>2</sub>RR or the carbonate formation reaction. Because of the

high CO<sub>2</sub> consumption, the gas product stream from the cathode chamber contains predominately CO (80%) and a small amount of H<sub>2</sub> (15%) and unreacted CO<sub>2</sub> (5%), which could be considered as a potential strategy to produce a relatively concentrated product stream without any gas separation processes.

## **2.5 Acknowledgements**

I would like to thank Dr. Brian Setzler for his help regarding the calculations for carbonate formation. In addition, I would like to thank Neil Garrett for his help in setting up the power supply, and Alfred Lance and Brian Brant in machine shop for fabricating the electrolyzer plates. Finally, I would like to acknowledge the financial support from the NASA DE Space Grant Graduate Fellowship.

## REFERENCES

1. NASA. Carbon Dioxide | Vital Signs – Climate Change: Vital Signs of the Planet.
2. Energy Information Administration, U.S. Annual Energy Outlook 2019 with projections to 2050 (2019).
3. Davis, S. J., Lewis, N. S., Shaner, M. Aggarwal, S., Arent, D., Azevedo, I. L., Benson, S. M., Bradley, T. Brouwer, J., Chiang, Y., Clack, C. T. M., Cohen, A., Soig, S. Edmonds, J., Fennell, P., Field, C. B., Hannegan, B., Hodge, B., Hoffert, M. I., Ingersoll, E., Jaramillo, P., Lackner, K. S., Mach, K. J., Mastrandrea, M., Ogden, J., Peterson, P. F., Sanchez, D. L., Sperling, D., Stagner, J., Trancik, J., Yang, C., Caldeira, K. Net-zero emissions energy systems. *Science* **360**, eaas9793 (2018).
4. Haegel, N. M., Margolis, R., Buonassisi, T., Feldman, D., Froitzheim, A., Garabedian, R., Green, M., Glunz, S., Henning, H., Holder, B., Kaizuka, I., Kroposki, B., Matsubara, K., Niki, S., Sakurai, K., Schindler, R. A., Tumas, W., Weber, E. R., Wilson, G., Woodhouse, M., Kurtz, S. Terawatt-scale photovoltaics: Trajectories and challenges. *Science* **356**, 141–143 (2017).
5. Hori, Y. Electrochemical CO<sub>2</sub> Reduction on Metal Electrodes. *Mod. Asp. Electrochem.* **42**, 89–189 (2008).
6. Kuhl, K. P., Cave, E. R., Abram, D. N. & Jaramillo, T. F. New insights into the electrochemical reduction of carbon dioxide on metallic copper surfaces. *Energy Environ. Sci.* **5**, 7050–7059 (2012).
7. Ju, W., Bagger, A., Hao, G. P., Varela, A. S., Sinev, I., Bon, V., Roldan Cuenya, B., Kaskel, S., Rossmeisl, J., Strasser, P. Understanding activity and selectivity of metal-nitrogen-doped carbon catalysts for electrochemical reduction of CO<sub>2</sub>. *Nat. Commun.* **8**, 944 (2017).
8. Verma, S., Hamasaki, Y., Kim, C., Huang, W., Lu, S., Jhong, H. R. M., Gewirth, A. A., Fujigaya, T., Nakashima, N., Kenis, P. J.A. Insights into the Low Overpotential Electroreduction of CO<sub>2</sub> to CO on a Supported Gold Catalyst in an Alkaline Flow Electrolyzer. *ACS Energy Lett.* **3**, 193–198 (2018).

9. Dinh, C. T., García De Arquer, F. P., Sinton, D. & Sargent, E. H. High rate, Selective, and Stable Electroreduction of CO<sub>2</sub> to CO in Basic and Neutral Media. *ACS Energy Lett.* **3**, 2835–2840 (2018).
10. Gabardo, C. M., Seifitokaldani, A., Edwards, J. P., Dinh, C. T., Burdyny, T., Kibria, M. G., O'Brien, C. P., Sargent, E. H., Sinton, D. Combined high alkalinity and pressurization enable efficient CO<sub>2</sub> electroreduction to CO. *Energy Environ. Sci.* **11**, 2531–2539 (2018).
11. Liu, Z., Yang, H., Kutz, R. & Masel, R. I. CO<sub>2</sub> Electrolysis to CO and O<sub>2</sub> at High Selectivity, Stability and Efficiency Using Sustainion Membranes. *J. Electrochem. Soc.* **165**, J3371–J3377 (2018).
12. Xia, C., Zhu, P., Jiang, Q., Pan, Y., Liang, W., Stavitsk, E., Alshareef, H. N., Wang, H. Continuous production of pure liquid fuel solutions via electrocatalytic CO<sub>2</sub> reduction using solid-electrolyte devices. *Nat. Energy* **4**, 776–785 (2019).
13. Endrődi, B., Bencsik, G., Darvas, F., Rajeshwar, K., Janáky, C. Continuous-flow electroreduction of carbon dioxide. *Progress in Energy and Combustion Science* **62** 133–154 (2017).
14. Weekes, D. M., Salvatore, D. A., Reyes, A., Huang, A. & Berlinguette, C. P. Electrolytic CO<sub>2</sub> Reduction in a Flow Cell. *Acc. Chem. Res.* **51**, 910–918 (2018).
15. Burdyny, T. & Smith, W. A. CO<sub>2</sub> reduction on gas-diffusion electrodes and why catalytic performance must be assessed at commercially-relevant conditions. *Energy Environ. Sci.* **12**, 1442–1453 (2019).
16. Lv, J. J., Jouny, M., Luc, W., Zhu, W., Zhu, J. J., Jiao, F. *Adv. Mater.* **30**, 1803111 (2018).
17. García de Arquer, F. P., Dinh, C. T., Ozden, A., Wicks, J., McCallum, C., Kirmani, A. R., Nam, D. H., Gabardo, C., Seifitokaldani, A., Wang, X., Li, Y. C., Li, F., Edwards, J., Richter, L. J., Thorpe, S. J., Sinton, D., Sargent, E. H. CO<sub>2</sub> electrolysis to multicarbon products at activities greater than 1 A cm<sup>-2</sup>. *Science*. **367**, 661–666 (2020).
18. Jouny, M., Luc, W. & Jiao, F. General Techno-Economic Analysis of CO<sub>2</sub> Electrolysis Systems. *Ind. Eng. Chem. Res.* **57**, 2165–2177 (2018).

19. Dufek, E. J., Lister, T. E., Stone, S. G. & McIlwain, M. E. Operation of a Pressurized System for Continuous Reduction of CO<sub>2</sub>. *J. Electrochem. Soc.* **159**, F514–F517 (2012).
20. Ma, S., Lan, Y., Perez, G. M. J., Moniri, S. & Kenis, P. J. A. Silver supported on titania as an active catalyst for electrochemical carbon dioxide reduction. *ChemSusChem* **7**, 866–874 (2014).
21. Möller, T., Ju, W., Bagger, A., Wang, X., Luo, F., Ngo Thanh, T., Varela, A. S., Rossmeisl, J., Strasser, P. Efficient CO<sub>2</sub> to CO electrolysis on solid Ni-N-C catalysts at industrial current densities. *Energy Environ. Sci.* **12**, 640–647 (2019).
22. Salvatore, D. A., Weekes, D. M., He, J., Dettelbach, K. E., Li, Y. C., Mallouk, T. E., Berlinguette, C. P. Electrolysis of Gaseous CO<sub>2</sub> to CO in a Flow Cell with a Bipolar Membrane. *ACS Energy Lett.* **3**, 149–154 (2018).
23. Li, T. Lees, E. W., Goldman, M., Salvatore, D. A., Weekes, D. M., Berlinguette, C. P. Electrolytic Conversion of Bicarbonate into CO in a Flow Cell. *Joule* **3**, 1487–1497 (2019).
24. Kutz, R. B., Chen, Q., Yang, H., Sajjad, S. D., Liu, Z., Masel, R. I. Sustainion Imidazolium-Functionalized Polymers for Carbon Dioxide Electrolysis. *Energy Technol.* **5**, 929–936 (2017).
25. Eliaz, N. & Gileadi, E. Physical Electrochemistry. 1–8 (2000).
26. Luo, T., Abdu, S. & Wessling, M. Selectivity of ion exchange membranes: A review. *J. Memb. Sci.* **555**, 429–454 (2018).
27. Lakshminarayanaiah, N. Transport Phenomena in Artificial Membranes. *Chem. Rev.* **65**, 492–565 (1965).
28. Ozen, D. N., Timurkutluk, B. & Altinisik, K. Effects of operation temperature and reactant gas humidity levels on performance of PEM fuel cells. *Renew. Sustain. Energy Rev.* **59**, 1298–1306 (2016).
29. Delacourt, C., Ridgway, P. L., Kerr, J. B. & Newman, J. Design of an electrochemical cell making syngas (CO+ H<sub>2</sub>) from CO<sub>2</sub> and H<sub>2</sub>O reduction at room temperature. *J. Electrochem. Soc.* **155**, 42–49 (2008).
30. Li, Y. C., Lee, G., Yuan, T., Wang, Y., Nam, D., Wang, Z., Garcia de Arquer, F. P., Lum, Y., Dinh, C., Voznyy, O., Sargent, E. H. CO<sub>2</sub> Electroreduction from Carbonate Electrolyte. *ACS Energy Lett.* **4**, 1427–1431 (2019).

## Chapter 3

### SCALABLE GAS DIFFUSION ELECTRODE FABRICATION FOR ELECTROCHEMICAL CO<sub>2</sub> REDUCTION USING PHYSICAL VAPOR DEPOSITION METHODS

In this chapter, I switch to discussing experiments involving the three-compartment microfluidic flow cell electrolyzer, specifically concentrating on catalyst preparation and integration for these electrolyzers. This chapter was the work done in collaboration with Lawrence Livermore National Laboratory, who had provided the samples and characterization. I have conducted the electrochemical tests for these samples presented in this chapter.

#### 3.1 Introduction

Coupling electrochemical conversion of the greenhouse gas CO<sub>2</sub> with renewable electricity sources such as solar and wind promises carbon-neutral production of high-demand chemicals and transportation fuels for a high-productivity, sustainable future.<sup>1,2</sup> This technology becomes increasingly competitive as prices of electricity from renewable energy resources continue to decrease.<sup>3</sup> Potential eCO<sub>2</sub>RR products, such as ethylene, ethanol, and acetic acid, can be used to feed industrial chemical process lines and power vehicles.<sup>1,2,4</sup> At the same time, eCO<sub>2</sub>RR provides an economical pathway for large-scale, seasonal storage of intermittent renewable electric energy. Much work has been devoted to developing more efficient electrochemical membrane reactor designs and catalyst materials.<sup>5-10</sup> Both microfluidic and zero-gap gas diffusion electrolyzer designs have shown great potential for

realization of high current density eCO<sub>2</sub>RR by delivering the reactant CO<sub>2</sub> to the catalyst in the gas phase.<sup>5,11-14</sup> The four orders of magnitude higher diffusivity of CO<sub>2</sub> gas (16 mm<sup>2</sup>/s) compared to CO<sub>2</sub> in an aqueous solution (0.0016 mm<sup>2</sup>/s) effectively mitigates mass transport limitations.<sup>15</sup> These reactor designs require good control of the interface between the catalyst, electrolyte, and membrane because the overall performance of the CO<sub>2</sub> electrolyzer is largely influenced by the nature of these interfaces. For instance, a low hydrophobicity of the electrode-electrolyte interface likely causes flooding issues thus preventing the reactant (i.e., CO<sub>2</sub> gas) from reaching the catalyst for the reaction.<sup>5</sup> Many of the electrodes used in electrolyzer studies are fabricated through the deposition of the catalyst onto a porous carbon paper commonly known as the gas diffusion layer (GDL). The GDL consists of a fibrous backing for efficient mass transport and a microporous carbon layer as catalyst support. Both layers contain polytetrafluoroethylene (PTFE) to increase hydrophobicity for reducing the risk of flooding. Replacing the carbon backing by a PTFE layer, or tuning the PTFE content in the microporous layer have both been used to further improve the GDL's flooding resilience.<sup>5</sup>

So far, copper and its alloys remain the only catalysts that have been demonstrated to efficiently convert CO<sub>2</sub> into multi-carbon (C<sub>2+</sub>) products, such as ethylene, ethanol, acetate, and propanol. Previous studies focused primarily on understanding the effect of the copper catalyst morphology and composition on the eCO<sub>2</sub>RR performance.<sup>6,8,9,16-23</sup> Compared to catalyst and electrolyzer design, far fewer studies have addressed catalyst integration despite its critical importance on overall device performance and electrolyzer size upscaling. Hand, screen, spray, and inkjet painting are frequently used methods for applying the catalyst coating on the GDL or

the electrolyzer membrane.<sup>24-26</sup> While all these methods are scalable towards larger electrodes and generally can provide good thickness and uniformity control (with exception of hand brush painting), they require development of suitable and stable particle-based ink systems. Furthermore, the particle character of the resulting catalyst coatings can cause poor electrical connectivity and mechanical properties. For example, Kenis *et al* reported on the effect of ink slurry deposition on eCO<sub>2</sub>RR performance, comparing hand painting, air brushing, and screen printing methods.<sup>24</sup> But despite critical importance for industrial applications, few studies have systematically addressed the effect of deposition method and Cu catalyst coating thickness on eCO<sub>2</sub>RR performance, especially for a flow cell electrolyzer configuration.

In this work, we used physical vapor deposition methods to systematically explore the effect of Cu catalyst coating thickness and morphology on eCO<sub>2</sub>RR activity and selectivity in a three-compartment microfluidic electrolyzer. Compared to ink-based methods, physical vapor deposition methods provide superior control over thickness, especially at low catalyst loadings, while their monolithic character reduces the contact resistance and provides mechanical stability. Here, we used electron beam (EB) deposition and magnetron sputtering (MS) to deposit Cu coatings of various thicknesses on commercial GDLs. Both methods have the potential for large scale production, allow for direct coating of the electrocatalyst on the GDL, provide excellent thickness control and coating uniformity combined with high specific surface area. More importantly, they are also scalable to very large electrode areas ( $\sim 10^4$  cm<sup>2</sup>) and enable efficient integration and compositional tuning of Cu alloy catalysts including non-thermodynamic equilibrium alloy compositions that would be

difficult to synthesize and integrate otherwise. Using a microfluidic gas diffusion electrolyzer, we observed that EB-Cu coatings generally provide better performance than the MS-Cu catalyst coatings in terms of current density, selectivity, and energy efficiency, with an optimum thickness of 400 nm where the energy efficiency (i.e., sum over the Faradaic Efficiency times theoretical cell potential divided by the applied potential for all eCO<sub>2</sub>RR products, for details see below) reaches 56.5%. Scanning and transmission electron microscopy (SEM/TEM), Rutherford backscatter analysis (RBA), electrochemical surface area (ECSA) measurements, and contact angle measurements suggest that the generally better eCO<sub>2</sub>RR performance of EB-Cu coatings correlates with the GDL/Cu catalyst morphology making the EB-Cu catalyst layer more hydrophobic.

## **3.2 Methods**

### **3.2.1 Catalyst Coatings**

100-800 nm thick Cu films (Cu loading: 0.09 - 0.72 mg/cm<sup>2</sup>) were deposited onto 25-600 cm<sup>2</sup> GDL substrates (Sigracet, BC 39) by both direct current (DC) magnetron sputtering (MS) and electron beam (EB) evaporation. Before coating, the GDL substrates were loaded into the respective deposition systems and pumped overnight to a base pressure in the 10<sup>-7</sup> Torr range. The MS-Cu coatings were prepared at room temperature in a custom-built deposition chamber equipped with a three-inch magnetron sputtering gun and using a pure copper target (Process Materials Inc, 99.99%), research grade Argon (99.9999%, chamber pressure 2 mTorr, flow rate 20 sccm) as a sputter gas, and a DC plasma power between 25 W and 100 W. Before every coating, the Cu target was pre-sputtered on the back of a shutter for

approximately five minutes to remove any oxide layer on the surface of the copper target. Calibration runs were performed to determine the deposition rate by measuring the film thickness on a silicon reference wafers with an Alpha-Step D-600 Stylus profilometer (KLA Tencor). The EB coatings were prepared in a custom-built EB system with a 10-kV power supply (Temescal) and a pure 15cc copper starter source (Process Materials Inc, 99.99%). The power supply was operated at 6.5 kV, operating between 25-35% power to achieve deposition rates between 1.8 and 2.5 Å/s. A quartz crystal monitor (calibrated against a silicon witness sample) was utilized for in-situ monitoring the coating thickness.

### **3.2.2 Materials Characterization**

Transmission electron microscopy (TEM) measurements were performed on a FEI Titan 80 – 300 (scanning) transmission electron microscope operated at 300 kV. TEM samples were prepared by scratching the GDL Cu coatings with a clean scalpel blade and subsequently rubbing them against a lacey carbon TEM grid. The material composition was confirmed via energy dispersive x-ray spectroscopy (EDS) using the SuperX G2 detector in the Titan. Scanning electron microscope (SEM) measurements were performed on an Apreo SEM (Thermo Scientific) operated at an accelerating voltage of 5 keV with a working distance of 8 mm. For characterization of the Cu catalyst after long-term stability testing, SEM measurements were conducted on an Auriga 60 CrossBeam system.

The thickness and depth distribution of Cu in the Cu/GDLs was studied by Rutherford backscattering spectrometry (RBS)<sup>27</sup> using 2 MeV  $4\text{He}^+$  ions incident between 0 and 10° to the sample surface (to minimize ion channeling in the textured films) and backscattered into a detector at 164° from the incident beam direction. To extract the Cu depth distribution in the

Cu coated GDLs we used the RUMP code.<sup>28</sup> In the RUMP simulations, the film was sliced into multiple layers to obtain the concentration depth profile. Conversion into depth scale assumes that the carbon in the microporous carbon (MPC) layer has a full density of 2.25 g/cc and a porosity of 75%.

For X-ray photoelectron spectroscopy (XPS) analysis of the spent catalyst after stability testing, the post reaction Cu electrode was first taken out of the electrolyzer, followed by washing with deionized water and drying. The electrode was stored in a vial filled with Ar before being analyzed using the XPS equipment (K-alpha Alpha X-ray photoelectron spectrometer system, Thermo Fisher Scientific). During the whole procedure, the electrode was exposed to air for less than 30 minutes. High-resolution XPS measurements were obtained at a pass energy of 20 eV with a step size of 0.1 eV. Flood gun was turned on, and Cu 2p was scanned 10 times. All peaks were fitted using Thermo Advantage software with adventitious carbon referenced to the C1s peak at 284.8 eV.

### **3.2.3 Electrochemical active surface area analysis (ECSA)**

Cu foil (Alfa Aesar), EB and MS-Cu samples were cut into 0.5 cm × 2 cm pieces and attached to a nickel wire using colloidal silver paint. The ECSA measurements were performed in a H-cell using a three-electrode configuration with a graphite rod counter electrode and a Ag/AgCl reference electrode, and a 0.1 M HClO<sub>4</sub> electrolyte under Ar atmosphere. For each sample, we recorded a series of cyclic voltammograms (CVs) in the pure double layer capacitance (C<sub>dl</sub>) potential range (-0.12 V to 0.07 V vs. RHE) at scan rates ranging from 20 mV/s to 100 mV/s. The C<sub>dl</sub> values were then calculated from current densities vs. scan rate plots. The ECSA of each sample and the corresponding roughness factor were obtained by normalizing the measured C<sub>dl</sub> values to the C<sub>dl</sub> value obtained from a Cu foil.

### 3.2.4 Electrochemical Testing

The copper coated GDLs were cut into 0.5 cm × 2 cm pieces to fit into microfluidic flow cell set-up described previously<sup>2</sup> (Fig. B.1). Most of the electrochemical measurements were performed in a three-electrode configuration with a Hg/HgO reference electrode and an iridium coated carbon paper with a titanium foil current collector as the counter electrode. CO<sub>2</sub> was regulated with a mass flow controller (MKS Instruments) at a rate of 15 sccm, and 1 M KOH was used as both catholyte and anolyte and fed at a rate of 1.5 ml/min using peristaltic pumps. The gas flow rates at the electrolyzer outlet were monitored using a gas flow meter (Agilent); no significant loss of CO<sub>2</sub> due to reaction with the 1 M KOH catholyte was found, and thus no corrections of the FE data were needed. After setting up the testing station, the current interrupt procedure was applied to measure the resistance before testing. No trend for resistance *vs* thickness was observed. The tests were conducted at constant current mode using a potentiostat (Autolab), and the potentials were recorded at the times of sample collection and corrected with the pH of the electrolyte and the measured resistance to the Reversible Hydrogen Electrode (RHE) scale ( $V [vs RHE] = V [Hg/HgO] + 0.098 + 0.059 \times 14 + I \times R$ , where  $I$  is the current density and  $R$  is the measured resistance). To quantify the products, the gas outlet was fed to the GC (SRI Instruments), and liquid electrolyte samples were collected at different times, diluted with DI water, and analyzed through NMR (AVIII 600).

### 3.3 Results and Discussion

The microstructure of EB- and MS-Cu coatings on the MPC top layer of the GDLs was characterized by SEM and TEM (Fig. 3.1). While the Cu coatings fabricated by both methods become increasingly dense with increasing coating

thickness, even the thickest, 800 nm thick Cu films on the porous GDL substrate remain porous in nature (Fig. B.2). The open porous microstructure of the Cu coatings is a critical feature for eCO<sub>2</sub>RR as it enables fast transport of the gaseous reactant CO<sub>2</sub> through the GDL to the catalyst layer as required for realization of high eCO<sub>2</sub>RR current densities ( $> 100 \text{ mA/cm}^2$ ). A comparison of SEM images collected from the top surface of nominally 400 nm thick EB (Fig. 3.1a) and MS (Fig. 3.1b) Cu coatings reveals that both films consist of 100-400 nm diameter Cu particles. However, the EB-Cu nanoparticles seem to have more well-defined facets, while the MS-Cu particles have a very rough and serrated appearance. The corresponding cross-sectional SEM images (Fig. 3.1c and d) confirm the open porous character of the Cu coatings and suggest the presence of a relatively sharp transition between the MPC layer (dark) of the GDL and the Cu catalyst layer (bright). TEM further confirms the more ordered, faceted nature of the EB-Cu coatings suggested by the SEM images. The EB-Cu particles consist of well-defined grains of about 10 nm and have a faceted surface (Fig. 3.1e); the MS-Cu particles seem to be composed of smaller, irregular shaped nanocrystals (Fig. 3.1f), and the surface is very rough even at the highest resolution.

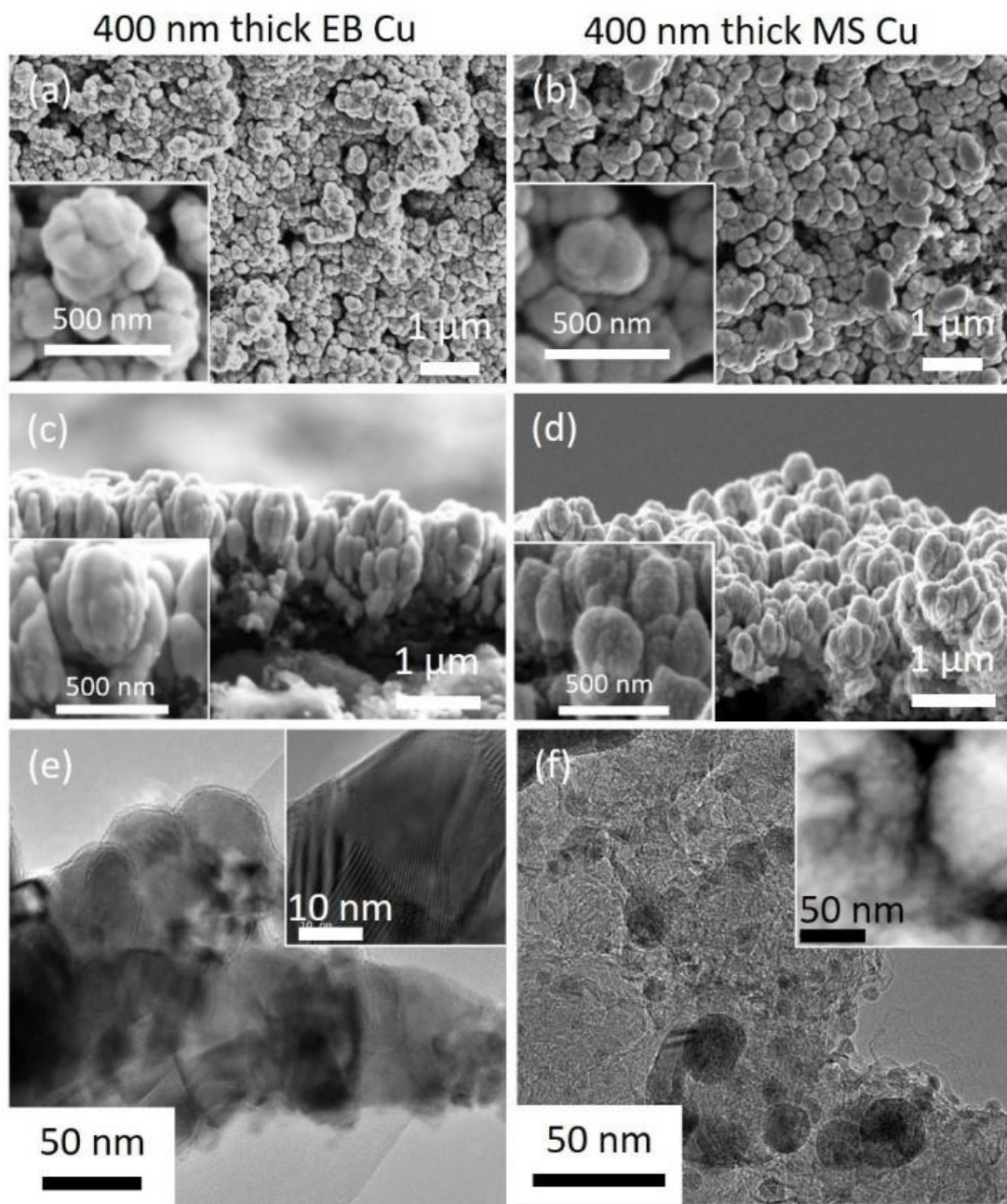


Figure 3.1: Characterization of Cu catalyst coatings: Top view SEM micrographs of (a) 400 nm thick EB and (b) MS Cu coatings on GDLs, as well as the corresponding cross-sectional SEM images (c,d); TEM micrographs of 100-nm-thick EB (e) and MS (d) Cu coatings.

For a more quantitative characterization of the depth distribution of the Cu coatings on and within the MPC layer of the GDLs, we turned to Rutherford backscattering spectrometry. Representative RBS spectra of nominally 400 nm thick EB- and MS-Cu coatings on the GDL substrate are shown in Fig. 3.2a and 3.2b, respectively. Composition and depth distribution (Fig. 3.2c) of the Cu coatings were obtained by fitting of the RBS spectra shown in Fig. 3.2a,b using RUMP code<sup>28</sup> simulations. The surface peaks of  $^{64}\text{Cu}$ ,  $^{19}\text{F}$  (from the PTFE content of the MPC layer of the GDL), and  $^{12}\text{C}$  are marked by arrows. The actual thickness of the Cu coating was estimated by fitting the RBS signal between the Cu surface peak and the 50% signal on the low energy side of the spectra (dashed line in Fig. 3.2a,b). The coating thickness thus derived is in good agreement with the nominal thicknesses predicted from the measured Cu deposition rates on flat substrates; for example, for nominally 400 nm thick EB- and MS-Cu films the RBS Cu coating thickness is 394 and 358 nm, respectively. The signal between the Cu surface peak and the Cu/MPC-PTFE interface (marked by  $\downarrow\text{Cu/PTFE}$ ) corresponds to pure Cu deposited *on top* of the MPC layer of the GDL. Here, the Cu/MPC-PTFE interface is defined by the first data point where the measured signal drops 10% below the simulated signal for pure copper (dashed line in Fig. 3.2a,b). The spectral intensity in the region between the Cu/MPC-PTFE interface and the  $^{19}\text{F}$  surface peak can be attributed to Cu deposited *within* the MPC layer of the GDL, and the solid line is the result of a RUMP code simulation based on fitted Cu-to-C atomic ratio depth profiles shown in Fig. 3.2c. The depth profile analysis reveals that the Cu-to-C ratio in the MPC layer of the EB coated GDL is lower than that of the MS GDL. The higher gas pressure used for magnetron sputtering seems to facilitate the deposition of Cu *within* the MPC layer of the GDL.

Similar trends were observed for both thinner and thicker Cu coatings, although the effect seems to become less pronounced for thicker coatings. Both the different surface morphology revealed by SEM and TEM (Fig. 3.1) and the different Cu-MPC interface (Fig 3.2a-c) can be expected to affect the nature of the solid/liquid/gas triple phase junctions that are critical for the performance of a GDE.

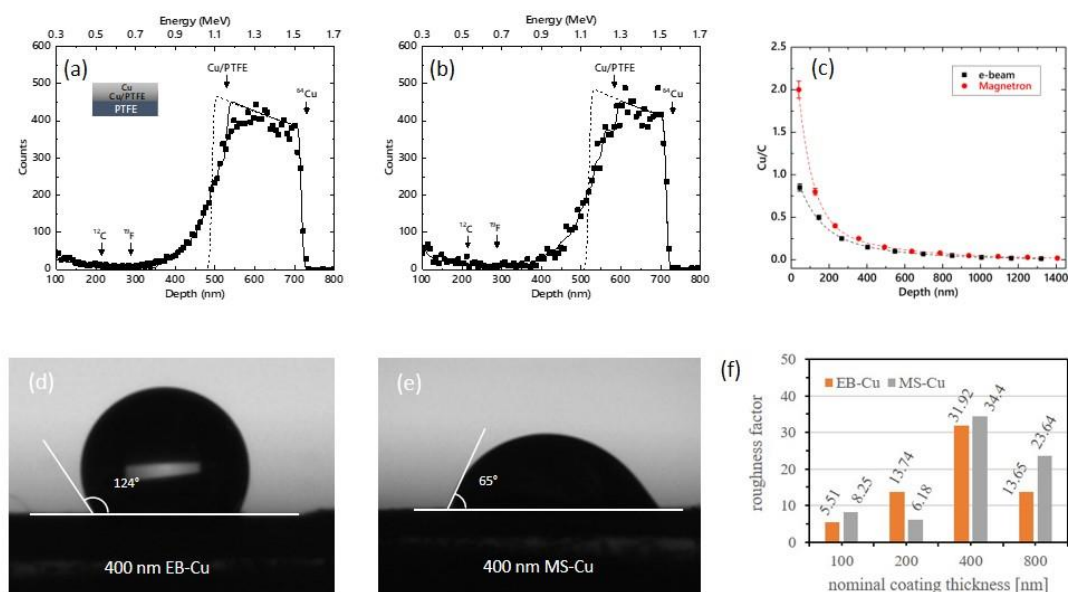


Figure 3.2: RBS spectra from GDLs with nominally 400 nm thick EB-Cu (a) and MS-Cu (b) coatings. The surface peaks of  $^{64}\text{Cu}$ ,  $^{19}\text{F}$  (from the PTFE content of the MPC layer), and  $^{12}\text{C}$  are denoted by arrows. Dashed lines are RUMP simulations for 394 (a) and 358 nm (b) fully dense Cu coatings on MPC, and solid lines are the result of RUMP code simulations reflecting the Cu-to-C depth distribution in the MPC layer shown in (c); contact angle measurements on GDLs with nominally 400 nm thick EB (d) and MS-Cu (e) coatings; (f) EB/MS-Cu roughness factor vs. thickness values derived from EASA measurements shown in Fig. B.4 and B.5.

Contact angle measurements on GDLs with nominally 400 nm thick EB (Fig. 3.2d) and MS (Fig. 3.2e) Cu films indeed confirm that the different surface and

MPC/Cu interface morphology of EB and MS films affects the wetting behavior of the Cu coated GDLs. With a contact angle of  $124^\circ$  compared to  $65^\circ$  the EB-Cu/GDL sample of the GDL is significantly more hydrophobic than the corresponding MS/GDL sample. For comparison, the contact angle of the fibrous backing side of the GDL is also  $124^\circ$  (Fig. B.3). The ECSA of Cu coated GDLs was measured by electrochemical double layer (DL) capacitance measurements in an Ar saturated 1 M  $\text{HClO}_4$  electrolyte (Fig. B.4 and Fig. B.5). CVs of 400 nm EB Cu-GDLs are shown in Fig. B.4a. The corresponding current density vs. scan rate plots (Fig. B.4b) show the expected linear behavior for pure capacitive DL charging. The roughness factor vs. thickness plot (Fig. 3.2f), obtained by using the measured area specific capacitance of a Cu foil of  $25 \mu\text{F}/\text{cm}^2$  as a reference (Fig. B.4c), reveals that the ECSA increases approximately linear between 100 and 400 nm EB Cu coating thickness with a maximum roughness factor of  $\sim 32$ , but decreases again for thicker Cu films indicating that for the thickest coatings some of the porosity becomes inaccessible. Similar trends with on average slightly higher roughness factors for nominally identical thicknesses have been observed for the MS-Cu coated GDLs (Fig. 3.2f and Fig. B.5).

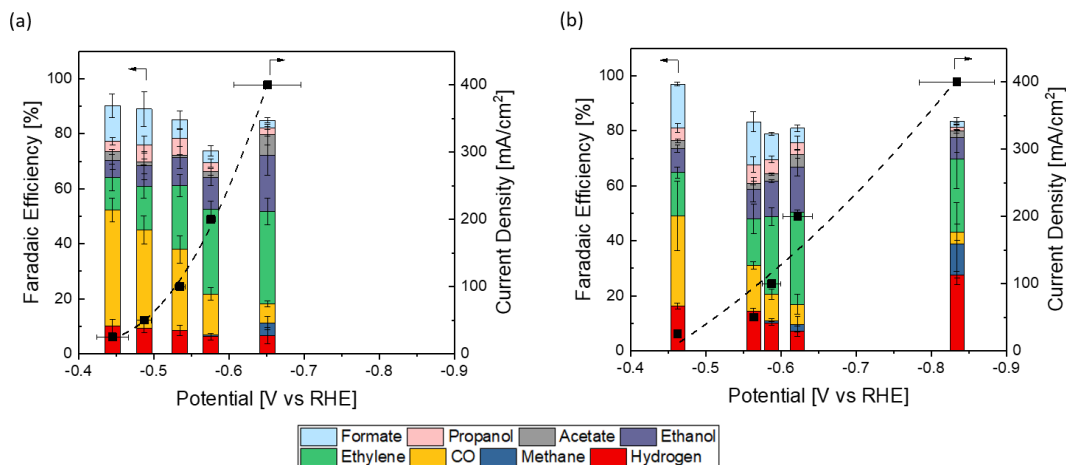


Figure 3.3: Faradaic efficiencies and current densities vs. potential for eCO<sub>2</sub>RR with 400 nm (a) EB-Cu and (b) MS-Cu catalysts. These tests were conducted in a three-compartment flow cell, with 15 sccm CO<sub>2</sub> and 1 M KOH electrolyte at room temperature.

To explore if and how the different Cu catalyst surface morphology, Cu/MPC interface structure, and wetting behavior affects the eCO<sub>2</sub>RR performance, nominally 400 nm thick EB and MS Cu catalysts films were tested using a three-compartment microfluidic flow cell for CO<sub>2</sub> electrolysis. Both samples show the product spectrum expected for eCO<sub>2</sub>RR over polycrystalline copper.<sup>9,11,29</sup> The Faradaic efficiencies (FEs) for ethylene, ethanol, and acetate go up with increasing potential/current density while that of CO decreases. However, there are distinct differences in the performance in terms of selectivity, current density, and stability: Compared to the MS Cu sample, the 400 nm EB Cu sample 1) reaches higher current densities at lower overpotentials (400 mA/cm<sup>2</sup> @ -0.65V vs. RHE for EB-Cu compared to 300 mA/cm<sup>2</sup> @ -0.72V vs. RHE for MS-Cu), and 2) better suppresses the competing hydrogen evolution reaction (HER), especially for high current densities; for the highest current density of 400 mA/cm<sup>2</sup>, H<sub>2</sub> FE for MS-Cu (28%) is 4 times higher than for EB-Cu (7%). For 400 nm

EB-Cu,  $C_{2+}$  FE reaches 70% at the highest current density of  $400 \text{ mA/cm}^2$ . As the total current density increases to  $400 \text{ mA/cm}^2$  for the MS-Cu sample, the voltage becomes unstable (Fig. 3.3) and the cathode suffers from flooding issues despite setting the  $\text{CO}_2$  backpressure to 15 psi as an attempt to stabilize the gas/liquid interface. We attribute these differences to the more hydrophilic character of MS-Cu coatings as revealed by the contact angle measurements (Fig 3.2d,e). In the microfluidic electrolyzer setup used for these experiments (Fig. B.1) the catalyst layer is in direct contact with a thin layer of liquid electrolyte, and the hydrophobicity of the GDL is thus crucial to prevent flooding which blocks the  $\text{CO}_2$  supply at the Cu catalyst.<sup>11</sup> The rougher surface nanoscale morphology and the thicker Cu/MPC interface of the MS-Cu coating seem to lower the GDL hydrophobicity resulting in more liquid penetrating the catalyst layer thus shifting the selectivity towards HER.

The effect of thickness of the EB-Cu catalysts coating on current density and  $\text{eCO}_2\text{RR}$  performance is summarized in Fig 3.4. Because the results discussed above revealed that the EB-Cu coatings outperform MS-Cu coatings in terms of selectivity, current density, and stability, we focused on EB-Cu coatings. The corresponding plots of Faradaic efficiencies and current densities vs. potential are shown in Figure B.6. In general, the  $\text{eCO}_2\text{RR}$  performance of the EB-Cu catalyst improves with increasing the catalyst loading. The overpotential required for any given current density decreases as the EB coating thickness increases, with the best performance observed for 400 nm thick EB Cu coatings that required the lowest overpotential ( $-0.65\text{V}$  vs RHE) for reaching a current density of  $400 \text{ mA/cm}^2$  (Fig. 3.4a). For thicker Cu catalysts coatings (800 nm) the overpotential increases again. Normalizing the  $\text{eCO}_2\text{RR}$  current density by the ECSA measured for the different coating thicknesses (Fig. 3.2f) reveals

that, regardless of the Cu loading, the coating thickness has little effect on the intrinsic activity of Cu, especially at the lower potentials (Fig. 3.4b). It also indicates that the entire ECSA contributes to eCO<sub>2</sub>RR. A closer look at the area normalized current density reveals that the higher current density data of the thinner 100/200 nm thick Cu coatings start to deviate from the linear behavior indicating the onset of mass transport limitations.

The coating thickness also affects the selectivity towards HER and CO<sub>2</sub>RR (Fig. 3.4c,d): For high current densities, the increase in HER can be suppressed by using thicker EB-Cu coatings (increasing the catalyst surface area) (Fig. 3.4c). For example, increasing the EB-Cu coating thickness from 100 (200) nm to 400 nm reduces H<sub>2</sub> FE by about a factor of 6 (5) times, from 37.7% at 300 mA/cm<sup>2</sup> for 100 nm Cu and 28.8% at 400 mA/cm<sup>2</sup> for 200 nm Cu to 6.7% at 400 mA/cm<sup>2</sup> for the 400 nm EB-Cu coating. The suppression of HER with increasing Cu coating thickness is accompanied by an increase in eCO<sub>2</sub>RR FE, from 23.2% (42.5%) at 300 (400) mA/cm<sup>2</sup> for 100 (200) nm EB-Cu to 72% at 400 mA/cm<sup>2</sup> for 400 nm EB-Cu (Fig. 3.4c). The suppression in HER with increasing roughness factor has also been observed for electrochemical CO reduction although at 100 times lower current densities.<sup>30</sup> The increase in eCO<sub>2</sub>RR selectivity with increasing Cu catalyst loading can be attributed to the higher Cu catalytic surface area available for eCO<sub>2</sub>RR (Fig. 3.2f and Fig. B.3). Consequently, the smaller Cu catalytic surface area of 800 nm EB-Cu coatings compared to 400 nm EB-Cu coatings (Fig. 3.2f and Fig. B.4) explains the increase observed for both the required overpotential (Fig. 3.4a) and H<sub>2</sub> FE (Fig. 3.4c). The reduced ECSA for the 800 nm sample is also evident in the SEM images (Fig.

B.2), in which the 800 nm sample shows more aggregation and less porosity than the 400 nm sample.

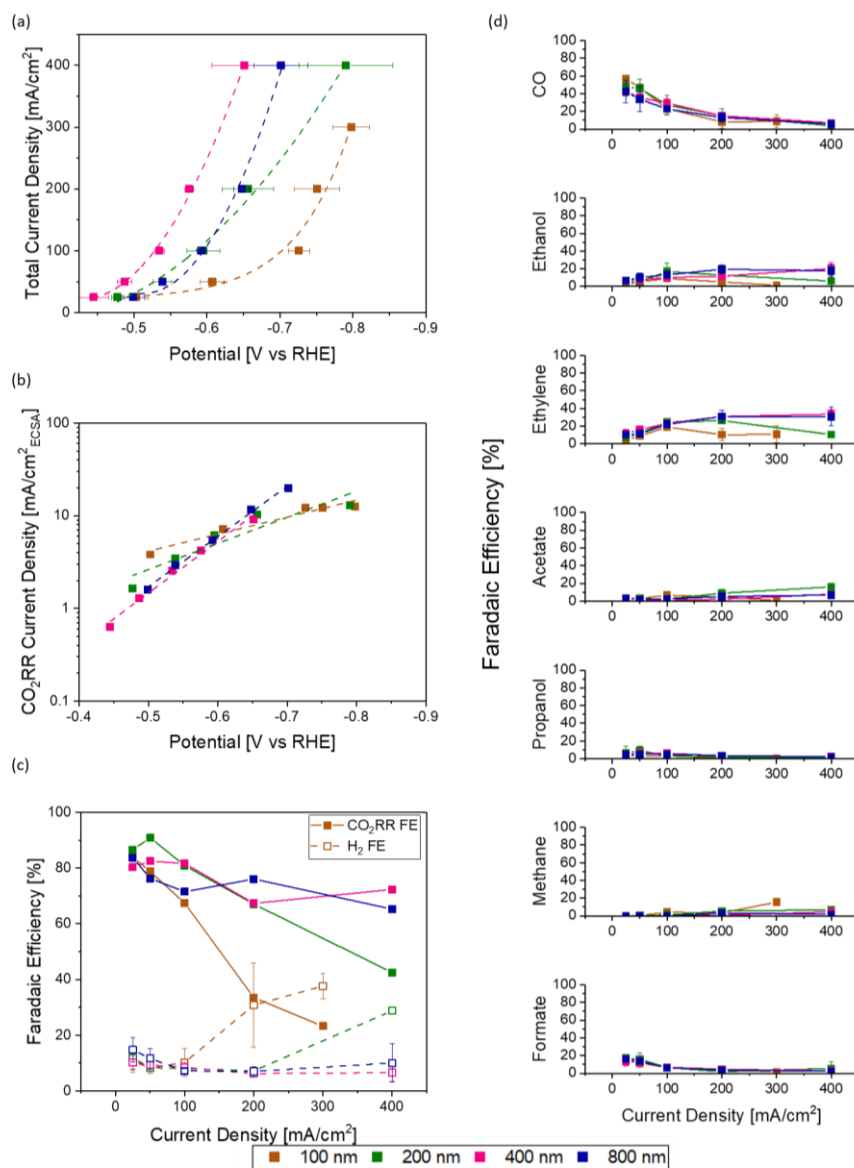


Figure 3.4: Comparison of the CO<sub>2</sub>RR performance of EB-Cu samples of different thicknesses (100, 200, 400, and 800 nm) measured in a 3-compartment electrochemical flow cell (Fig. B.1), with 15 sccm CO<sub>2</sub> and 1 M KOH electrolyte. (a) Total current densities vs. potential for all the thicknesses; (b) ECSA-normalized eCO<sub>2</sub>RR current densities for each catalyst; (c) H<sub>2</sub> and CO<sub>2</sub>RR Faradaic efficiencies for all the different thicknesses at different current densities; and (d) FE of eCO<sub>2</sub>RR products (CO, methane, formate, ethylene, ethanol, acetate, propanol) vs. current density.

The eCO<sub>2</sub>RR product distributions at different current densities for all the Cu catalysts are shown in Fig. 3.4d. CO and formate FEs decrease with increasing current density while the C<sub>2</sub> FEs (i.e., ethylene, ethanol and acetate FEs) increase with increasing current density, but only for the thicker Cu coatings (400 and 800 nm). The methane FE shows a maximum (15% @ 300 mA/cm<sup>2</sup>) for the highest current density – lowest coating thickness combination. The propanol FE is always low and shows no obvious dependence on current density or coating thickness. In summary, the most important effect of film thickness is that the selectivity for C<sub>2</sub> products at the highest current densities increases with increasing Cu loading. The effect of surface area / roughness factor on selectivity has recently also been reported for electrochemical CO reduction where the selectivity towards oxygenates increased with increasing roughness factor, although measured at much lower current densities (< 1 mA/cm<sup>2</sup>).<sup>30</sup>

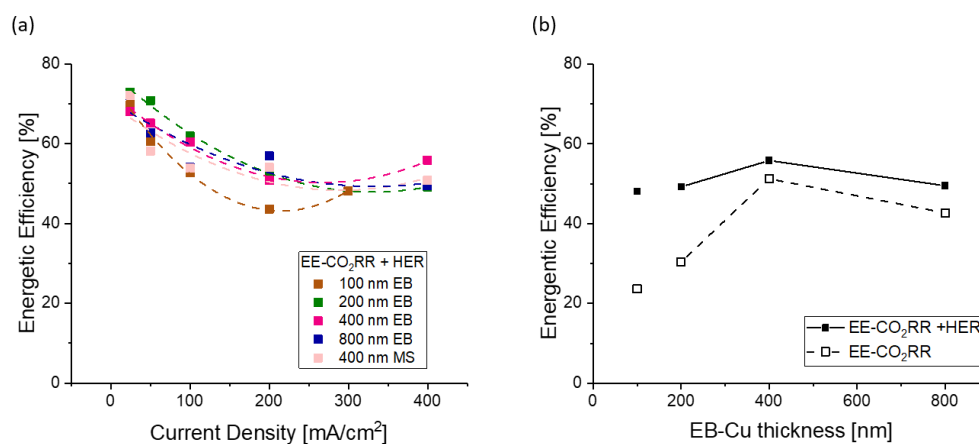


Figure 3.5: (a) Energy efficiency (CO<sub>2</sub>RR + HER) vs. current density for 100-800 nm EB Cu and 400 nm MS Cu catalyst coatings, and (b) energy efficiency vs. film thickness at the highest current density measured (300 mA/cm<sup>2</sup> for 100 nm EB-Cu, 400 mA/cm<sup>2</sup> for all other thicknesses). All tests were performed in the three-compartment flow cell (Fig. B.1) using 15 sccm CO<sub>2</sub> and 1 M KOH electrolyte.

An energy efficiency analysis confirms that the 400 nm EB-Cu catalyst coating provides the best combination of overpotential, eCO<sub>2</sub>RR FE, and current density, with a total (eCO<sub>2</sub>RR and HER combined) energy efficiency of 56.5% at 400 mA/cm<sup>2</sup> (Fig. 3.5). The energy efficiency was calculated using Faradaic efficiencies for each detected product including hydrogen (Fig. 3.4) using the following formula:

$$\varepsilon_{energetic} = \sum_k \frac{\varepsilon_{Faradaic,k} E_k^{\circ}}{E_{applied}}$$

Where  $\varepsilon_{Faradaic,k}$  is the Faradaic efficiency for product  $k$ , and  $E_k^{\circ}$  are the thermoneutral theoretical potentials for these products<sup>31</sup> shown in the table B.3. For all catalyst coating thicknesses, the total energy efficiency decreases with increasing current density, from ~70% for 25 mA/cm<sup>2</sup> to ~50% for 400 mA/cm<sup>2</sup> (Fig. 3.5a). For the highest current density (400 mA/cm<sup>2</sup>), the total (CO<sub>2</sub>RR + HER) FE (56.5%) and especially the CO<sub>2</sub>RR FE (51%) peak at 400 nm EB Cu (Fig. 3.5b). Note, that the maximum current density for the 100 nm EB Cu coating reached only 300 mA/cm<sup>2</sup>.

Extended eCO<sub>2</sub>RR tests with a 400 nm EB-Cu catalysts coating showed a stable performance (Fig. 3.6). This test ran for almost 6 hours, before H<sub>2</sub> FE started to increase. The potential gradually increased by ~15% over time where the increase slightly accelerated at the onset of the increase of H<sub>2</sub> FE after 4 hours. Post-reaction characterization through XPS and SEM imaging (Fig. B.7) revealed that the catalyst morphology and composition did not change during the test suggesting that the catalyst is not responsible for the degrading performance after 5 hours. XPS (Fig. B.7a) further showed that preexisting Cu<sup>+2</sup> oxides have been reduced during the eCO<sub>2</sub>RR. During the testing, water droplets and salt buildup were observed on the back of the GDL (Fig. B.7b) suggesting that catholyte has permeated through the GDL (despite controlling the gas-liquid interface through a back pressure controller set at a

constant 14.75 psi) resulting in partial blockage of the GDL for gas delivery. For long-term stability testing, it will thus be necessary to not only optimize the catalyst integration but also the GDL catalyst support to withstand flooding and prevent salt buildup during prolonged operations.

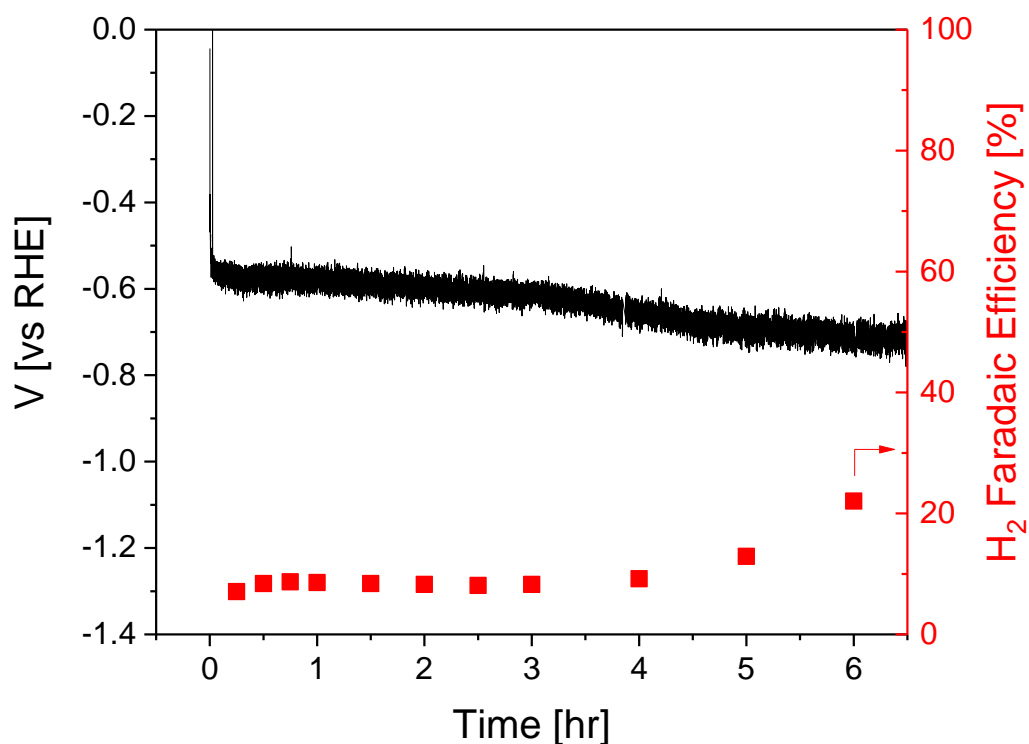


Figure 3.6: Electrode potential vs. RHE and FE(HER) during a long-term stability test of 400 nm EB-Cu in the microfluidic electrochemical flow cell at a constant current density of 100 mA/cm<sup>2</sup> with 15 sccm CO<sub>2</sub> and 1 M KOH electrolyte.

### 3.4 Conclusion

The effect of catalyst deposition methods and loading on eCO<sub>2</sub>RR performance was assessed in a microfluidic gas diffusion electrolyzer. EB-Cu catalysts showed generally better performance than the corresponding MS-Cu catalysts coatings which is attributed to the more hydrophobic character of EB Cu GDLs. RBS and TEM analysis revealed that more MS Cu is deposited within the MPC layer of the GDL, and that the MS Cu coatings are rougher than the corresponding EB Cu coatings, both rendering MS Cu catalyst coatings less hydrophobic and more prone to flooding. The thicknesses of the EB Cu samples also strongly affects device performance: Low Cu loadings (100 and 200 nm EB-Cu) result in higher overpotentials as well as lower FE for eCO<sub>2</sub>RR and C<sub>2</sub>H<sub>4</sub>. The weaker performance of lower Cu catalyst loadings is attributed to lower surface area available on these coatings. Increasing the Cu loading too much also reduced the eCO<sub>2</sub>RR performance as seen with the 800 nm EB-Cu, resulted in aggregation of the catalyst resulting in lower porosity and less catalytic surface area, which also led to worse performance. For the optimal thickness of 400 nm, EB Cu reached a combined eCO<sub>2</sub>RR and HER energetic efficiency of 56.5% at 400 mA/cm<sup>2</sup>. In summary, our works demonstrates that, despite little attention in the field, integration of eCO<sub>2</sub>RR catalysts is of equal importance to compositional tuning, and that the catalyst integrations need to be optimized for the specific electrolyzer environment. With other words, caution must be exercised when comparing the performance of different eCO<sub>2</sub>RR catalysts if the integration for these catalysts has not been optimized for a particular electrolyzer environment. The MS/EB PVD catalyst deposition techniques used in this work are particularly well suited to optimize both integration and composition of eCO<sub>2</sub>RR catalysts for large, industrially relevant electrolyzer electrodes as they allow the deposition of very homogeneous coatings

with very uniform catalyst loading while at the same time enabling morphological and compositional tuning including non-thermal equilibrium alloy compositions that otherwise are difficult to integrate.

### **3.5 Acknowledgements**

I would like to thank Dr. Juergen Biener and Dr. Zhen Qi for their help in this collaboration, synthesizing the materials, characterization (SEM, TEM, RBS, and contact angle measurements), and writing the manuscript. I would also like to thank Byunghee “Brian” Ko for his help in pre-reaction and post-reaction XPS characterization, and Haeun Shin for pre-reaction and post-reaction SEM characterization. Finally, I would like to thank Lawrence Livermore National Laboratory/Department of Energy for the funding of this work.

## REFERENCES

1. De Luna, P. et al. What would it take for renewably powered electrosynthesis to displace petrochemical processes? *Science* **364**, 350-+ (2019).
2. Bushuyev, O. S. et al. What Should We Make with CO<sub>2</sub> and How Can We Make It? *Joule* **2**, 825-832 (2018).
3. Haegel, N. M. et al. Terawatt-scale photovoltaics: Transform global energy. *Science* **364**, 836-+ (2019).
4. Jhong, H. R., Ma, S. C. & Kenis, P. J. A. Electrochemical conversion of CO<sub>2</sub> to useful chemicals: current status, remaining challenges, and future opportunities. *Current Opinion in Chemical Engineering* **2**, 191-199 (2013).
5. Dinh, C. T. et al. CO<sub>2</sub> electroreduction to ethylene via hydroxide-mediated copper catalysis at an abrupt interface. *Science* **360**, 783-787 (2018).
6. Hori, Y., Wakebe, H., Tsukamoto, T. & Koga, O. Electrocatalytic Process of CO Selectivity in Electrochemical Reduction of CO Selectivity in Electrochemical Reduction of CO<sub>2</sub> at Metal-Electrodes in Aqueous-Media. *Electrochimica Acta* **39**, 1833-1839 (1994).
7. Kortlever, R., Shen, J., Schouten, K. J. P., Calle-Vallejo, F. & Koper, M. T. M. Catalysts and Reaction Pathways for the Electrochemical Reduction of Carbon Dioxide. *Journal of Physical Chemistry Letters* **6**, 4073-4082 (2015).
8. Lu, Q., Rosen, J. & Jiao, F. Nanostructured Metallic Electrocatalysts for Carbon Dioxide Reduction. *Chemcatchem* **7**, 38-47 (2015).
9. Nitopi, S. et al. Progress and Perspectives of Electrochemical CO<sub>2</sub> Reduction on Copper in Aqueous Electrolyte. *Chemical Reviews* **119**, 7610-7672 (2019).
10. Fan, L. et al. Strategies in catalysts and electrolyzer design for electrochemical CO<sub>2</sub> reduction toward C<sub>2</sub>+ products. *Science Advances* **6** (2020).

11. Lv, J. J. et al. A Highly Porous Copper Electrocatalyst for Carbon Dioxide Reduction. *Advanced Materials* **30** (2018).
12. Weekes, D. M., Salvatore, D. A., Reyes, A., Huang, A. X. & Berlinguette, C. P. Electrolytic CO<sub>2</sub> Reduction in a Flow Cell. *Accounts of Chemical Research* **51**, 910-918 (2018).
13. Whipple, D. T., Finke, E. C. & Kenis, P. J. A. Microfluidic Reactor for the Electrochemical Reduction of Carbon Dioxide: The Effect of pH. *Electrochemical and Solid State Letters* **13**, D109-D111 (2010).
14. Burdyny, T. & Smith, W. A. CO<sub>2</sub> reduction on gas-diffusion electrodes and why catalytic performance must be assessed at commercially-relevant conditions. *Energy & Environmental Science* **12**, 1442-1453 (2019).
15. Weng, L.-C., Bell, A. T. & Weber, A. Z. Towards membrane-electrode assembly systems for CO<sub>2</sub> reduction: a modeling study. *Energy & Environmental Science* **12**, 1950-1968 (2019).
16. Hahn, C. et al. Engineering Cu surfaces for the electrocatalytic conversion of CO<sub>2</sub>: Controlling selectivity toward oxygenates and hydrocarbons. *Proceedings of the National Academy of Sciences of the United States of America* **114**, 5918-5923 (2017).
17. Kuhl, K. P., Cave, E. R., Abram, D. N. & Jaramillo, T. F. New insights into the electrochemical reduction of carbon dioxide on metallic copper surfaces. *Energy & Environmental Science* **5**, 7050-7059 (2012).
18. Ma, S. et al. Electroreduction of Carbon Dioxide to Hydrocarbons Using Bimetallic Cu-Pd Catalysts with Different Mixing Patterns. *Journal of the American Chemical Society* **139**, 47-50 (2017).
19. Reske, R., Mistry, H., Behafarid, F., Roldan Cuenya, B. & Strasser, P. Particle Size Effects in the Catalytic Electroreduction of CO<sub>2</sub> on Cu Nanoparticles. *Journal of the American Chemical Society* **136**, 6978-6986 (2014).
20. Hori, Y., Takahashi, I., Koga, O. & Hoshi, N. Electrochemical reduction of carbon dioxide at various series of copper single crystal electrodes. *Journal of Molecular Catalysis a-Chemical* **199**, 39-47 (2003).
21. Jiang, K. et al. Metal ion cycling of Cu foil for selective C-C coupling in electrochemical CO<sub>2</sub> reduction. *Nature Catalysis* **1**, 111-119 (2018).

22. Li, C. W. & Kanan, M. W. CO<sub>2</sub> Reduction at Low Overpotential on Cu Electrodes Resulting from the Reduction of Thick Cu<sub>2</sub>O Films. *Journal of the American Chemical Society* **134**, 7231-7234 (2012).
23. Loiudice, A. et al. Tailoring Copper Nanocrystals towards C-2 Products in Electrochemical CO<sub>2</sub> Reduction. *Angewandte Chemie-International Edition* **55**, 5789-5792 (2016).
24. Jhong, H. R., Brushett, F. R. & Kenis, P. J. A. The Effects of Catalyst Layer Deposition Methodology on Electrode Performance. *Advanced Energy Materials* **3**, 589-599 (2013).
25. Taylor, A. D., Kim, E. Y., Humes, V. P., Kizuka, J. & Thompson, L. T. Inkjet printing of carbon supported platinum 3-D catalyst layers for use in fuel cells. *Journal of Power Sources* **171**, 101-106 (2007).
26. Wang, Z. Q. & Nagao, Y. Effects of Nafion impregnation using inkjet printing for membrane electrode assemblies in polymer electrolyte membrane fuel cells. *Electrochimica Acta* **129**, 343-347 (2014).
27. Wang, Y. & Nastasi, M. Handbook of Modern Ion Beam Materials Analysis. (2010).
28. Doolittle, L. R. Algorithms for the rapid simulation of rutherford backscattering spectra. *Nuclear Instruments & Methods in Physics Research Section B-Beam Interactions with Materials and Atoms* **9**, 344-351 (1985).
29. Tang, W. et al. The importance of surface morphology in controlling the selectivity of polycrystalline copper for CO<sub>2</sub> electroreduction. *Physical Chemistry Chemical Physics* **14**, 76-81 (2012).
30. Wang, L. et al. Electrochemically converting carbon monoxide to liquid fuels by directing selectivity with electrode surface area. *Nature Catalysis* **2**, 702-708 (2019).
31. Martín, A. J., Larrazábal, G. O. & Pérez-Ramírez, J. Towards sustainable fuels and chemicals through the electrochemical reduction of CO<sub>2</sub>: lessons from water electrolysis. *Green Chemistry* **17**, 5114-5130 (2015).

## Chapter 4

### CONCLUSIONS AND RECOMMENDATIONS

#### 4.1 Conclusion

In this thesis, I have discussed different studies for flow cell CO<sub>2</sub> electrolyzers. First, I investigate the single-pass conversion for a CO<sub>2</sub> flow cell electrolyzer, a figure-of-merit that is not usually discussed for CO<sub>2</sub> electrolysis studies. Systematic studies with a MEA-type flow cell electrolyzer for the conversion of CO<sub>2</sub> to CO were conducted, and it was observed that the highest single-pass conversion to CO could only reach up to 50% due to the formation of carbonates during the electrolysis process, regardless of gas inlet flow rate or temperature. In addition, the single-pass conversion was found to affect the gas outlet stream composition of the electrolyzer. This study has shown that although a majority of the CO<sub>2</sub> (up to 95%) is consumed during the electrolysis process, only about 50% of the CO<sub>2</sub> is being utilized for conversion to CO.

Next, I talk about the work done with the three-compartment, microfluidic flow cell electrolyzer, specifically the electrodes used for such a system. Copper electrodes with different fabrication methods, E-beam deposition and magnetron sputtering deposition, were tested for CO<sub>2</sub> electrolysis. It was found that E-beam deposited copper had a better performance, as the deposition method did not affect the PTFE layer. In addition, an optimal thickness for fabrication was shown to be at 400 nm, as both thinner and thicker films had less catalytic surface area. This study

showed that not only is catalyst development in CO<sub>2</sub> electrolysis important, but also how the gas diffusion electrode is fabricated.

While these studies have brought more insight into the development for CO<sub>2</sub> electrolyzers, they also show that clearly more work needs to be done for further improvement. The following recommendations should be considered going forward.

## **4.2 Recommendations**

### **4.2.1 Carbonate Formation/CO<sub>2</sub> Crossover**

As discussed previously, the single-pass conversion of CO<sub>2</sub> to CO is limited to only about 50% because of the hydroxide consuming the fed CO<sub>2</sub>. These carbonates would then travel across the membrane, over to the anode, to be reconverted back to CO<sub>2</sub> due to the shift in equilibrium in the electrolyte. Preventing the formation of carbonate would be necessary to improve the overall CO<sub>2</sub> utilization, but it is also not a trivial challenge<sup>1</sup>.

One possible solution to consider is utilizing a bicarbonate buffer along with a cation exchange membrane catholyte to prevent the bicarbonate crossover to the anode. This has been demonstrated as one of the most effective cell configurations for eCO<sub>2</sub>R<sup>2</sup>. Luc et al had demonstrated that the use of this bicarbonate buffer had resulted in improved CO<sub>2</sub> conversion, up to 86%<sup>3</sup>. However, this would also come at the expense of the Faradaic efficiency, as to operate at high conversions, a lower CO<sub>2</sub> flow rate is desirable. This lower CO<sub>2</sub> flow rate could result in a higher possibility of flooding with the buffer layer in direct contact with the catalyst, and thus a higher H<sub>2</sub> F.E. In addition, it was observed that the stability of the system using a cation exchange membrane resulted in lower stability due to the cation transfer across the

membrane being replaced by the cations from the electrolyte, as opposed to the much more mobile  $\text{H}^+$  ions. One possible solution to improve that stability is to start with the membrane ion exchange with the cations in the electrolyte, as opposed to activation through acid. However, because of the poorer mobility of cations in comparison to hydrogen ions<sup>4</sup>, this will result in increased voltage necessary to obtain higher current densities.

Another suggestion would be to utilize a bipolar membrane to prevent the  $\text{CO}_2$  from crossing over. With a bipolar membrane configuration, water is dissociated into  $\text{H}^+$  and  $\text{OH}^-$ , which travel to the cathode and the anode, respectively. The hydrogen ions formed could protonate the formed carbonate and bicarbonate ions back into  $\text{CO}_2$ . However, it must be noted that to prevent the selectivity from shifting to  $\text{H}_2$ , a buffer layer must also be used<sup>5</sup>. Even without this buffer layer, another drawback with using a bipolar membrane layer is the higher overpotential needed for operation<sup>6</sup>.

In addition, bipolar membrane configurations have been used for directly converting bicarbonate and carbonate to other  $\text{CO}_2$  products<sup>7,8</sup>. This could especially be advantageous if the  $\text{CO}_2$  is captured using alkaline solutions, as a direct conversion would avoid the extra step of regeneration and reduce the energy input necessary. The selectivity towards  $\text{CO}_2$  reduction is still low for these direct conversion systems, as the hydrogen ions formed from water dissociation from the membrane will lead to a selectivity shifting towards  $\text{H}_2$ . However, it was shown that tuning the electrode structure could also help with shifting the selectivity towards  $\text{eCO}_2\text{R}$  products<sup>9</sup>.

To prevent salt buildup and thus avoiding possible issues regarding the electrolyzer stability, alkaline electrolytes should be avoided as much as possible, even if an alkaline environment would result in a better performance for  $\text{CO}_2$  electrolysis.

As seen in Figure B.7b, when the cations of the electrolyte interact with the formed carbonate anions, salt can form either in the gas channels and/or the backing of the gas diffusion layer<sup>10,11</sup>, resulting in blocked gas delivery and thus poor stability.

Minimizing cation concentration in the electrolyte would be ideal, but completely removing the cations would result in needing to use DI water instead of an electrolyte. While this has been demonstrated with one electrolyzer for the production of formate by using a solid polymer electrolyte made of a porous styrene-divinylbenzene copolymer with sulfonic acid functional groups for H<sup>+</sup> conductivity and quaternary amino functional groups<sup>12</sup>, very few electrolyzers have been able to operate using DI water, as the overall conductivity would also degrade over time.

#### **4.2.2 Membranes and Ionomers**

One way to lower the overall ohmic resistance of the electrolyzer is to design better membranes for better ionic conductivity. Voltage is the main parameter that will influence the operating costs of eCO<sub>2</sub>R<sup>13</sup>, so it is crucial to lower the potential needed to overcome the ohmic resistances. For anion exchange membranes, in fuel cell studies involving anion exchange membranes, carbon dioxide is purged out of the reactant stream to prevent the reaction with hydroxide to form carbonate ions, which has a much lower mobility traveling in aqueous solutions and thus results in much lower conductivity<sup>14</sup>. However, since the formation of carbonate ions is currently an inevitable problem for CO<sub>2</sub> electrolysis, anion exchange membranes should be designed to be extremely conductive to carbonate ions. Currently, one of the few reported anion exchange membranes used for CO<sub>2</sub> electrolysis includes Sustainion, which is a polystyrene-based membrane with imidazolium functional groups and has high carbonate ion conductivity, able to maintain 200 mA/cm<sup>2</sup> at 3 V for 1000 hours<sup>15</sup>.

Improved conductivity for carbonate ions must be investigated to reach higher current densities at lower voltages. In addition, another zero-gap flow cell electrolyzer used an anion exchange membrane called the PiperION membrane, which is comprised of piperidinium cations<sup>16,17</sup>. Using this membrane had also shown high conductivity for carbonate ions, reaching a current density of 1 A/cm<sup>2</sup> at similar voltages<sup>16</sup>.

In addition to designing the membrane, designing and optimizing the ionomer for eCO<sub>2</sub>R should also be investigated. In many eCO<sub>2</sub>R studies, Nafion has been used as the binder. However, as demonstrated by Kutz et al, the ionomer could affect the performance<sup>15</sup>. Too little ionomer resulting in poor ionic conductivity, while too much ionomer results in higher catalyst coverage and thus higher resistance. While designing the membrane,

For the MEA-type configuration, the water uptake of membranes is also something to consider as a strategy to mitigate severe flooding for eCO<sub>2</sub>R. For instance, Berlinguette et al had looked into different types of membranes based on water uptake and thickness for MEA electrolyzers, observing that the best performance came from their thinnest (about 20  $\mu$ m) low water uptake membranes<sup>18</sup>. They explain that based on their transport model, the thickness affects the water flux most drastically, as it can influence the amount of water back-diffusion away from the cathode. This suggests that more studies should investigate membranes as another water management strategy.

#### **4.2.3 CO<sub>2</sub> Gas Delivery**

Water management remains a crucial issue regardless of eCO<sub>2</sub>R in either the MEA-type configuration and the microfluidic flow cell. Control of the gas-liquid interface is necessary, as the accumulation of water over time will affect the

selectivity, shifting towards forming hydrogen instead of carbon products, and thus also affect the stability of the electrolysis process.

One aspect to investigate should be the tuning of properties of GDLs for CO<sub>2</sub> electrolyzers specifically. The GDL should be tuned to allow for efficient gas reactant delivery, maintain low electrical resistance, and prevent flooding. Some have looked into constructing GDLs for these different types of CO<sub>2</sub> electrolyzers. For instance, for the microfluidic electrochemical flow cell, Kenis et al had looked into tuning the PTFE content in the microporous layer and varying the thickness of the carbon fiber substrate, trying to find an optimum amount that will provide the hydrophobicity while still maintaining a low resistance<sup>19</sup>. In addition, Sargent et al had designed an electrode in which the catalyst is deposited onto a PTFE membrane, which allows for hydrophobicity to prevent flooding and maintain stability<sup>20</sup>. However, for a scaled-up CO<sub>2</sub> electrolyzer, a scaled-up electrode fabricated this way would result in large resistances that would increase the overpotential drastically. GDLs were also investigated in an MEA-electrolyzer set-up in conjunction with different types of membranes, with the best performance using a GDL with 29% PTFE along with a thin membrane with low water uptake<sup>18</sup>. When testing catalysts in the flow cell electrolyzers, GDLs optimized for electrolyzers, whether for the three-compartment flow cell or for the MEA-type flow cell, should be used.

Another aspect to examine includes the way in which the CO<sub>2</sub> gas is delivered. As CO<sub>2</sub> electrolyzers scale up, maintaining an even distribution of the gas reactant will become more crucial. From Chapter 2, for a 25 cm<sup>2</sup> electrode, we observe that the performance becomes limited by the flooding from the decrease in the gas partial pressure as it travels along the serpentine flow field, resulting in unreacted CO<sub>2</sub> in the

effluent stream. Designing flow fields for electrolyzer systems will be important for flow cells to ensure that the gas is evenly distributed throughout the electrode. One transport mechanism that could be utilized for flow field design, often discussed in the flow fields for fuel cells, is under-rib convection, in which the difference in pressure between the ribs would result in a convective flow<sup>21,22</sup>. For the design of flow fields, similar to what has been done with fuel cell study, using computational fluid dynamics (CFD) software<sup>23</sup>, in conjunction to experimental methods to track the water distribution such as neutron scattering<sup>24,25</sup>, would be useful for a better understanding in how effective and well-distributed the gas reactant is delivered.

Overall, all of these recommendations are all interconnected, and combining these strategies could help to improve the overall efficiency of CO<sub>2</sub> electrolyzers.

## REFERENCES

1. Rabinowitz, J. A. & Kanan, M. W. The future of low-temperature carbon dioxide electrolysis depends on solving one basic problem. *Nature Communications* vol. 11 1–3 (2020).
2. Delacourt, C., Ridgway, P. L., Kerr, J. B. & Newman, J. Design of an electrochemical cell making syngas ( $\text{CO} + \text{H}_2$ ) from  $\text{CO}_2$  and  $\text{H}_2\text{O}$  reduction at room temperature. *J. Electrochem. Soc.* **155**, 42–49 (2008).
3. Luc, W., Jouny, M., Rosen, J. & Jiao, F. Carbon dioxide splitting using an electro-thermochemical hybrid looping strategy. *Energy Environ. Sci.* **11**, 2928–2934 (2018).
4. Varcoe, J. R. *et al.* Anion-exchange membranes in electrochemical energy systems. *Energy Environ. Sci.* **7**, 3135–3191 (2014).
5. Salvatore, D. A. *et al.* Electrolysis of Gaseous  $\text{CO}_2$  to CO in a Flow Cell with a Bipolar Membrane. *ACS Energy Lett.* **3**, 149–154 (2018).
6. Salvatore, D. & Berlinguette, C. P. Voltage Matters When Reducing  $\text{CO}_2$  in an Electrochemical Flow Cell. *ACS Energy Lett.* **5**, 215–220 (2020).
7. Li, T. *et al.* Electrolytic Conversion of Bicarbonate into CO in a Flow Cell. *Joule* **3**, 1487–1497 (2019).
8. Li, Y. C. *et al.*  $\text{CO}_2$  Electroreduction from Carbonate Electrolyte. *ACS Energy Lett.* **4**, 1427–1431 (2019).
9. Lees, E. W. *et al.* Electrodes Designed for Converting Bicarbonate into CO. *ACS Energy Lett.* (2020).
10. Tewari, A., Sambhy, V., Urquidi MacDonald, M. & Sen, A. Quantification of carbon dioxide poisoning in air breathing alkaline fuel cells. *J. Power Sources* **153**, 1–10 (2006).
11. Adams, L. A., Poynton, S. D., Tamain, C., Slade, R. C. T. & Varcoe, J. R. A carbon dioxide tolerant aqueous-electrolyte-free anion-exchange membrane alkaline fuel cell. *ChemSusChem* **1**, 79–81 (2008).

12. Xia, C. *et al.* Continuous production of pure liquid fuel solutions via electrocatalytic CO<sub>2</sub> reduction using solid-electrolyte devices. *Nat. Energy* **4**, 776–785 (2019).
13. Jouny, M., Luc, W. & Jiao, F. General Techno-Economic Analysis of CO<sub>2</sub> Electrolysis Systems. *Ind. Eng. Chem. Res.* **57**, 2165–2177 (2018).
14. Varcoe, J. R. *et al.* Anion-exchange membranes in electrochemical energy systems. *Energy Environ. Sci.* **7**, 3135–3191 (2014).
15. Kutz, R. B. *et al.* Sustainion Imidazolium-Functionalized Polymers for Carbon Dioxide Electrolysis. *Energy Technol.* **5**, 929–936 (2017).
16. Endrődi, B. *et al.* High carbonate ion conductance of a robust PiperION membrane allows industrial current density and conversion in a zero-gap carbon dioxide electrolyzer cell. *Energy Environ. Sci.* (2020).
17. Wang, J. *et al.* Poly(aryl piperidinium) membranes and ionomers for hydroxide exchange membrane fuel cells. *Nat. Energy* **4**, 392–398 (2019).
18. Reyes, A. *et al.* Managing Hydration at the Cathode Enables Efficient CO<sub>2</sub> Electrolysis at Commercially Relevant Current Densities. *ACS Energy Lett.* **5**, 1612–1618 (2020).
19. Kim, B., Hillman, F., Ariyoshi, M., Fujikawa, S. & Kenis, P. J. A. Effects of composition of the micro porous layer and the substrate on performance in the electrochemical reduction of CO<sub>2</sub> to CO. *J. Power Sources* **312**, 192–198 (2016).
20. Dinh, C. T. *et al.* CO<sub>2</sub> electroreduction to ethylene via hydroxide-mediated copper catalysis at an abrupt interface. *Science (80-. ).* **360**, 783–787 (2018).
21. Nam, J. H., Lee, K. J., Sohn, S. & Kim, C. J. Multi-pass serpentine flow-fields to enhance under-rib convection in polymer electrolyte membrane fuel cells: Design and geometrical characterization. *J. Power Sources* **188**, 14–23 (2009).
22. Wang, C. *et al.* The respective effect of under-rib convection and pressure drop of flow fields on the performance of PEM fuel cells. *Sci. Rep.* **7**, 1–9 (2017).
23. Le, A. D. & Zhou, B. A general model of proton exchange membrane fuel cell. *J. Power Sources* **182**, 197–222 (2008).

24. Ueda, S., Koizumi, S. & Tsutsumi, Y. Flooding and performance of polymer electrolyte fuel cell, investigated by small-angle neutron scattering, neutron radiography and segmented electrode. *Results Phys.* **12**, 504–511 (2019).
25. Holderer, O. *et al.* Fuel cell electrode characterization using neutron scattering. *Materials (Basel)*. **13**, 1–9 (2020).

## Appendix A

### SUPPLEMENTARY INFORMATION FOR CHAPTER 2- INVESTIGATIONS OF CO<sub>2</sub> SINGLE-PASS CONVERSION IN A FLOW ELECTROLYZER

Table A.1: Literature comparison of CO<sub>2</sub> single-pass conversion in CO<sub>2</sub> flow electrolyzers.

Ref.	Flow cell configuration	Catalyst	CO <sub>2</sub> feeding rate [mL/min]	Electrode size [cm <sup>2</sup> ]	CO Faradaic Efficiency [%]	Reported Current Density [mA/cm <sup>2</sup> ]	Conversion to CO [%]
1	microfluidic flow cell	commercial silver nanoparticles (100 nm)	17	6.25	90%	440	19.7
2	pressurized electrolytic cell	Porous Ag sheet	50	6.25	80-90%	191.25	8.1
3	microfluidic flow cell	Ag/MWCNT on GDL (mixed 1:1)	7	1	90%	350	38.0
4	microfluidic flow cell	MWNT/PyPBI/Au	17	8.4	63.60%	200	44.7
5	microfluidic flow cell	Ag nanoparticles and 40% Ag/TiO <sub>2</sub>	7	1	90%	100	10.9
6	microfluidic flow cell	Ni-N-C	50	5	85%	200	9.1
7	bipolar membrane	Ag nanopowder	100	1	50%	200	9.5
8	liquid flow cell	Ag nanopowder	50	0.1	37%	100	6.1

9	Three-compartment flow cell	Ag nanoparticles	50	3	80%	300	4.6
10	Three-compartment flow cell	Ag/PTFE	50	6.25	90%	150	2.3

Table A.2: Constants for the calculations of CO<sub>2</sub> consumption due to carbonate formations.

Constant	Equation/Value	Units	Reference
H <sub>CO<sub>2</sub></sub>	$34 \times 10^{-6} \exp\left[\left(\frac{1}{T} - \frac{1}{273.15}\right)\right]$	mol cm <sup>-3</sup> atm <sup>-1</sup>	11
K1	$10^{[-126.3408 + \frac{6320.813}{T} + 19.568224 \ln(T)]}$	mol cm <sup>-3</sup> atm <sup>-1</sup>	12
K2	$10^{[-90.18333 + \frac{5143.692}{T} + 14.613358 \ln(T)]}$	mol cm <sup>-3</sup> atm <sup>-1</sup>	12
k <sub>1f</sub>	$2.0 \times 10^{18} \exp\left[-\frac{7698}{T}\right]$	cm <sup>3</sup> mol <sup>-1</sup> s <sup>-1</sup>	13
kw	$1.0 \times 10^{-6}$	mol cm <sup>-3</sup> s <sup>-1</sup>	11
D <sub>OH<sup>-</sup></sub>	$2.89 \times 10^{-5} \exp\left[-1750\left(\frac{1}{T} - \frac{1}{273.15}\right)\right]$	cm <sup>2</sup> s <sup>-1</sup>	13
D <sub>HCO<sub>3</sub><sup>-</sup></sub>	$7.016 \times 10^{-5} \left(\frac{T}{204.0282} - 1\right)^{2.3942}$	cm <sup>2</sup> s <sup>-1</sup>	13
D <sub>CO<sub>3</sub><sup>2-</sup></sub>	$5.447 \times 10^{-5} \left(\frac{T}{210.2646} - 1\right)^{2.1929}$	cm <sup>2</sup> s <sup>-1</sup>	13
IEC	$1.1 \times 10^{-3}$	mol g <sup>-1</sup>	14
ρ <sub>mem</sub>	1.23	g cm <sup>-3</sup>	15

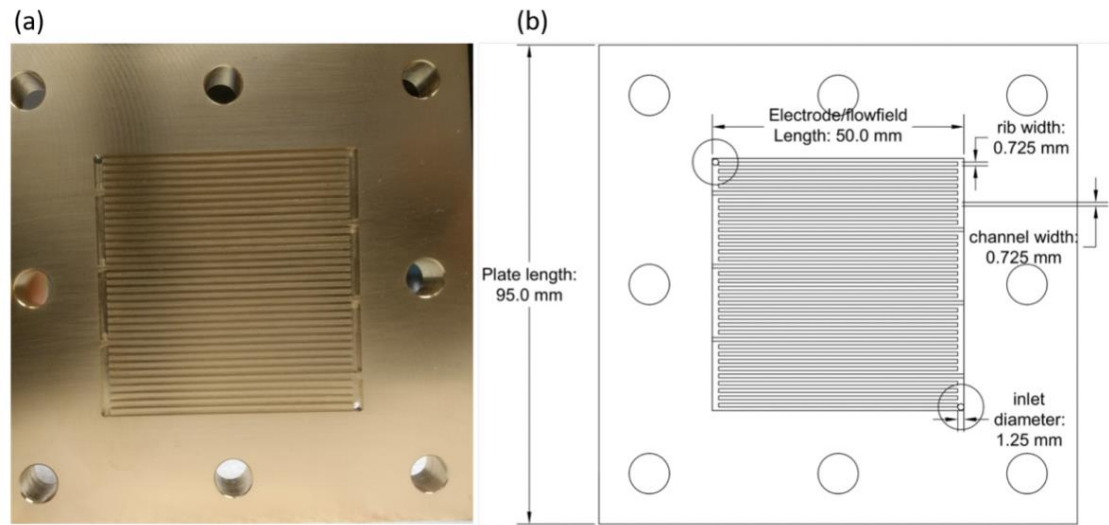


Figure A.1- Serpentine flow field used for the cathode during testing: (a) picture and (b) drawing with dimensions.

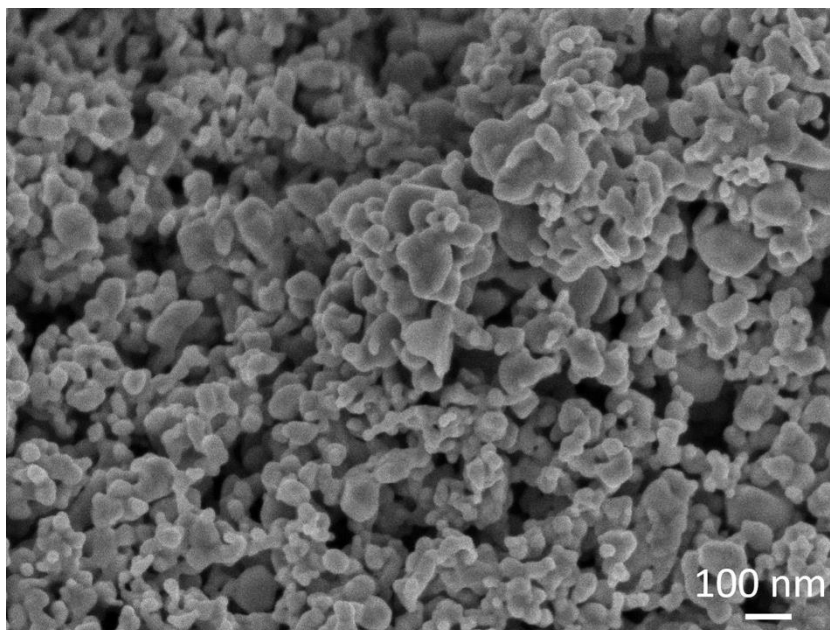


Figure A.2-SEM image of 100-nm silver nanoparticles deposited on the gas diffusion layer.

### Calculation of theoretical rate of CO<sub>2</sub> conversion to carbonates

Only CO<sub>2</sub> dissolved in an aqueous environment would undergo the reaction with hydroxides, so the concentration of CO<sub>2</sub> dissolved in water at the electrode surface was calculated based on Henry's Law, as shown in the following equation:

$$[\text{CO}_2]_{\text{aq}} = H_{\text{CO}_2} P_{\text{CO}_2}$$

Since the concentration of CO<sub>2</sub> will continue to decrease as the gas travels along the serpentine channel, the log mean average CO<sub>2</sub> concentration was assumed for calculation as an approximate amount of how much CO<sub>2</sub> will be available for carbonate formation during the simultaneous electroreduction reaction, setting the initial pressure of CO<sub>2</sub> as 1 atm and the final partial pressure of CO<sub>2</sub> to reflect the lowest possible concentration of CO<sub>2</sub> in the outlet exiting the outlet. Although ideally we would want to have no CO<sub>2</sub> leftover in the effluent, we used a CO<sub>2</sub> partial pressure of 0.005 atm as the amount leftover after the entire reaction.

A modified Nernst-Planck equation relating ion flux to the current was used:

$$J_i = \frac{z_i C_i D_i}{\sum_i^n z_i C_i D_i} \left( -\frac{I}{F} \right)$$

Where  $J_i$  represents the flux of species  $i$  across the membrane,  $D_i$  represents the diffusion coefficient of species  $i$  in an aqueous medium,  $F$  represents Faraday's constant,  $R$  represents the gas constant,  $T$  represents temperature, and  $z_i$  represents the valence of the ion.

At steady state, the reaction rate of carbonate formation is set equal to the total carbonate flux, represented by the Nernst-Planck equation. To determine the actual concentration of hydroxide at the electrode surface formed during the reaction, equilibrium constants,  $K_1$  and  $K_2$ , and the water dissociation constant,  $K_w$ , as shown

below, were used to convert the concentration of bicarbonate and carbonate as expressions relating with the concentration of hydroxide.

$$K1 = \frac{[H^+][HCO_3^-]}{[CO_2]_{aq}} = \frac{kw[HCO_3^-]}{[OH^-][CO_2]_{aq}}$$

$$K2 = \frac{[H^+][CO_3^{2-}]}{[HCO_3^-]} = \frac{kw[CO_3^{2-}]}{[OH^-][HCO_3^-]}$$

In addition, we assumed charge conservation by setting the total anion concentration equal to that of the membrane, which represents the cation concentration. The cation concentration,  $C^+$ , is given by taking the product of the specified ion exchange capacity of the membrane and the density of the membrane ( $\rho_{mem}$ ). This charge conservation equation was also used to rearrange the bicarbonate concentration as an expression related to hydroxide.

$$C^+ = IEC \cdot \rho_{mem} = 2[CO_3^{2-}] + [HCO_3^-] + [OH^-]$$

With all these assumptions and substitutions of equations, we can calculate the steady state concentration of hydroxide, and as a result, we can calculate the concentrations of bicarbonate and carbonate. This will give us the total flux of carbonates and bicarbonates, which would give us the total amount of  $CO_2$  that will react with hydroxides at the given current, using the constants listed in Table A.2.

## REFERENCES

1. Verma, S., Lu, X., Ma, S., Masel, R. I. & Kenis, P. J. A. The effect of electrolyte composition on the electroreduction of CO<sub>2</sub> to CO on Ag based gas diffusion electrodes. *Phys. Chem. Chem. Phys.* **18**, 7075–7084 (2016).
2. Dufek, E. J., Lister, T. E., Stone, S. G. & McIlwain, M. E. Operation of a Pressurized System for Continuous Reduction of CO<sub>2</sub>. *J. Electrochem. Soc.* **159**, F514–F517 (2012).
3. Ma, S. *et al.* Carbon nanotube containing Ag catalyst layers for efficient and selective reduction of carbon dioxide. *J. Mater. Chem. A* **4**, 8573–8578 (2016).
4. Verma, S. Hamasaki, Y., Kim, C., Huang, W., Lu, S., Jhong, H. R. M., Gewirth, A. A., Fujigaya, T., Nakashima, N., Kenis, P. J. A. Insights into the Low Overpotential Electroreduction of CO<sub>2</sub> to CO on a Supported Gold Catalyst in an Alkaline Flow Electrolyzer. *ACS Energy Lett.* **3**, 193–198 (2018).
5. Ma, S., Lan, Y., Perez, G. M. J., Moniri, S. & Kenis, P. J. A. Silver supported on titania as an active catalyst for electrochemical carbon dioxide reduction. *ChemSusChem* **7**, 866–874 (2014).
6. Möller, T., Ju, W., Bagger, A., Wang, X., Luo, F., Ngo Thanh, T., Varela, A. S., Rossmeisl, J., Strasser, P. Efficient CO<sub>2</sub> to CO electrolysis on solid Ni-N-C catalysts at industrial current densities. *Energy Environ. Sci.* **12**, 640–647 (2019).
7. Salvatore, D. A., Weekes, D. M., He, J., Dettelbach, K. E., Li, Y. C., Mallouk, T. E., Berlinguette, C. P. Electrolysis of Gaseous CO<sub>2</sub> to CO in a Flow Cell with a Bipolar Membrane. *ACS Energy Lett.* **3**, 149–154 (2018).
8. Li, T., Lees, E. W., Goldman, M., Salvatore, D. A., Weekes, D. M., Berlinguette, C. P. Electrolytic Conversion of Bicarbonate into CO in a Flow Cell. *Joule* **3**, 1487–1497 (2019).

9. Gabardo, C. M., Seifitokaldani, A., Edwards, J. P., Dinh, C. T., Burdyny, T., Kibria, M. G., O'Brien, C. P., Sargent, E. H., Sinton, D. Combined high alkalinity and pressurization enable efficient CO<sub>2</sub> electroreduction to CO. *Energy Environ. Sci.* **11**, 2531–2539 (2018).
10. Dinh, C. T., García De Arquer, F. P., Sinton, D. & Sargent, E. H. High rate, Selective, and Stable Electroreduction of CO<sub>2</sub> to CO in Basic and Neutral Media. *ACS Energy Lett.* **3**, 2835–2840 (2018).
11. Weng, L.-C., Bell, A. T. & Weber, A. Z. Towards membrane-electrode assembly systems for CO<sub>2</sub> reduction: a modeling study. *Energy Environ. Sci.* **12**, 1950–1968 (2019).
12. Millero, F. J., Graham, T. B., Huang, F., Bustos-Serrano, H. & Pierrot, D. Dissociation constants of carbonic acid in seawater as a function of salinity and temperature. *Mar. Chem.* **100**, 80–94 (2006).
13. Myles, T. D., Grew, K. N., Peracchio, A. A. & Chiu, W. K. S. Transient ion exchange of anion exchange membranes exposed to carbon dioxide. *J. Power Sources* **296**, 225–236 (2015).
14. Kaczur, J. J., Yang, H., Liu, Z., Sajjad, S. D. & Masel, R. I. Carbon Dioxide and Water Electrolysis Using New Alkaline Stable Anion Membranes. *Front. Chem.* **6**, 263 (2018).
15. Dighe, A. S. Imidazole. *Pharmaceutical Organic Chemistry* (2020).

## Appendix B

### SUPPLEMENTARY INFORMATION FOR CHAPTER 3- SCALABLE GAS DIFFUSION ELECTRODE FABRICATION FOR ELECTROCHEMICAL CO<sub>2</sub> REDUCTION USING PHYSICAL VAPOR DEPOSITION METHODS

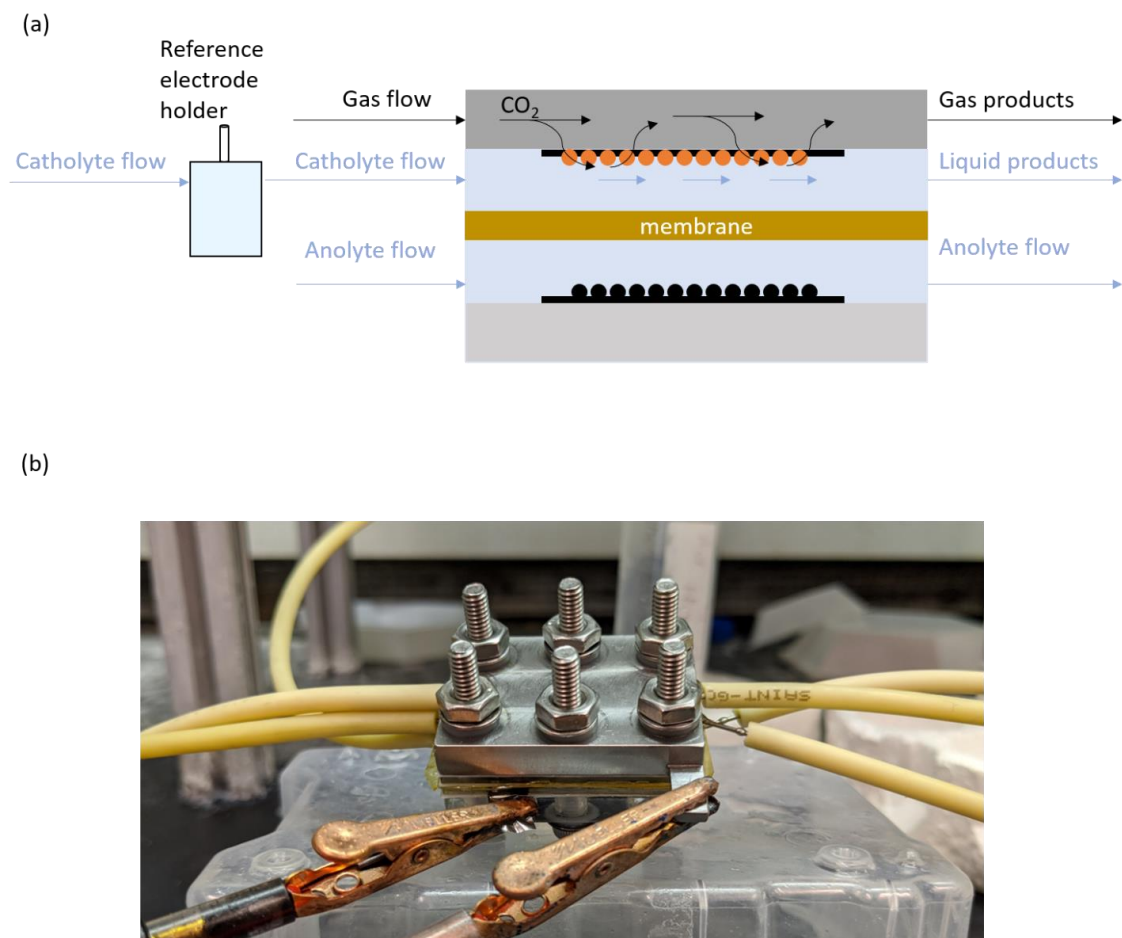


Figure B.1: Electrochemical Testing with the Three-Compartment Flow Cell Set-up, with (a) the schematic and (b) the picture during testing

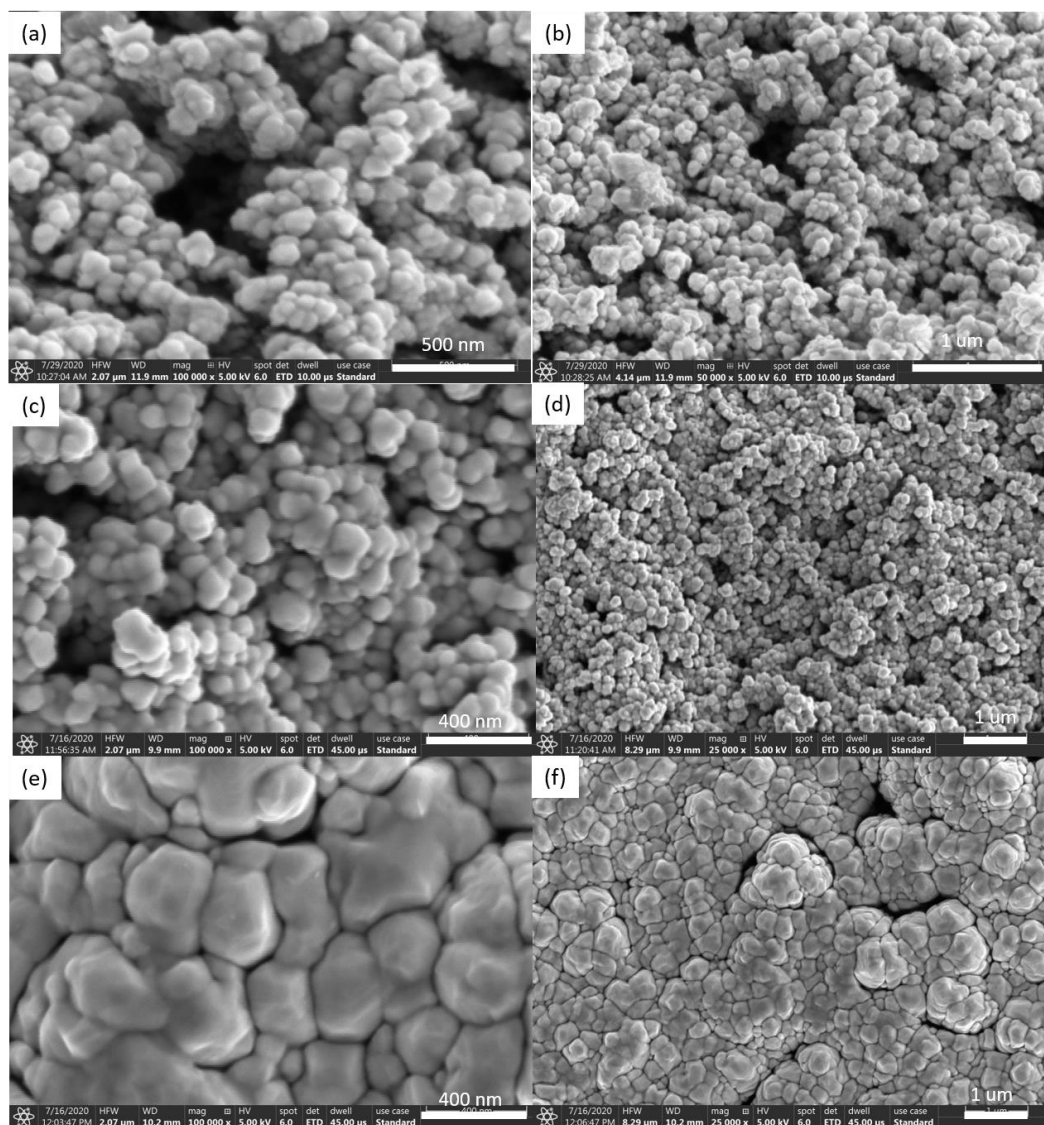


Figure B.2: SEM images of (a, b) 100 nm, (c, d) 200 nm, and (e, f) 800 nm thickness EB-Cu samples

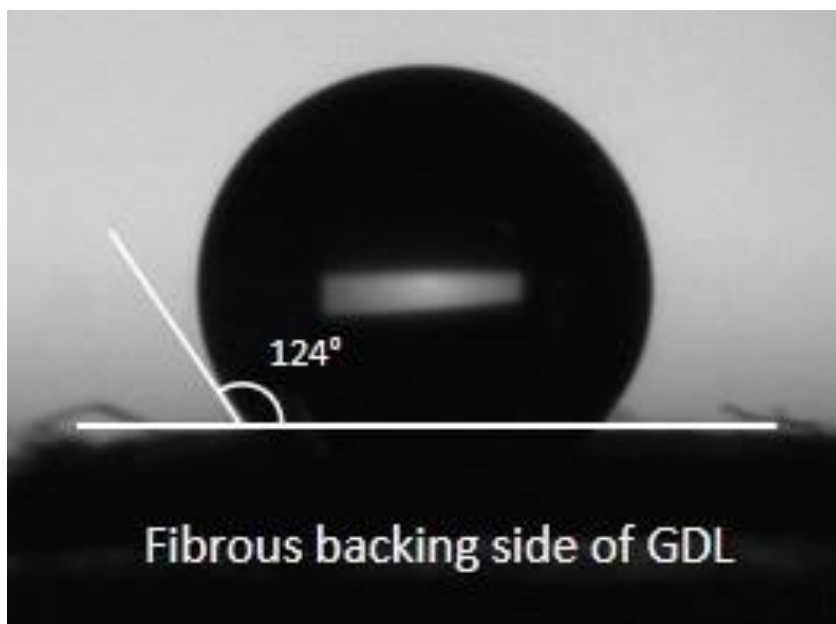


Figure B.3: Contact angle measurement on fibrous backing side of the GDL

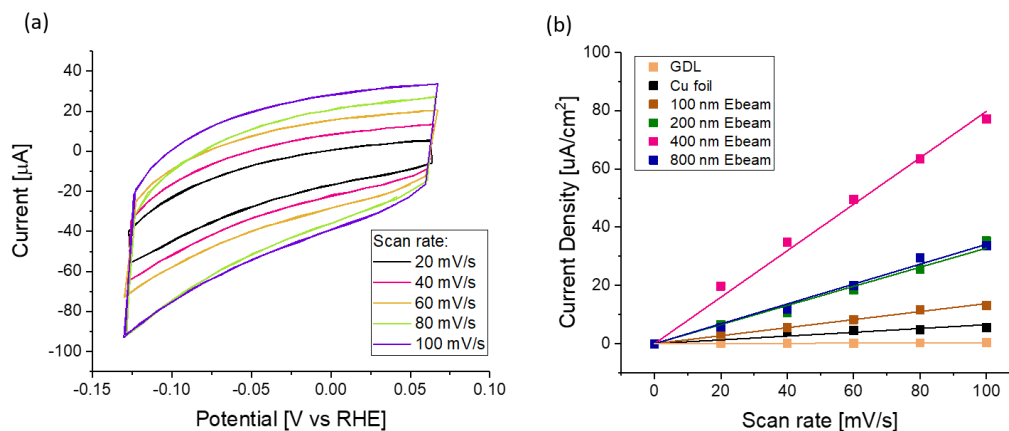


Figure B.4: EB-Cu GDL electrochemical surface area (ECSA) measurements: (a) sample CV scans at different scan rates in 0.1 M HClO<sub>4</sub> for the 400 nm EB Cu, (b) plot of current density vs scan rate for capacitance measurements

Sample	Capacitance [ $\mu\text{F}/\text{cm}^2$ ]	Roughness factor
GDL	3.4	—
Cu foil	25.0	1
100 nm Ebeam	137.8	5.51
200 nm Ebeam	343.5	13.74
400 nm Ebeam	798.1	31.92
800 nm Ebeam	343.3	13.65

Table B.1: Measured capacitance values and corresponding roughness factor of each sample obtained by normalization to Cu foil

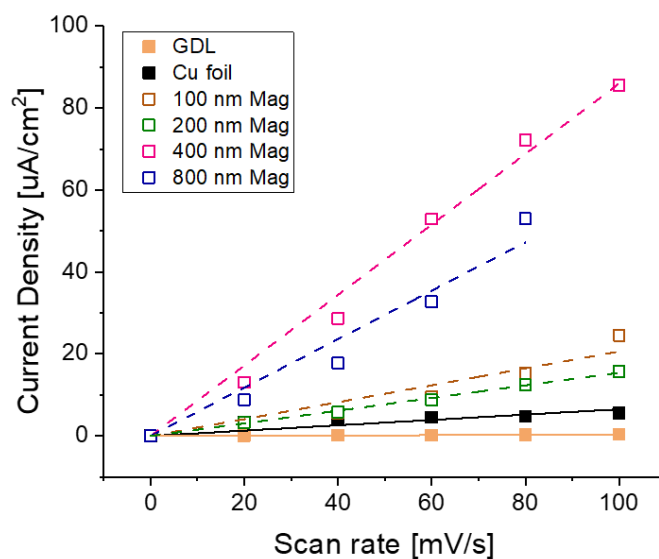


Figure B.5: MS-Cu GDL electrochemical surface area (ECSA) measurements: Plot of current density vs scan rate for capacitance measurements 0.1 M HClO<sub>4</sub>

Sample	Capacitance [ $\mu\text{F}/\text{cm}^2$ ]	Roughness factor
GDL	3.4	—
Cu foil	25.0	1
100 nm Mag	206.3	8.25
200 nm Mag	154.5	6.18
400 nm Mag	860.1	34.4
800 nm Mag	591.0	23.64

Table B.2: Measured capacitance values and corresponding roughness factor of each sample obtained by normalization to Cu foil

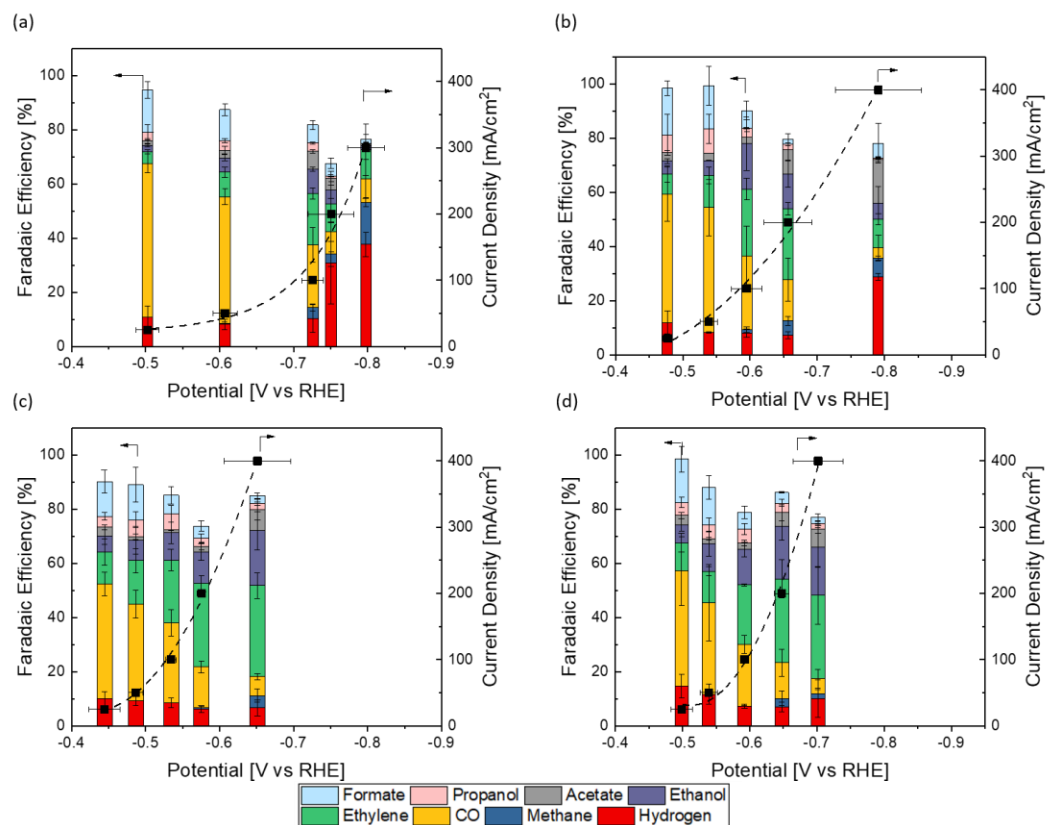


Figure B.6: Faradaic efficiencies and current densities vs. potential for EB-Cu at (a) 100 nm (b) 200 nm (c) 400 nm and (d) 800 nm thickness. These tests were conducted in the 3-compartment flow cell (Fig. B.1), with 15 sccm CO<sub>2</sub> and 1 M KOH electrolyte.

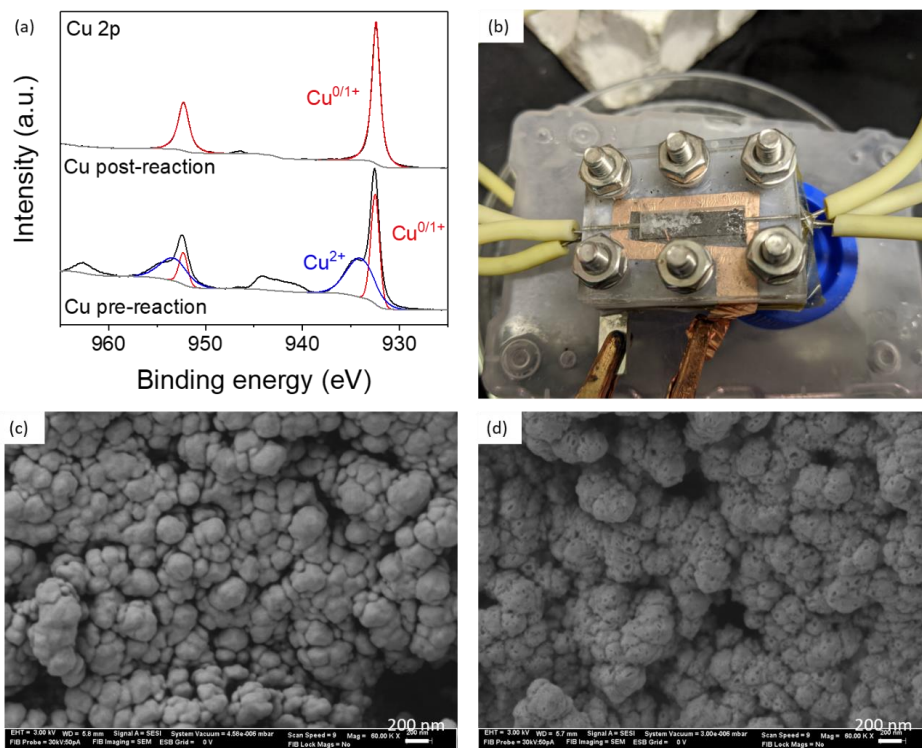


Figure B.7: Long-term stability test of 400 nm EB-Cu: (a) XPS Characterization of the EB-Cu sample before and after 6 hours at a constant current of  $100 \text{ mA/cm}^2$  reaction; (b) Picture showing the formation of salt on the backside of the GDL during the stability testing; (c) Pre-reaction and (d) post-reaction SEM images of the EB-Cu catalyst coating show no change in morphology due to  $\text{CO}_2\text{R}$

Product	Thermoneutral [V]
CO	1.47
HCOO <sup>-</sup>	1.34
CH <sub>4</sub>	1.15
C <sub>2</sub> H <sub>4</sub>	1.22
H <sub>2</sub>	1.48
C <sub>2</sub> H <sub>5</sub> OH	1.18
C <sub>3</sub> H <sub>7</sub> OH	0.97
AcO <sup>-</sup>	1.36


Table B.3: Thermoneutral theoretical potentials for products detected in Fig. 3.4

## Appendix C

### PERMISSION LETTERS

Figure C.1: Permission Letter for Chapter 2

2/3/2021 University of Delaware Mail - RE: Permission Request Form: Emily Jeng

 **G Suite** Emily Jeng <ecjeng@udel.edu>

---

**RE: Permission Request Form: Emily Jeng**  
1 message

---

**CONTRACTS-COPYRIGHT (shared)** <Contracts-Copyright@rsc.org> Thu, Sep 3, 2020 at 2:13 AM  
To: "ecjeng@udel.edu" <ecjeng@udel.edu>

Many thanks for sending the permissions request below. The Royal Society of Chemistry (RSC) hereby grants permission for the use of your paper(s) specified below in the printed and microfilm version of your thesis. You may also make available the PDF version of your paper(s) that the RSC sent to the corresponding author(s) of your paper(s) upon publication of the paper(s) in the following ways: in your thesis via any website that your university may have for the deposition of theses, via your university's Intranet or via your own personal website. We are however unable to grant you permission to include the PDF version of the paper(s) on its own in your institutional repository. The Royal Society of Chemistry is a signatory to the STM Guidelines on Permissions (available on request).

Please note that if the material specified below or any part of it appears with credit or acknowledgement to a third party then you must also secure permission from that third party before reproducing that material.

Please ensure that the thesis states the following:

Reproduced by permission of The Royal Society of Chemistry

and include a link to the paper on the Royal Society of Chemistry's website.

Please ensure that your co-authors are aware that you are including the paper in your thesis.

Best wishes,

**Chloe Szebrat**  
Contracts and Copyright Executive  
Royal Society of Chemistry  
Thomas Graham House  
Science Park, Milton Road  
Cambridge, CB4 0WF, UK  
[www.rsc.org](http://www.rsc.org)

**From:** [ecjeng@udel.edu](mailto:ecjeng@udel.edu) <[ecjeng@udel.edu](mailto:ecjeng@udel.edu)>  
**Sent:** 29 August 2020 01:33

<https://mail.google.com/mail/u/1/?ik=2a84ed2d68&view=pt&search=all&permthid=thread-f%3A1676792126734336910&simpl=msg-f%3A16767921267...> 1/2

2/3/2021

University of Delaware Mail - RE: Permission Request Form: Emily Jeng

**To:** CONTRACTS-COPYRIGHT (shared) <[Contracts-Copyright@rsc.org](mailto:Contracts-Copyright@rsc.org)>  
**Subject:** Permission Request Form: Emily Jeng

Name: Emily Jeng

Institution: University of Delaware

Email: [ecjeng@udel.edu](mailto:ecjeng@udel.edu)

Address:

[2 The Horseshoe](#)

Newark  
19711  
United States

**I am preparing the following work for publication:**

Article/chapter title: Investigation of CO<sub>2</sub> single-pass conversion in a flow electrolyzer  
Journal/book title: Reaction Chemistry & Engineering  
Editor/author(s): Emily Jeng and Feng Jiao  
Publisher: Royal Society of Chemistry  
Is this request for a thesis?: Yes

**I would very much appreciate your permission to use the following material:**

Journal/book title: Reaction Chemistry & Engineering  
Editor/author(s): Emily Jeng & Engineering  
ISBN/DOI: 10.1039/D0RE00261E  
Year of publication: 2020  
Page(s): 1768-1775  
Type of material: Full paper  
Figure/image number (if relevant):

**Any additional comments:**

**Agree to terms:** I agree

This communication is from The Royal Society of Chemistry, a company incorporated in England by Royal Charter (registered number RC000524) and a charity registered in England and Wales (charity number 207890). Registered office: Burlington House, Piccadilly, London W1J 0BA. Telephone: +44 (0) 20 7437 8656.

The content of this communication (including any attachments) is confidential, and may be privileged or contain copyright material. It may not be relied upon or disclosed to any person other than the intended recipient(s) without the consent of The Royal Society of Chemistry. If you are not the intended recipient(s), please (1) notify us immediately by replying to this email, (2) delete all copies from your system, and (3) note that disclosure, distribution, copying or use of this communication is strictly prohibited.

Any advice given by The Royal Society of Chemistry has been carefully formulated but is based on the information available to it. The Royal Society of Chemistry cannot be held responsible for accuracy or completeness of this communication or any attachment. Any views or opinions presented in this email are solely those of the author and do not represent those of The Royal Society of Chemistry. The views expressed in this communication are personal to the sender and unless specifically stated, this e-mail does not constitute any part of an offer or contract. The Royal Society of Chemistry shall not be liable for any resulting damage or loss as a result of the use of this email and/or attachments, or for the consequences of any actions taken on the basis of the information provided. The Royal Society of Chemistry does not warrant that its emails or attachments are Virus-free; The Royal Society of Chemistry has taken reasonable precautions to ensure that no viruses are contained in this email, but does not accept any responsibility once this email has been transmitted. Please rely on your own screening of electronic communication.

More information on The Royal Society of Chemistry can be found on our website: [www.rsc.org](http://www.rsc.org)

<https://mail.google.com/mail/u/1?ik=2a84ed2d68&view=pt&search=all&permthid=thread-f%3A1676792126734336910&simpl=msg-f%3A16767921267...> 2/2

Figure C.2: Permission Letter for Figure 1.3

2/3/2021

University of Delaware Mail - RE: Permission Request Form: Emily Jeng



Emily Jeng <ecjeng@udel.edu>

---

**RE: Permission Request Form: Emily Jeng**

1 message

---

**CONTRACTS-COPYRIGHT (shared)** <Contracts-Copyright@rsc.org>  
To: "ecjeng@udel.edu" <ecjeng@udel.edu>

Mon, Nov 2, 2020 at 9:24 AM

Many thanks for sending the permissions request below. The Royal Society of Chemistry hereby grants permission for the use of the material specified below in your thesis.

Please note that if the material specified below or any part of it appears with credit or acknowledgement to a third party then you must also secure permission from that third party before reproducing that material.

Please ensure that the published article carries a credit to The Royal Society of Chemistry in the following format:

[Original citation] – Reproduced by permission of The Royal Society of Chemistry

and that any electronic version of the work includes a hyperlink to the article on the Royal Society of Chemistry website.

Best wishes,

**Chloe Szebrat**  
Contracts and Copyright Executive  
Royal Society of Chemistry  
Thomas Graham House  
Science Park, Milton Road  
Cambridge, CB4 0WF, UK

[www.rsc.org](http://www.rsc.org)

**From:** [ecjeng@udel.edu](mailto:ecjeng@udel.edu) <[ecjeng@udel.edu](mailto:ecjeng@udel.edu)>

**Sent:** 01 November 2020 02:58

**To:** CONTRACTS-COPYRIGHT (shared) <[Contracts-Copyright@rsc.org](mailto:Contracts-Copyright@rsc.org)>

**Subject:** Permission Request Form: Emily Jeng

Name: Emily Jeng

Institution: University of Delaware

Email: [ecjeng@udel.edu](mailto:ecjeng@udel.edu)

<https://mail.google.com/mail/u/1?ik=2a84ed2d68&view=pt&search=all&permthid=thread-f%3A1682258856896054579&simpl=msg-f%3A16822588568...> 1/2

2/3/2021

University of Delaware Mail - RE: Permission Request Form: Emily Jeng

Address:

12 Main St, Apt 1

Enfield  
03748  
United States

**I am preparing the following work for publication:**

Article/chapter title: Investigations into Flow Cell Electrolyzers for CO<sub>2</sub> Reduction  
Journal/book title: Investigations into Flow Cell Electrolyzers for CO<sub>2</sub> Reduction  
Editor/author(s): Emily Jeng  
Publisher: University of Delaware  
Is this request for a thesis?: Yes

**I would very much appreciate your permission to use the following material:**

Journal/book title: Green Chemistry  
Editor/author(s): Antonio J. Martín, Gastón O. Larrazábal and Javier Pérez-Ramírez  
ISBN/DOI: 10.1039/C5GC01893E  
Year of publication: 2015  
Page(s): 5118  
Type of material: Image  
Figure/image number (if relevant): Figure 3

**Any additional comments:**

**Agree to terms:** I agree

This communication is from The Royal Society of Chemistry, a company incorporated in England by Royal Charter (registered number RC000524) and a charity registered in England and Wales (charity number 207890). Registered office: Burlington House, Piccadilly, London W1J 0BA. Telephone: +44 (0) 20 7437 8656.

The content of this communication (including any attachments) is confidential, and may be privileged or contain copyright material. It may not be relied upon or disclosed to any person other than the intended recipient(s) without the consent of The Royal Society of Chemistry. If you are not the intended recipient(s), please (1) notify us immediately by replying to this email, (2) delete all copies from your system, and (3) note that disclosure, distribution, copying or use of this communication is strictly prohibited.

Any advice given by The Royal Society of Chemistry has been carefully formulated but is based on the information available to it. The Royal Society of Chemistry cannot be held responsible for accuracy or completeness of this communication or any attachment. Any views or opinions presented in this email are solely those of the author and do not represent those of The Royal Society of Chemistry. The views expressed in this communication are personal to the sender and unless specifically stated, this e-mail does not constitute any part of an offer or contract. The Royal Society of Chemistry shall not be liable for any resulting damage or loss as a result of the use of this email and/or attachments, or for the consequences of any actions taken on the basis of the information provided. The Royal Society of Chemistry does not warrant that its emails or attachments are Virus-free; The Royal Society of Chemistry has taken reasonable precautions to ensure that no viruses are contained in this email, but does not accept any responsibility once this email has been transmitted. Please rely on your own screening of electronic communication.

More information on The Royal Society of Chemistry can be found on our website: [www.rsc.org](http://www.rsc.org)

<https://mail.google.com/mail/u/1?ik=2a84ed2d68&view=pt&search=all&permthid=thread-f%3A1682258856896054579&simpl=msg-f%3A16822588568...> 2/2